3-20-2017

Hall Effect Thruster Characterization through Potential, Magnetic, and Optical Measurements

Nicholas L. Hyatt

HALL EFFECT THRUSTER CHARACTERIZATION THROUGH POTENTIAL, MAGNETIC, AND OPTICAL MEASUREMENTS

THESIS

Nicholas L. Hyatt, Captain, USAF

AFIT-ENY-MS-17-M-267

DEPARTMENT OF THE AIR FORCE
AIR UNIVERSITY

AIR FORCE INSTITUTE OF TECHNOLOGY

Wright-Patterson Air Force Base, Ohio

AFIT-ENY-MS-17-M-267

Hall Effect Thruster Characterization Through Potential, Magnetic, and Optical Measurements

THESIS

Presented to the Faculty

Department of Aeronautics and Astronautics

Graduate School of Engineering and Management

Air Force Institute of Technology

Air University

Air Education and Training Command

In Partial Fulfillment of the Requirements for the

Degree of Master of Science in Astronautical Engineering

Nicholas L. Hyatt, BS

Captain, USAF

March 2017

AFIT-ENY-MS-17-M-267

Hall Effect Thruster Characterization Through Potential, Magnetic, and Optical Measurements

Nicholas L. Hyatt
Captain, USAF

Approved:

Carl Hartsfield, PhD (Chairman)	Date
Maj. David Liu, PhD (Member)	Date
William Hargus, PhD (Member)	Date

AFIT-ENY-MS-17-M-267

Abstract

Electric propulsion is a promising method for providing ΔV to spacecraft on orbit. In general, much higher I_{sp}s are obtained compared to their chemical counterparts. Hall thrusters are a subset of electric propulsion with moderately high specific impulse and thrust when compared to other forms of electric propulsion. Even though Hall thrusters have an extensive flight legacy around the world, there are still many unknowns associated with their operation. Experimental research was conducted in AFIT's Space Propulsion Application Simulation System (SPASS) laboratory, to measure Hall current, plasma potential and visible emission from the 600W Hall thruster in a time correlated system at data rates up to 1MHz. Unfortunately issues would plague the experiment and ultimately prevent any data collection on the thruster understudy. Instead data collected prior was further analyzed in attempt correlate behavior of plasma instabilities to determine causal relationships between plasma properties and anomalous diffusion modes. This was done by performing a frequency analysis where frequencies associated with breathing mode and spoke mode were identified.

For my wonderful wife and son. Thanks for your love and support!

Acknowledgments

I would like to express my sincere appreciation to Dr. Carl Hartsfield for his guidance and support throughout the course of this thesis effort. I would also like to thank Josh, Jamie, and Keith for their support with the labs and equipment.

I would also like to acknowledge Dr. Mitat Birkan of the Air Force Office of Scientific Research for providing funding and support for this research.

Nicholas L. Hyatt

Table of Contents

Page

List of Figures

Page

List of Tables

Page

List of Symbols

Symbol	Definition
$\vec{E}$	electric field, V/m
$\vec{B}$	magnetic field, G
g_0	acceleration due to Gravity, 9.81 $\frac{m}{s^2}$
I_{sp}	specific impulse, s
m	mass, kg
$\dot{m}$	mass flow rate, kg/s
N	Newton
sccm	Standard Cubic Centimeters per Minute
ΔV	change in velocity
v	voltage, V
R	resistance, Ohm
I	current, Amp
t	time, sec
T	thrust, N
η	efficiency
P	power, W
ω_c	cyclotron frequency Hz
q	charge, C
E	energy, J
c	speed of light, 2.99e8 $\frac{m}{s}$

λ	wave length, nm
$J(r')$	Current distribution
μ_0	permeability of free space
A	Green's Matrix
L	regularizing term

HALL EFFECT THRUSTER CHARACTERIZATION THROUGH POTENTIAL, MAGNETIC, AND OPTICAL MEASUREMENTS

I. Introduction

Background

Of the many different forms of propulsion that can be used in space, the two most popular are chemical and electrical. Chemical rockets get their energy from the reaction of an oxidizer and a fuel. This reaction will cause an increase in temperature in the chamber and expels the reactants through the converging/diverging nozzle, producing the desired thrust. On the other hand, electric propulsion in the form of Hall thrusters and ion engines use ionized gasses which are accelerated by an electrostatic field to provide thrust. Electric propulsion is an improved method for providing velocity to spacecraft because much higher specific impulses (I_{SP}) can be realized compared to their chemical counterparts. Hall thrusters are a subset of electric propulsion with moderately high I_{SP} and thrust. In general, I_{SP}s of Hall thrusters range from 1100 to 2000+ seconds, which is much higher than their chemical counterparts whose I_{SP}s range from 150-400 seconds [1]. The advantage of higher I_{SP} propulsion options is that less propellant is required on the satellite when compared to its chemical counterpart. An additional advantage to electric propulsion is the ability to restart thousands of times over the life of the satellite. This makes them ideal for orbital corrections and station keeping.

From their advent in the 1960s, Hall thrusters have been used for orbit station keeping, attitude control, and orbit transfer [1]. The first major use of Hall thrusters was by the Russians for station keeping on communication satellites in 1971 [1]. The United States of America did not use a Hall thruster on orbit until 1998 when it was part of the National

Reconnaissance Office's Space Technology Experiment (STEX) satellite. In 2010, a Hall thruster aboard the Air Force Advanced Extremely High Frequency (AEHF) satellite, made the news when it proved its usefulness by providing the ΔV for circularizing the geo transfer orbit to a geosynchronous orbit after the main propulsion unit failed due to a propellant blockage of the apogee kick motor [1] [2]. As the requirements for high I_{SP} with relatively high thrust density increase, Hall thrusters will become more prevalent, which will require better modeling capabilities for more efficient implementation.

This research will focus on Hall effect thrusters; thus, a basic understanding of how they work will be useful. The picture in figure 1 shows the general construction of a Hall thruster. The major components consist of a cylindrical channel surrounded by magnets on the inner and outer surfaces, an anode with gas feed at the back of the channel, and a cathode mounted on the outside of the channel. The cylindrical channel has an axial electric and radial magnetic field applied. This field traps electrons and causes them to drift in the $\vec{E}x\vec{B}$ direction. These drifting electrons ionize the propellant gas as it flows through the cylindrical channel. Once ionized, the electric field between the anode and cathode propels the positive ions out of the channel at speeds up to 10^2 km/s [1].

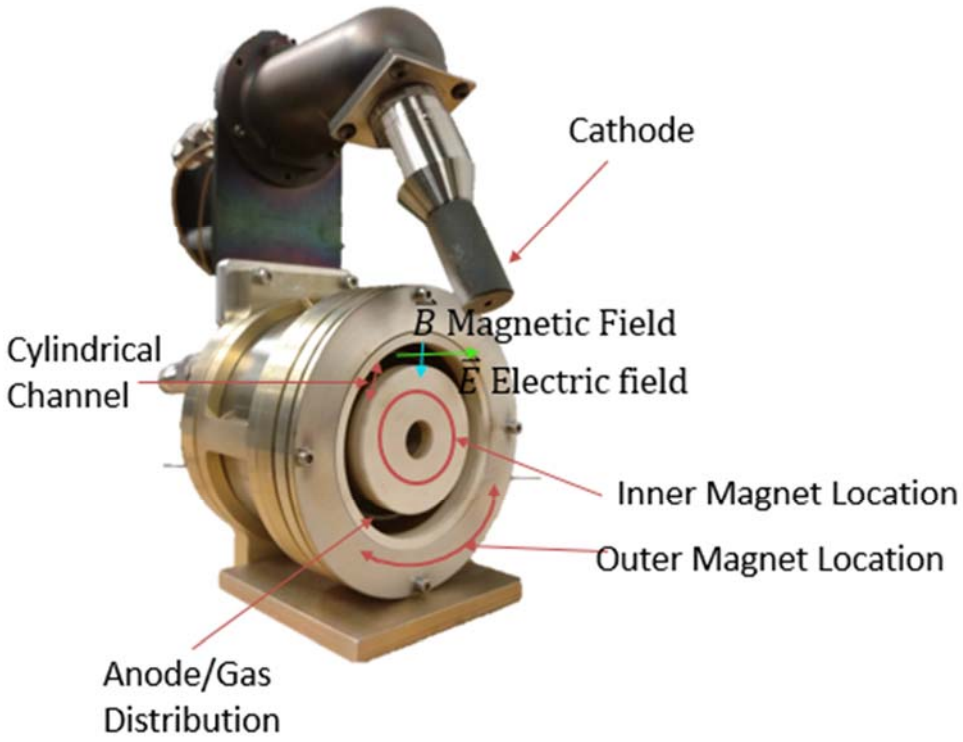

Figure 1: Hall Thruster

The efficiency, versatility, and ability to restart mean that we will continue to see different forms of electric propulsion in space. As technology and our understanding of Hall thrusters continues to grow, they will become even more prevalent.

Motivation

While Hall thrusters have been studied since the 1960s and have been in active use since the 70s, our understanding of the complicated plasma physics which govern their operation is still not complete, as well as being a complex and difficult problem to solve, or even simulate. As we learn more about their operation, our goal will be to design more efficient thrusters that allow for less propellant and more payload mass to be carried by the space vehicles, or simply to allow longer operational lives before insulator erosion

terminates the thruster. At the present time simulation models used to predict Hall thruster performance do a fairly good job with steady state time averaged metrics, but they break down when evaluating more complex modes at high data rates such as 500 khz [3]. The purpose for this research is to first, operate the 600 Watt permanent magnet Hall thruster in a laboratory environment; next, collect data on the Hall thruster at high data rates for both steady state and anomalous diffusion modes that can be used to compare to current Hall thruster models; Finally, to perform analysis on the data to correlate observations and measurements to the different phenomenon taking place. An additional motivator that impacts the larger Air Force is that as the Hall thruster power levels increase, the locations for testing decrease and the cost of testing increases; thus the increased emphasis on modelling [4].

Scope

The focus of this research will be to measure the changes in Hall current, plasma potential, and visible emission from a commercially sourced 600W permanent magnet Hall thruster in a time correlated system at high data rates of up to 500 kHz. These measurements will serve to determine the course of investigation for the cause of noted preferential locations for apparent spoke initiation and also determine the path and distribution by which the spokes translate into the Hall thruster exhaust plume. Comparison of data generated by Hall thruster models to experimental data lies outside the scope of this research.

Experimental Methodology

Experiments will be conducted in AFIT's Space Propulsion Application Simulation System (SPASS) laboratory. The Vacuum chamber used is a 2.5m long by 1.8 m diameter cylinder capable of maintaining pressures less than or equal to $3 \cdot 10^{-7}$ Torr with no gas flow into the chamber, or approximately $3 \cdot 10^{-5}$ Torr with a thruster operating. Building from previous research on collecting high speed synchronized data, the Hall current, plasma potential, and visible emissions will be collected. This data will then be used to correlate behavior of plasma instabilities, and determine causal relationships between plasma properties and anomalous diffusion modes.

During experiments, the 600W Hall effect thruster will be mounted to a translational stand. The local plasma potential will be measured with an emissive probe, the Hall current will be measured with magnetic field sensors, and visible emissions will be captured with a high speed camera.

One area of special interest is spoke generation location. In prior experiments, the spokes appeared to be preferentially generated in a specific location. Because it is not clear what generates the spokes, the magnetic sensor and emissive probe will be removed from the test stand and only visible emissions will be collected with the high speed camera. The cathode will be clocked in different locations in attempt to identify a causal relationship for spoke generation. If it is seen that the spokes are generated in different locations, then the emissive probe and magnetic sensor will be reintroduced and tests run again to gain more time correlated data on the plasma plume.

High speed imagery will also be used in a temporally correlated sense to view both normal to the channel and normal to the axis of the thruster. In this way, data correlating

how the spoke mode instabilities translate to the central jet of the Hall thruster are expected. We anticipate that this data may be useful in improving higher resolution Hall thruster simulations by coupling the channel and plume behaviors in multiple dimensions with time correlated images.

Experimental Results

When the experiments are run, plasma instabilities will be induced by varying voltage and propellant flow to the Hall thruster and cathode. From prior experiments on a similar Hall thruster, we expect to see breathing mode and spoke generation [5]. As the cathode is clocked to different orientations, it is expected that spokes will emanate from different locations within the Hall thruster. Previous data indicates that there is a preferential location for spoke initiation, about 90 degrees in the E x B direction from the cathode [5]. What is unclear, and one of the things that this research is expected to clear up, is if that location is driven by the location of the cathode or by some feature of the main body of the thruster, such as a magnetic field cusp or surface feature of the insulating liner for the Hall current channel. The data that is collected from these experiments may provide the ability to isolate and determine causal relationships between plasma properties and anomalous diffusion modes. Additionally the methodology developed for the analysis of the data will provide insight about the inner workings of the Hall thruster. What will make this research difficult is the lack of information about the operation of Hall thrusters at high data rates; therefore, many of the frequencies that are identified might not relate to something that is known. Also, because we are limited on the frequency at which data can be collected, it will be tough to discern if the frequencies

being evaluated are actual or aliasing effects of a phenomenon happening at a much higher frequency.

Chapter summary

In the first chapter a brief overview of the research was given which touched on the background, motivation, scope, experimental methodology, and experimental result. In the following chapters, the literature review, methodology, results, and conclusions will be discussed in greater detail.

II. Literature Review/ Background

Chapter Overview

Chapter two will go through the derivation of the ideal rocket equation, plasma physics basics, Hall thruster operation theory, measurement techniques, and finally, how this ties into the present research. The purpose of this chapter is to provide the reader with an understanding of the theory that will drive the experimental methodology and the results that follow.

Derivation of the Ideal Rocket Equation

Any discussion about space propulsion should start with the derivation of the ideal rocket equation - also known as the Tsiolkovsky rocket equation. This is important because it explains the relationship between the energy of the exhaust and the energy of the spacecraft. This begins with an assumption of conservation of momentum. The acceleration of a space craft is due to the momentum exchange, which occurs as propellant is ejected from the thruster at high speed [6].

$$\sum \mathbf{F} = m\mathbf{a}$$

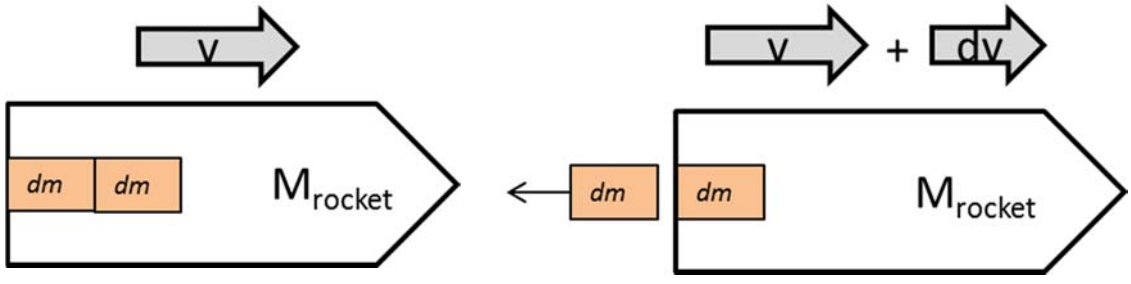

Figure 2: Ideal Rocket

If a close look is taken at Figure 2, it can be seen that the rocket starts with an initial mass and velocity. As the thruster fires, it ejects mass *dm* at a velocity v_e. If the assumption that

no external forces are acting on the system is made, then the total momentum is conserved. Eq. (1) below equates the momentum before and after the burn.

$$mv = (m - dm) * (v + dv) + dm(v - v_e) \quad (1)$$

By expanding these terms and neglect the higher order terms, we arrive at Eq. (2)

$$mdv = dmv_e \quad (2)$$

If we examine this over time, *dt*, we arrive at Eq. (3)

$$m\frac{dv}{dt} = v_e\frac{dm}{dt} \quad (3)$$

Where $\frac{dv}{dt}$, or change in velocity over time is acceleration (a), and $\frac{dm}{dt}$, or change of mass over time is mass flow ($\dot{m}$) yielding Eq. (4).

$$ma = -v_e\dot{m} \quad (4)$$

This means that the rocket's increase in momentum is equal to the exhaust momentum in the opposite direction. The force that results from this change in momentum is defined as the thrust:

$$T = v_e\dot{m} \quad (5)$$

We will now rearrange and integrate

$$\int_{v_0}^{v_f} dv = -v_e \int_{m_o}^{m_f} \frac{1}{m} dm \tag{6}$$

Carrying out this integration and simplifying yields Eq. (7).

$$\Delta v = v_e \ln\left(\frac{m_o}{m_f}\right) \tag{7}$$

This is the ideal rocket equation for free space [6]. If we evaluate this equation in the context of Hall thrusters, one can begin to see why they are advantageous for on orbit maneuvers. For a chemical rocket engine, we typically see exit velocities on the order of 3000 m/s; thus, they require a large amount of propellant when compared to a Hall thruster, which has exhaust velocities on the order of 20 km/s, to achieve the same change in vehicle velocity.

An additional equation that is useful for characterizing rocket performance is Eq. (8) [7].

$$I_{sp} = \frac{T}{g_o \dot{m}} = \frac{v_e}{g_0} \tag{8}$$

Specific impulse, or I_{sp}, is measured in seconds and is the thrust per unit weight flow. For all I_{sp} calculations, we use g_o, which is a constant equal to the Earth's gravitational acceleration at sea level, $9.80665\frac{m}{s^2}$ [7].

This combined with equations 5 and 7, enable the conversion from propulsion system performance in terms of I_{sp} and thrust to mission performance in terms of the ΔV and propellant mass.

Theory of operation for a Hall thruster

A Hall thruster is an electro-static propulsion device. Figure: 3 shows a basic cutaway of a Hall thruster.

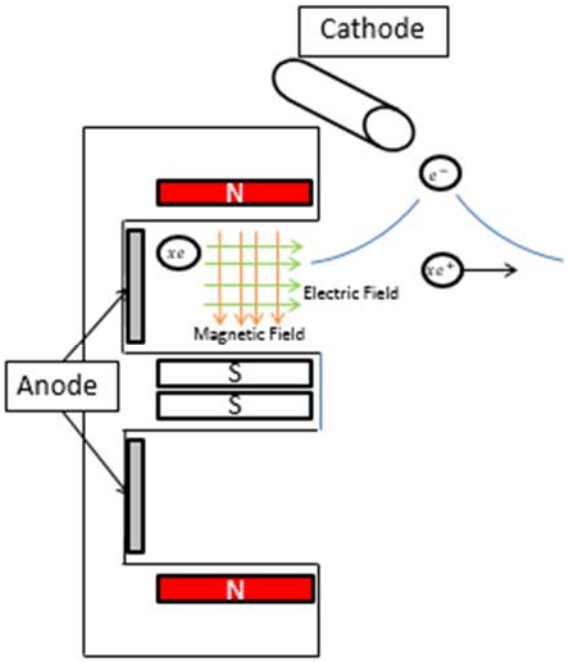

Figure: 3 Hall Thruster Cutaway

The four major parts to a Hall thruster are the anode, propellant diffuser, and cylindrical channel surrounded by magnets on both sides (can be permanent or electromagnetic). In addition to the thruster, a cathode is needed to supply electrons for the Hall current and to neutralize the ion beam. A power processing and conditioning unit is required to take the spacecraft power and convert it to the power required for the Hall thruster. It is important to mention the power processing unit and cathode because there are significant weight, thermal, and power penalties associated with electro-static means of propulsion that are not always seen if we just evaluate the thruster.

The theory of operation for a Hall thruster is as follows: there is a radial magnetic field created from the inner and outer magnets and an axial electric field established between the anode and cathode. As electrons are emitted from the cathode, they are pulled towards the anode. As they flow through the magnetic field, they get trapped and pushed in the E x B direction.

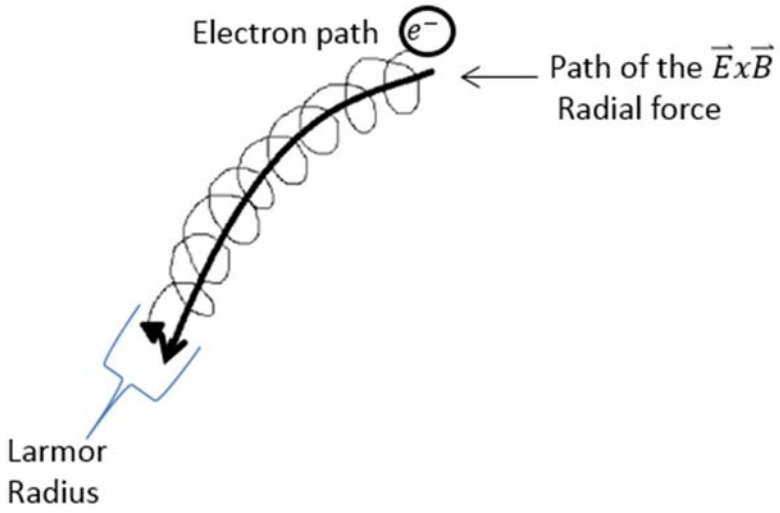

Figure 4: Hall Current

This electron motion is called the Hall current. As more and more electrons are trapped in the Hall current, a swirling cloud of electrons moving at thermal velocities in excess of 200,000 m/s is created. While this is happening, xenon is being introduced from the anode side of the Hall thruster. As the xenon drifts into the electron cloud, the atoms are impacted by the electrons. This electron bombardment removes electrons from the xenon particle causing it to ionize, and the expelled electron adds to the electron cloud. Once ionized, the xenon is propelled out of the thruster by the applied electric field. The xenon ions are not trapped in the Hall current because the Larmor radius is longer than the

channel length. This is due to the mass of the ion being considerably larger than that of the electron. Therefore, the force of the magnetic field has less effect on its path. Downstream from the thruster, electrons emitted from the cathode will neutralize the ions. Theory for cathode operation follows next.

The theory of operation for a hollow cathode is as follows: As discussed previously, ions are generated and then propelled out, generating the thrust in the Hall thruster. The result of this operation is a negative net charge on the spacecraft. This makes the neutralizing cathode necessary, since if the charge is not neutralized, the ions will make their way back to the spacecraft, negating the thrust produced by their expulsion. There are various types of cathodes used in practice to neutralize the beam; this research will focus on the hollow cathode. In its most basic form, the hollow cathode is made up of a hollow cylinder with a cap containing an emitter orifice. Inside the tube, is a low work function insert. The low work function insert is key to the efficient operation of the cathode because it requires a relatively small amount of energy to remove an electron. A heating wire is wrapped around the tube to provide the necessary energy to ignite the cathode. Once the cathode has been ignited, a neutral gas, in most cases the same propellant, flows into the cathode. Electrons then bombard the neutral gas, creating plasma. After the process of electron bombardment, an ionized particle, and a free electron from the neutral are created, in addition to the original bombarding electron. From there, the keeper, a positively charged electrode, draws the electrons out of the cathode through the emitter orifice, while retaining the positively charged ions. Finally, the positive potential of the xenon ions in the plume pull the electrons to neutralize the plume. The key components of the cathode can be seen in Figure 5.

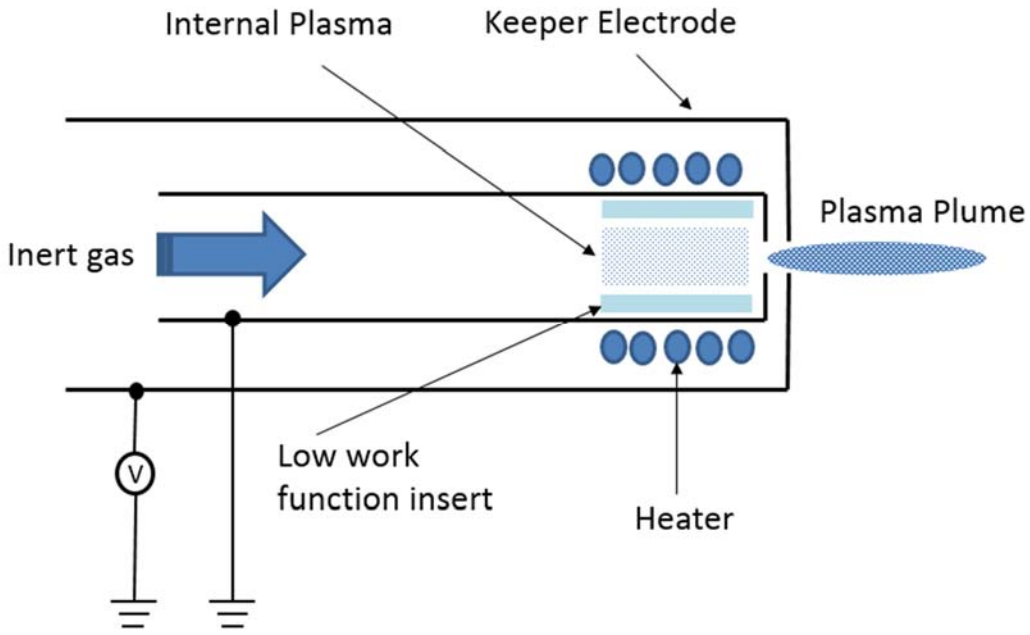

Figure 5: Cathode cross-section

As previously discussed, for a Hall thruster to work, the beam must be neutralized. This means that the beam current of the ions must equal the beam current of the electrons. The voltage required to extract current from the hollow cathode is V_c. We can use the equation below to calculate the cathode coupling voltage.

$$V_d = V_b + V_c \tag{9}$$

Where V_b is the beam voltage, V_d is thruster discharge voltage, and V_c is cathode coupling voltage [1]. V_c can further be evaluated using Ohm's law, which is dependent on the distance based on how the resistance of the plasma changes over distance.

$$V_c = IR \tag{10}$$

By decreasing the distance, the resistance is decreased, which decreases the power supply requirements.

Efficiency and loss mechanisms of a Hall Thruster

The overall efficiency of a Hall thruster is expressed as [1]:

$$\eta_T = \frac{T^2}{2\dot{m}P_{in}} \tag{11}$$

Where T is thrust, $\dot{m}$ is the total mass flow, and P_{in} is the total power input to the thruster. For the present research, the total mass flow is a combination of the thruster mass flow and the cathode mass flow. The input power follows a similar trend, combining the power into the power processing unit and the cathode.

An important consideration for any form of space propulsion is the lifespan of the thruster. This is one area where electrostatic propulsion stands out. This is due to propellant densities and pressures being much less than their chemical counterpart. This leads to very low heat transfer to the walls, even though the equivalent plasma temperatures are on the order of magnitude of a 100,000 K. One area of concern for Hall thruster life is erosion of the thruster channel. This is caused by electron bombardment of the insulation that protects the magnets. During normal operation, the electron cloud will move as illustrated in Figure 6.

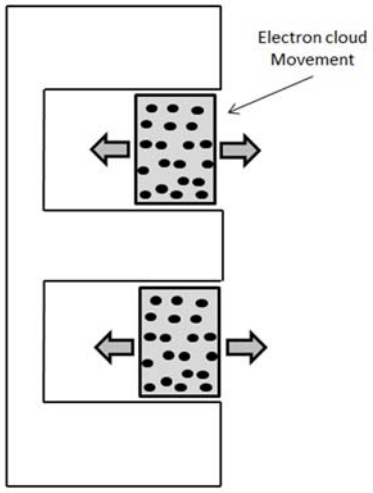

Figure 6: Electron Cloud Movement

As the electrons move in the channel and collide with the walls, they strip off atoms, eventually exposing the electromagnetic coils and shorting them out, which compromises the magnetic field and causes the thruster to stop working in its intended manner. This motion is magnified during the Hall thruster instabilities, which are discussed later in this chapter.

Propellant

The propellants used for the present research are krypton and xenon. Xenon and krypton are desirable as propellants for numerous reasons. Some of the most important reasons are in a launch environment they are not hazardous to handle, combustible, or corrosive. This makes the storage and use of the propellants on spacecraft very convenient when compared to other fuels, such as hydrazine or mercury. In addition, krypton and xenon both have relatively high atomic masses, as well as being stable in their most common isotopes, when compared to the other noble gases such as argon with

an atomic weight of 39.94 or radon with a half-life of 3.82 days in its most likely isotope [8]. The increased atomic mass results in the ability to produce more thrust for a given input power, while stable isotopes can be stored for long periods of time without changing composition. Both xenon and krypton are storable at high pressures, requiring less spacecraft volume be used for fuel storage. Finally, when use on orbit they do not require a tank heater for operation, resulting in a more robust and simpler fuel delivery system when compared to some other propellants. For electric spacecraft propulsion, xenon is the best choice out of the two because its atomic mass is higher and it requires less ionization energy; but due to the cost of xenon, the choice for many laboratory experiments is krypton. Initially, a considerable amount of effort was spent to test the thruster on krypton in an attempt to minimize the cost associated with testing while the experimental methodology was being developed. This would prove to be very problematic and the propellant was switched to xenon exclusively. Additional details on the issues and solutions are found in subsequent sections and chapters.

Plasma fundamentals

Plasma is a state of matter that is defined by particle ionization. This state occurs when atoms are imparted enough energy that they can no longer retain the required electrons to remain a neutral species. In the case of Hall thrusters, the medium that is ionized is the propellant gas. The two propellant gasses used for the present research are krypton and xenon. The associated ionization energies for the two gasses is shown in the table below [1].

Table 1: Ionization energies

Ionization energy for select gasses	
xenon	12.129 ev
krypton	13.999 ev

An additional constraint placed on plasmas is that the collection of ionized gas and electrons must remain neutrally charged globally, this is known as a quasi-neutral state [9]. Local deviations from this charge neutrality do occur and are manifested in anomalous diffusion modes of Hall thrusters, which are discussed later. Some additional concepts that are useful for understanding plasmas and Hall thrusters are Debye length, cyclotron frequency, and Larmor radius.

The Debye length, named after the Dutch scientist Peter Debye, is the distance over which a significant charge separation can occur. For example, if a negative charge is placed in a neutral plasma, the electrons will be repelled and the ions are attracted. This motion is called Debye shielding and creates a polarization that will shield the plasma from the test charge. The length of the shielding is the previously mentioned Debye length which is given in the equation below [9].

$$\lambda_D = \sqrt{\frac{\varepsilon_0 k T_e}{n_0 e^2}} \tag{12}$$

This is important in understanding the behavior and performance of Hall thrusters because these boundaries represent the physical interface through which energy and particles enter and leave the plasma of the thruster [1].

The cyclotron frequency is the uniform circular motion around a magnetic field line and can be calculated with the equation below [9].

$$\omega_c = \frac{|q|B}{m} \tag{13}$$

Where q is the charge, B is the magnetic field strength, and m is the mass of an electron. This is of great importance because the radius of this oscillation is the Larmor radius, which plays a critical role in thruster design. The Larmor radius is a result of the centripetal force that the electron feels as it orbits the magnetic field line. One can calculate this radius with the equation below where $v_\perp$ is the tangential velocity of the electron given by Eq. (14) derived from Maxwell's equation,

$$v_\perp = \frac{V}{e^{i\omega_c t}} \tag{14}$$

and ω_c is the cyclotron frequency [1].

$$r_l = \frac{v_\perp}{\omega_c} \tag{15}$$

If one takes a closer look at Figure 6, the grey boxes that represent the boundary of the electron cloud also represent the space with which the Larmor radius must fit. In general, the Larmor radius needs to be much less than the width of the channel. This will minimize wall erosion of the thrusters, extending the useful life.

Photon emission of propellant gasses

A useful concept to understand when diagnosing problems with Hall thrusters is photon emissions for different gasses. For ease of explanation, helium will be used as the example gas, but the concept can be applied to other gasses such as krypton and xenon. As the hydrogen atom absorbs energy (electron bombardment in the case of Hall thrusters), it will reach different energy levels, or if enough energy is absorbed the

electron will be separated from the atom all together, thus ionizing the atom. If we look at a simplified hydrogen atom as an electron orbiting a proton such that the electron's wave function makes 3 oscillations upon returning to its base state, we can then calculate the associated energies. This is shown in Figure 7.

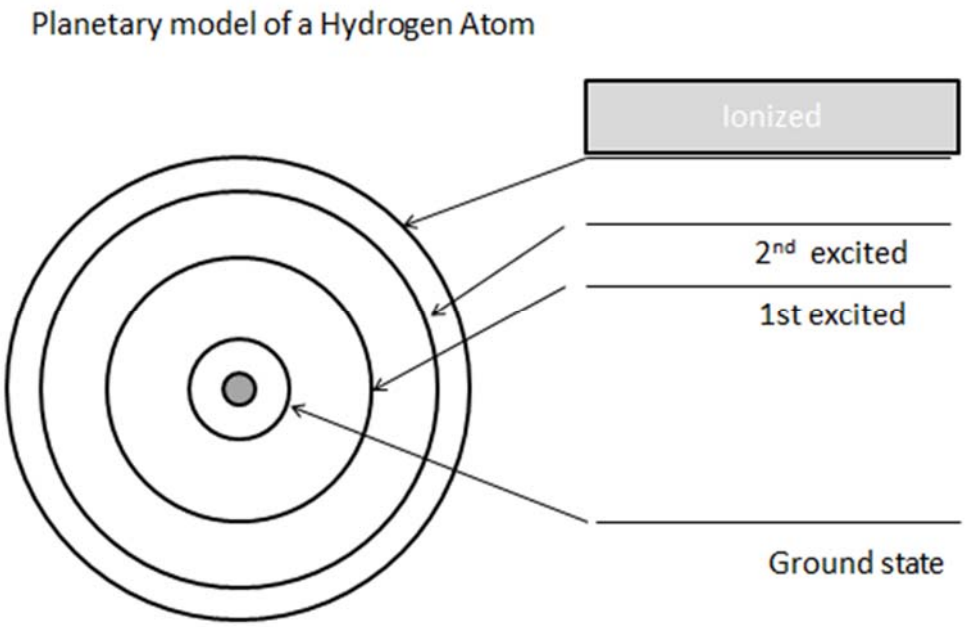

Figure 7: Model of a Hydrogen atom

Because energy levels above the base state are unstable, when the hydrogen atom is at an excited state, it will want to release energy to make it back to its base state [10]. The photon that is released as the electron makes its quantum leaps between the different states are at specific wavelengths. The table below lists hydrogen's visible emission lines, with the bolded/ italicized wavelengths being the high intensity wavelengths [11]. It is also worth noting that Hydrogen also emits in the UV range as well, but equipment used in the present research cannot detect those emissions.

Hydrogen											
Air Wavelength (nm)	383.5384	388.9049	397.0072	410.174	***434.0462***	***486.1279***	***486.1287***	***486.1362***	***656.2711***	***656.2725***	***656.2852***
Color Aproximation	Violet					Blue			Red		

Figure 8: Hydrogen Emissions

Based on the wave length we can calculate the energy that was imparted on the atom using the method below. This method will not give us precise energies due to the spacing between energy bands, and because energy states rarely fall from high energy states directly to the ground state, but it will give us a rough order of magnitude, which will be useful when diagnosing problems. In order to make this estimation, two basic equations are combined

$$E = h * v \tag{16}$$

$$v = \frac{c}{\lambda} \tag{17}$$

giving Eq. (18) [12].

$$E = h * \frac{c}{\lambda} \tag{18}$$

Where E is the associated energy of the photon, h is Planck's constant, c is the speed of light in a vacuum, and λ is the wave length. The energy is then divided by the elementary charge to give units of electron volts. This value can then be compared to the ionization potential for the different propellants with the limitations from above taken into account.

Hall thruster instabilities

In this section, Hall thruster instabilities, which are important to the present research, will be discussed. Additional instabilities exist and are mentioned, but further analysis is outside the scope of the present research.

Anomalous diffusion mode

Some electrons will travel back to the anode of the thruster, as this is required to maintain neutrality of the plasma and spacecraft, but experiments have shown that there is a larger follow of electrons than is expected. The reason why this is such an active area of research is because it is still not well understood, and when these modes are observed it is correlated with a decrease in thruster efficiency and increased wear on thruster surfaces, shortening the life of the thruster [1] [5] [4].

Breathing mode

Breathing mode manifests in a thruster as a cyclic increase and decrease in optical intensity, discharge current, plasma potential, and the magnetic fields within the thruster and plume channel. This will also cause the Hall current region to move within the thruster channel, as shown in Figure 6. This is caused because the process which creates plasma by moving electrons across the magnetic field through collision diffusion, is an unstable process. When a small deviation from the steady state operation occurs, the system does not return to the initial condition, but instead begins to oscillate. The oscillation amplitude will increase exponentially with time, but as the oscillation amplitude increased, the amplitude of these oscillations is limited by the diffusion coefficient. During the oscillations, the diffusion coefficient rapidly increases as the

electrons move across the oscillating electric field, which in turn dampens the exponential increase in amplitude [13].

Spoke mode

Spokes are defined as rotating areas of increased electron density which are seen as optical emissions traveling around the thruster channel in the $\vec{E}x\vec{B}$ direction. They were first observed by Janes and Lowder in the 60's [14]. The optical emission studied in the present research are thought to be the result of excited ions and neutrals following an electron density wave. The electron density wave drives an azimuthal electric field component which then creates another $\vec{E}x\vec{B}$ drift driving electrons towards the anode [4]. In in Janes and Lowder's research they found an average velocity of the spokes to be 7 km/s [14].

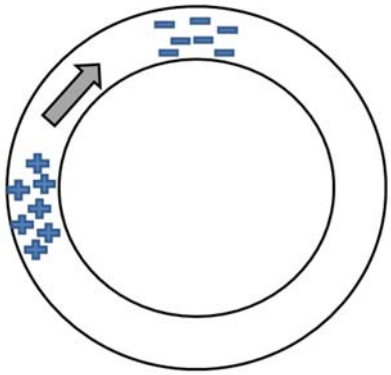

Figure 9: Azimuthal electric field in Hall thruster

Spokes are areas of active research because when present they have a detrimental effect on Hall thruster life and are linked to incomplete ionization of propellant [4].

Cathode location and impact

It is clear that the cathode location is important to thruster performance, and many experiments have been done to show location and alignment have a direct impact on thruster performance [1] [15] [16]. An area of interest for the present research will be to evaluate if and how the radial location of the cathode influences the location of spoke generation. In prior research, a preference for spoke generation was shown in the lower half of the thruster (-180° to 0°), but it is not clear why this is. With the ability to rotate the cathode around the thruster face, the impact will be able to be determined [5].

Measurement techniques

The three instruments that will be used to measure the local plasma properties in this experiment are hot emissive probes, Hall current sensors, and a high speed camera. In the following paragraphs these different instruments and how they are intended to be used will be discussed.

As previously discussed, Hall thrusters generate thrust using an electric field. This makes measuring plasma potential very important when trying to understand their operation. Kemp and Sellen were among the first to use emissive probes in the measurement of plasma potentials. They did this by noting that as emission increases, the floating potential of the emissive probe approaches the plasma potential. For this research, the floating potential V_p will be solved for using the equation below [17] [18].

$$V_f = V_p - T_e ln\left(\frac{I_{s,e}}{I_{s,i} + I_{ee}}\right) \tag{19}$$

In the preceding equation V_f is the plasma potential, $I_{s,e}$ is the electron saturation current $I_{s,i}$ is the ion saturation current, and $I_{e,e}$ is the electron emission current. When the filament

of the floating probe is sufficiently heated with a DC power supply, it enters the regime of electron emission. When $I_{ee} = I_{s,e} >> I_{s,i}$, the floating potential approaches the plasma potential. The probe potential is measured is not exactly equal to the plasma potential because the temperature of the emitted electrons will be less than the electron temperature of the plume, resulting in measurement accuracy on the order of the plasma electron temperature [18].

The magnetic sensor will allow for collection of magnetic field data along multiple axes in multiple radial and axial locations. This technique will allow for the generation of temporally resolved Hall current density maps within the channel for azimuthally uniform operational modes, including the breathing mode. An array of 8 magnetic sensors will be used to measure the Hall current indirectly. They operate using the Biot-Savart law for steady currents, which is defined by the equation below [19] [5].

$$B(r) = \frac{\mu_0}{4\pi} \int \frac{J(r') \text{ x } \hat{\imath}}{\imath^2} \, d\tau' \tag{20}$$

Eq. (20) describes the magnetic field at location $B(r)$ due to current distribution $J(r')$. An important assumption that is made with this equation is that we are operating at steady state. This is only true for the azimuthally uniform modes. Otherwise, the steady current assumption must be revisited. In Eq. (20) μ_0 is the permeability of free space and τ' is the volume which contains all the current elements [19] [5]. From this, we can see how to calculate the magnetic field strength at an arbitrary location given a current at another arbitrary location. Starting with, Eq (20) and make the following assumptions: the current being measured is steady, axisymmetric and intersects the 2 measurement planes we can reduce to Eq. (21) [5].

$$B_r(r)\widehat{e_r} + B_z(r)\widehat{e_z} = \frac{\mu}{4\pi}\oint_{E'} \frac{-J_\theta(r')(z-z')\widehat{e_r} + J_\theta(r')(z-z')\widehat{e_z}}{(r-r')^2 + (z-z')^2} dr'dz' \quad (21)$$

Next we will make the assumption that the total area of integration is divisible into *n* areas of piecewise constant current density. This will allow the currents to be removed from the integration and yields Eq. (22) [5].

$$B_r(r)\widehat{e_r} + B_z(r)\widehat{e_z} = \sum_{i=1}^{n} \frac{\mu J_\theta}{4\pi}\oint_{E'} \frac{-(r')(z-z')\widehat{e_r} + (r')(z-z')\widehat{e_z}}{(r-r')^2 + (z-z')^2} dr'dz' \quad (22)$$

Where the current element being evaluated is represented by the index i. From this point it can be seen that the integral depends on E and the position, which for the present research's case is a fixed geometry. Additional the sensors only measure in one direction thus only one direction must be evaluated. This results in the sensor value being related to the current via Eq. (23) [5].

$$B_j = \sum_{i=1}^{n} A_{ij} J_i \quad (23)$$

Where A_{ij} is a constant dependent on the current element to sensor distance, permeability of space between the current element and sensor, and the size of E_i. The matrix relation for each current element to all sensors can now be shown via Eq. (24),

$$A\boldsymbol{J} = \boldsymbol{B} \quad (24)$$

where *A* is the Green's matrix of constant coefficients relating ***J*** to the column vector of currents at area elements to ***B*** the column vector of magnetic sensor values, which describe the magnetic field distribution [5]. It is important to note that the values of ***B***

from the electric or permanent magnets are accounted for during the calibration process, but the magnetic field generated from the electric field between the anode and cathode is not accounted for. For the present research, the magnetic field will be measured and the current distribution will be backed out. This proposes a problem because prior research identified that simply using least-squares method will not give meaningful data, so some form of matrix regularization will need to be used [20] [5]. The method that was successful and will be replicated for the present research, is the use of Tikhonov's method [20] [5]. Tikhonov's method works by making assumptions about the desired solution based on what is theoretically expected to happen. Tikhonov's Method takes the form:

$$Min[\|AJ - B\|^2 + \lambda^2 \|LJ\|^2] \tag{25}$$

In this equation λ is the regularization parameter and L is the discrete smoothing matrix. The matrix L is determined from the assumptions about the desired solution. In prior research performed by Rubin *et al.* different forms of the matrix L were tested including the identity matrix, corresponding to minimum-norm solution, and different forms of two-dimensional derivative operators corresponding to the continuous and smooth solutions [20]. Finally the following regularizing term was chosen [20]:

$$L = \left\| \frac{d^2 j}{dr^2} J \right\|^2 + \left\| \frac{d^2 j}{dz^2} J \right\|^2 + \left\| \frac{d^2 j}{dr dz} J \right\|^2 \tag{26}$$

The next step that follows is determination of the greens matrix which is discussed in greater detail in the following chapter.

The next instrument that will be used for data collection is the high speed camera. The high speed camera will be used to capture direct photon emission in the visible

spectrum of the plasma from the Hall thruster. The camera in use has the ability to collect images at 1 million frames per second One reason this is an area of interest is because of phenomenon such as spoke mode. This mode is not axisymmetric which makes it hard to measure with just 1 emissive probe and magnetic sensor but by using the high speed camera one can view the entire thruster face and in a time correlated environment tie what is being seen with the emissive probe or magnetic sensor together. One parameter that will have to be taken into account with the optical emissions is based on the camera location, which is in line with the thruster channel. Because of this, the optical emissions seen are the "integration of light throughout the plasma plume" [21] [22]. This means that any phenomenon that happen on top of each other will be combined together and indistinguishable.

Motivation

The primary motivation for the present research is to gain a better understanding of the inner workings of how the different diffusion modes seen in the operation of Hall thrusters work, and provide quality time correlated high fidelity data to modelers. Understanding the under workings for the different diffusion modes in Hall thrusters is important because they directly affect the lifespan of the thruster. By minimizing them through design or operational settings, we can increase the useful life of the thruster. Providing quality data to the modelers is important because it will increase their ability to compare model results to operational results, leading to model validation or improvement. The following chapters will explain the methodology, experimental data, and results for the present research.

III. Methodology

Chapter Overview

This chapter discusses the methodology, experimental setup, and test articles used to generate data. The laboratory equipment and facility details are also described. The procedures used to setup and conduct each experiment are included, and the methods used to reduce the data from each experiment are also described. Evaluation of the data gained from this experiment will aid in our understanding of Hall thrusters, and hopefully aid in design of the next generation of thrusters.

Materials and equipment

The materials and equipment used for the present research are discussed in the following sections.

Vacuum chamber

Experiments were conducted in AFIT's Space Propulsion Application Simulation System (SPASS) laboratory.

Figure 10: SPASS chamber

The vacuum chamber used is a 2.5m long by 1.8 m diameter cylinder that is capable of maintaining pressures less than or equal to $3x10^{-7}$ Torr with no gas flow into the chamber, or approximately $3x10^{-5}$ Torr with a thruster operating. The chamber maintains this pressure using an Oerlikon/ Leybold Vacuum Screwline sp 250 roughing pump, four CVI Torr Master 20 inch TM500 helium cooled cryopumps, and a final helium cooled cryo plate mounted on the chamber ceiling downstream of the thruster.

Inside of the chamber there are two translational stands with three degrees of freedom each. The first translation stand is mounted to the floor of the chamber. The Hall thruster and magnetic sensor are mounted to this stand via a platform made from 80/20 aluminum extrusions. The emissive probe is also mounted to the translational stand, but it will only travel with the translation stand in the X direction. In the front of the chamber there is an additional translational stand, which translates in the X and Y direction and rotates about the Z axis.

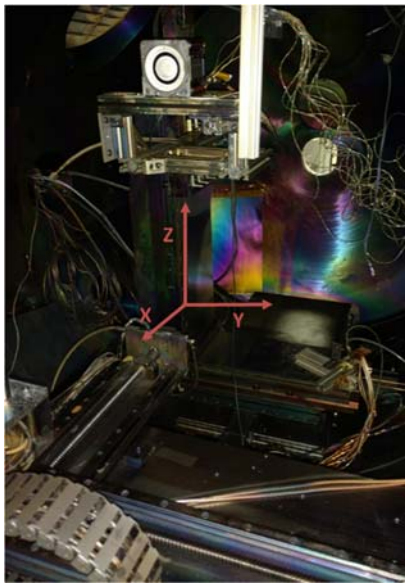

Figure 11: Rear translation stand

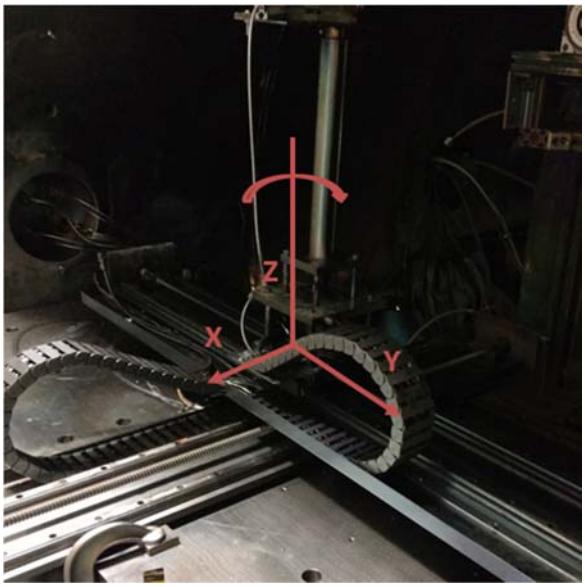

Figure 12: Forward translation stand

Originally, this stand was to be used to hold the emissive probe, but due to other testing taking place, the mounting location of the emissive probe was moved to the rear translational stand and this stand was not used for the purposes of this testing. Located within the chamber walls and doors are seven 25 cm ports. The ports are covered by quartz windows. These ports allows for high-speed imaging in the visible spectrum of the thruster plume while in operation.

Prior to testing, the chamber required some maintenance. This was highlighted in previous testing when the previous thruster under study stopped working. The issue was traced back to faulty wiring. After evaluation, it was determined that it would be more beneficial to completely rewire the power supplies for the chamber.

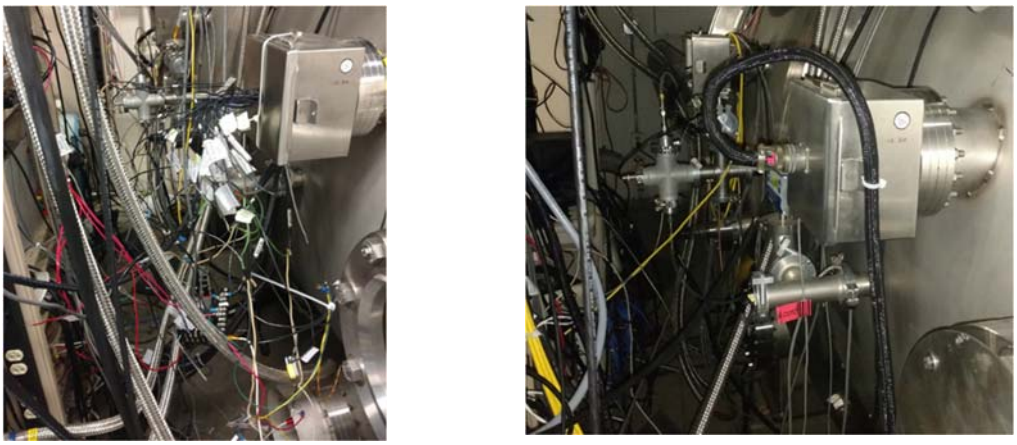

Before (a) After (b)

Figure 13: Chamber wiring before and after

In addition to cleaning up the wiring between the chamber and power supply racks, a pair of patch panels were mounted on the front of the power supply racks to connect the power supplies to the chamber pass through. This can be seen in Figure 14. This allows for easy reconfiguration between experiments and makes trouble shooting much easier.

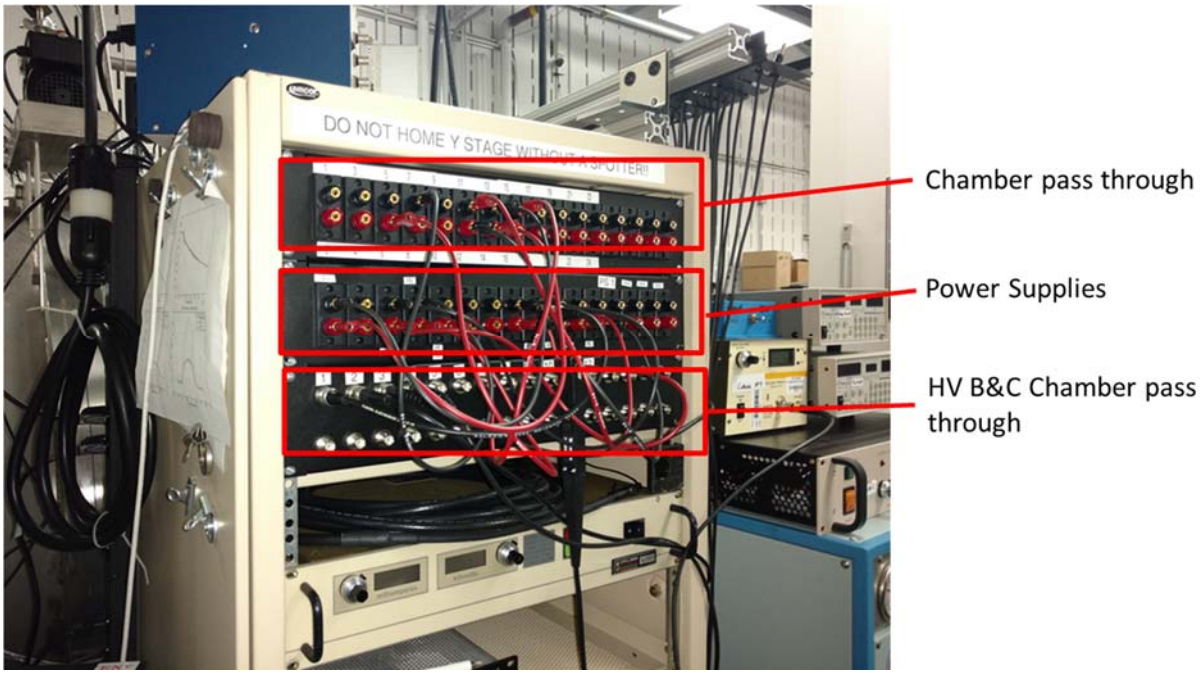

Figure 14: Chamber patch panels

The wiring diagram for the thruster is shown in Figure 15. It is based off of the Hoffman pass through wiring diagram, with the exception of the magnet connections. In the tested configuration, magnet power was not needed because the thruster under study does not have electric magnets. There were some slight variations as testing proceeded due to concurrent testing taking place in the chamber, but care was taken to make sure it did not impact the present research.

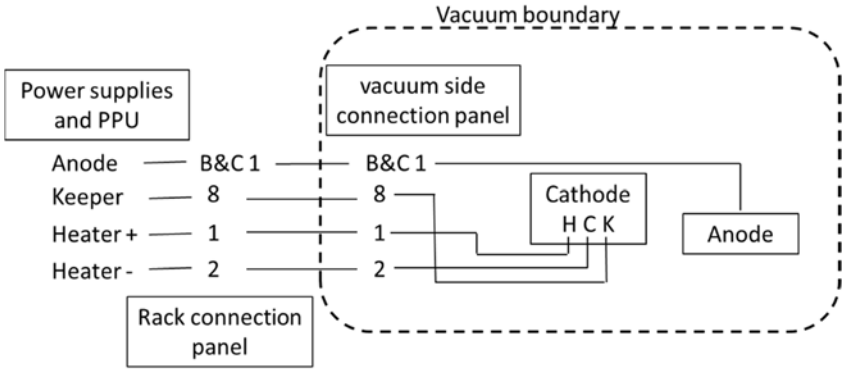

Figure 15: Wiring Diagram

Hall Thruster

The Hall thruster that was used for the present research is a commercially sourced 600 watt permanent magnet thruster, designed and manufactured by Busek; it can be seen in Figure 16. This thruster is designed to provide propulsion to a wide variety of spacecraft ranging from a small 10 kg spacecraft mounted on an Evolved Expendable Launch Vehicle Secondary Payload Adapter (ESPA) ring, to a several hundred kilogram primary payload spacecraft [23]. The I_{SP} of the thruster is approximately 1,500 s depending on thruster configuration, and has an efficiency ranging from 40-55 percent. The thruster is capable of providing up to 40 mN of thrust [23]. These figures do not take into account the cathode; when that is factored in the I_{SP} and efficiency decrease. The thruster is powered by a Sorensen DCS55-55E power supply and the power is regulated through a Power Processing Unit (PPU), also designed by Busek. The PPU has the ability to run the thruster in an automated mode where predetermined settings are used, or in an operational mode where the user can define the parameters. For the purpose of this experiment, the PPU was used in operational mode, and the settings for thruster operation can be found in the subsequent chapter.

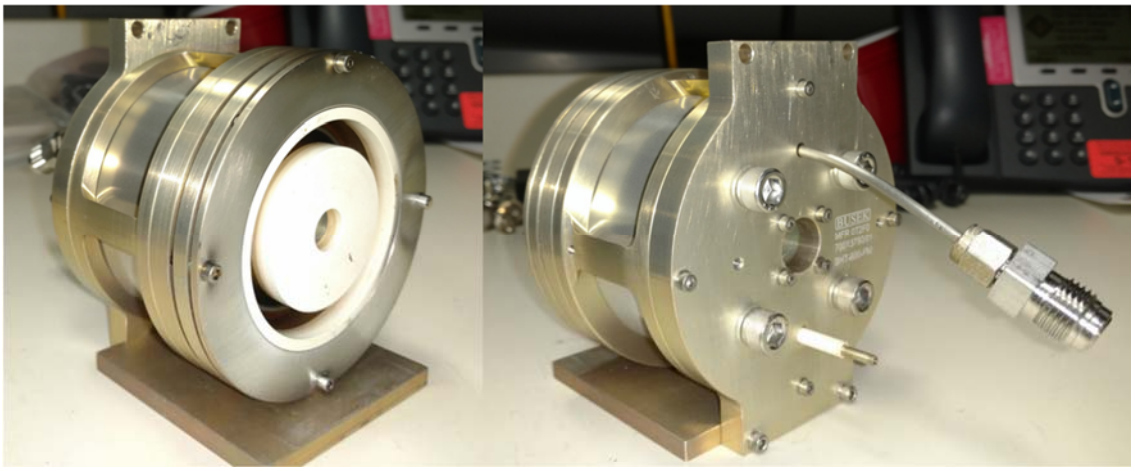

Figure 16: 600W Hall Thruster

The Hall thruster being used was designed for a cathode to be mounted along the centerline of the thruster, but because that cathode was not available, the Busek BHC-1500 was used. This cathode also has flight legacy. It is the same cathode used on the aforementioned TacSat 2 [24]. The BHC-1500 design uses a porous tungsten hollow insert impregnated with a barium calcium-aluminate mixture. The cathode is brought up to temperature by a co-axial tantalum swaged heater wire. The mounting of the cathode to the thruster will be done by a custom bracket designed with help from AFIT's manufacturing subject matter expert and created by the AFIT Machine Shop, which can be seen in Figure 17.

Cad rendering prototype (a) Actual bracket used (b)

Figure 17: Cathode mounting bracket

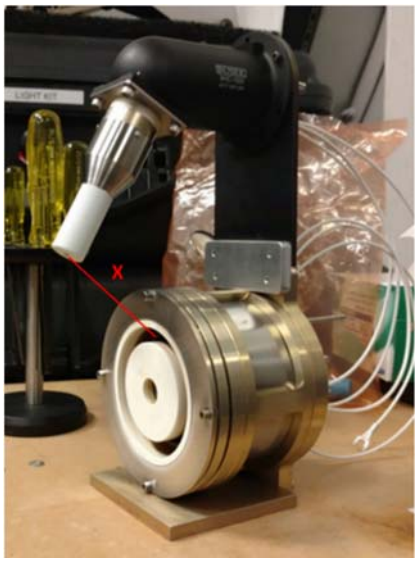

Figure 18: Initial configuration of Hall thruster and cathode

In comparison to how the same cathode was mounted to a 600W electric magnetic Hall thruster of similar design, the X dimension referenced in Figure 18 is 2.5 cm further away for the thruster under study. Initially, it was thought this would be a negligible change and could potentially aid in the reduction of light pollution in the high speed camera data, but as the experiment progressed, the cathode location was changed to make starting the thruster easier. A more in depth discussion on this topic will take place in the next chapter.

Propellant flow control

The Hall thruster and cathode's propellant gas is supplied through two MKS flow controllers, which are controlled by a MKS type 247 4 channel read out. The current configuration of the propellant tanks allows for the use of 99.99% pure laboratory grade krypton or 99.99% pure laboratory grade xenon. This is done by connecting the two propellant tanks parallel to each other with a valve on each tank so that one gas can be selected at a time as seen in Figure 19. Care must be taken when switching between propellants due to pressure difference in the two tanks. For the duration of this testing, the pressure in the krypton tank was 200 -300 PSI higher than the xenon. This required a purge of all of the krypton in the lines before we opened the xenon valve to prevent cross contamination. The pressure supplied to the MKS flow controllers was regulated to 18 PSI by the pressure regulator mounted in line between the flow controller and the propellant selection valves, which is also seen in Figure 19.

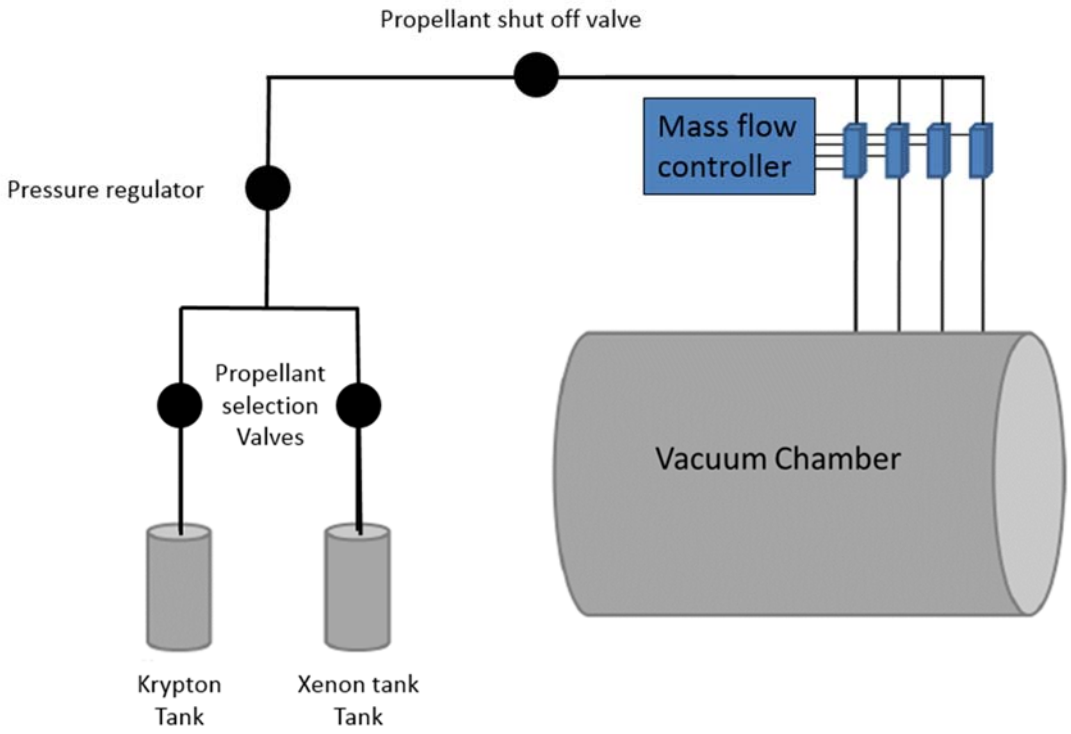

Figure 19: Propellant tank configuration

Emissive Probe:

The emissive probe used for the current experiment is developed by Plasma Controls. The probe consists of $5x10^{-4}$ inch tungsten filament wire loop protruded from a double-bore alumina tube.

Figure 20: Emissive probe tungsten wire loop

Figure 21: Fully assembled emissive probe

The emissive probe will be heated by a potential from a battery floating with the probe. The wiring diagram for the probe is shown in Figure 22.

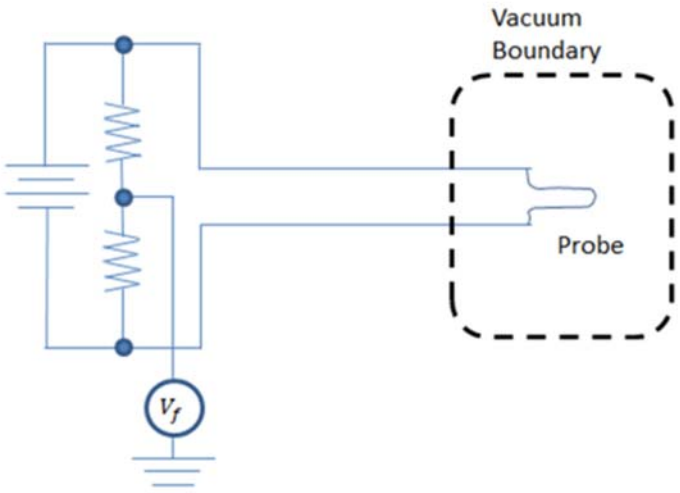

Figure 22: Emissive probe wiring diagram [25]

The probe will be positioned such that it intrudes on the plasma plume and is just downstream from the Hall current channel. The data collection will be done through a Texas Instruments DAQ, and will be triggered by the 5 Volt TTL signal supplied by the oscilloscope. The DAQ uses a LabView program developed by Plasma Controls to filter and store probe readings.

Magnetic sensor: Magnetic sensor overview

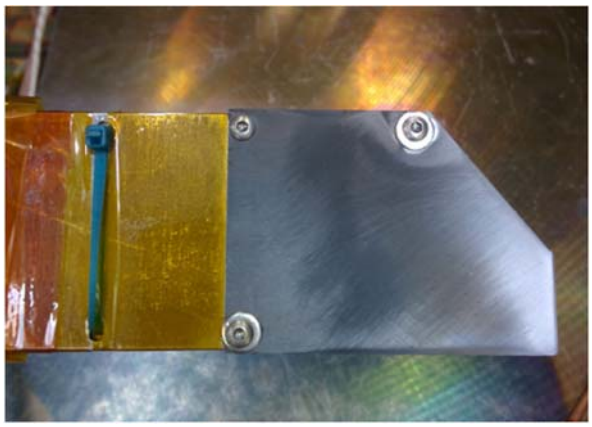

Figure 23: Magnetic Sensor

Measurements of magnetic field fluctuations around the thruster will be performed with a sensor probe developed and constructed by Plasma Controls. The probe uses an 8-sensor planar array of Micro- Magnetics STJ-240 tunneling magnetoresistive (TMR) sensors. There are four sensors mounted in the radial direction and four mounted in the axial direction. In order to obtain data sufficiently above the noise floor of the outermost TMR sensors, it will be necessary to position the probe slightly protruding in the plume of the thruster as seen in Figure 24.

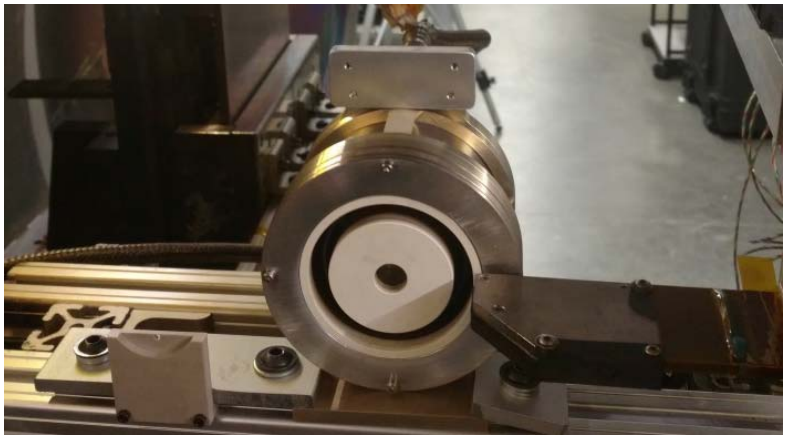

Figure 24: Magnetic Sensor

To protect the sensors from the plasma environment, they are covered by graphite-coated stainless steel housing. This will reduce erosion. The probe will also be connected to the water-cooling system in the chamber to maintain suitable operating temperatures for each sensor while it is protruding in the plume. A Li-ion battery will be used to supply a constant voltage to the sensor array. Figure 23 shows the magnetic sensor in its housing. Sensor output of all 8 channels will be acquired simultaneously by an NI USB-6366 Data Acquisition system (DAQ) at a rate of 2 million samples per second.

Calibration of the magnetic field sensor

In order to solve for the Hall current, the kernel or Green's matrix must be created. This is done by passing known currents within the Hall thruster channel at multiple locations, both axially and radially, while taking measurements. In order to do this, a set of calibration coils and spacers created by Plasma Controls LLC were used. These can be seen in Figure 25.

Figure 25: Magnetic sensor calibration ring and spacers

The current was passed through the coils using a switching box, and while the coil was energized, a measurement was taken. This process was repeated with ten spacers, and at each spacer location, eight coils were individually energized. One issue that arose with the calibration method was accurate placement of the coils. The original thruster which this was designed for utilized a holding mechanism that would not work for the 600W permanent magnet thruster under study. To remedy this, a plastic screw was created that runs through the center of the thruster and has fingers that hold the coil in place. This allows for consistent, even placement. The images in (b)

Figure 26 below show the screw and how it assembles in the thruster.

(a)

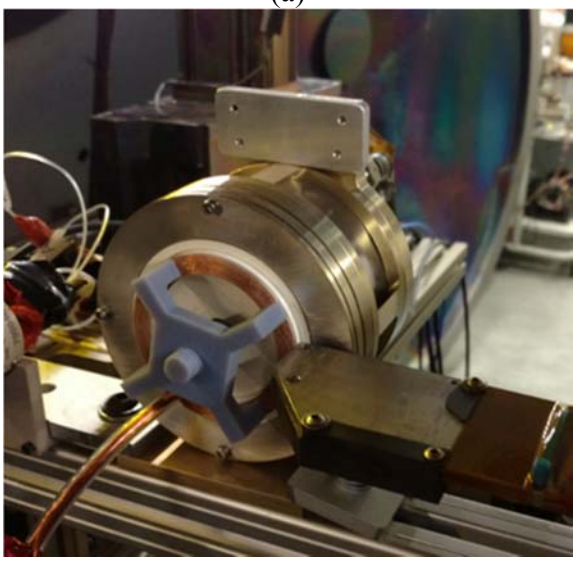

(b)

Figure 26: Magnetic Sensor Calibration Coil Holder

These measurements were then fed into an algorithm created by Plasma Controls, which then produced the Green's matrix used in the analyses of the data.

High speed camera

A Shimadzu Hyper Vision HPV-2 high-speed video camera with a 300mm Nikon lens will be used to capture video of thruster operation. The camera and lens setup used for testing is shown in the figure below. In each recording, the HPV-2 captures 102 frames of 312 - 260 pixel images at rates up to 1 million frames per second (Mfps). The camera will have the f-stop set at its highest setting of 2.4, to maximize the light incident on the complementary metal-oxide semiconductor (CMOS) sensor. The CMOS sensor is sensitive to emissions across the visible spectrum, so resulting images are panchromatic and will be color rendered to make post processing easier [26].

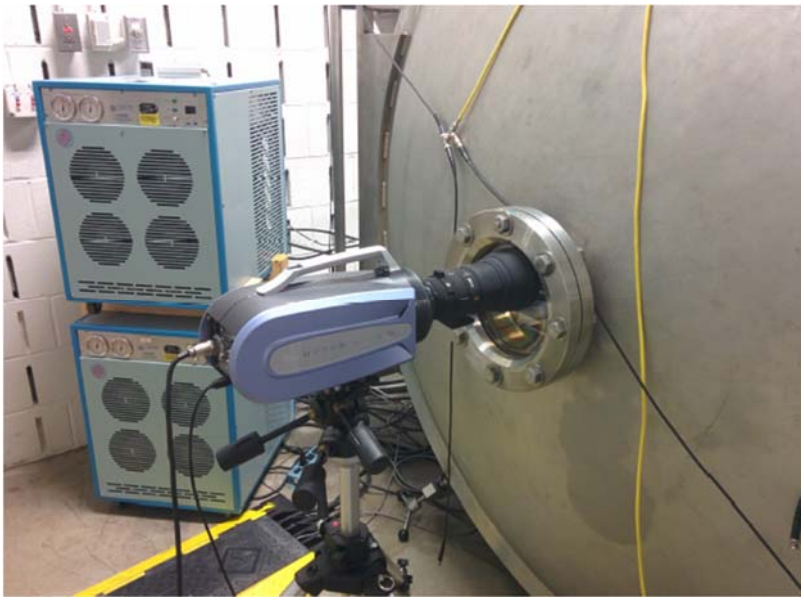

Figure 27: High speed camera [5]

Methodology/ procedures and process

Starting and running the thruster

The starting procedure used for testing is listed in Table 2. This procedure was continuously improved over the course of the experiment and found to be the best way to reliably start the thruster. Once the thruster was set to the desired operating conditions, it

would be allowed to run for 30 minutes before testing would start. This time was determined in previous research to be the amount of time it would take for propellant flow fluctuation to consistently reach the minimum value [5].

Table 2: Cathode and thruster starting procedure

Step	Procedure
1	flow propellant through cathode at 5 sccm for 10 min
2	With propellant flow turned off, apply 2 amps to the cathode heater then wait for 90 minutes
3	Increase heater to 4 amps wait 90 minutes
4	Increase heater to 6 amps wait 30 minutes
5	Increase heater to 6.5 amps Turn on cathode flow 5 sccm Apply .5 amps to the keeper * The voltage for the keeper will start around 600 volts. Once the cathode lights it will drop down to a range of 30-60 volts. If the cathode does not light within 4 minutes then there is a larger problem that will need to be addressed
6	Once the cathode is running, decrease the cathode heater current to 5 amps
7	Turn on propellant flow to the anode, 25 sccm
8	Apply 200 volts to discharge current, wait 1 minute
9	Increase discharge current to 250 volts, and turn off cathode heater after 10 minutes of operation. At this time the thruster should be operating and the setting can be adjusted to their desired values for testing

Mounting of sensors

Figure 28 shows how the different sensors are mounted around the thruster inside the chamber.

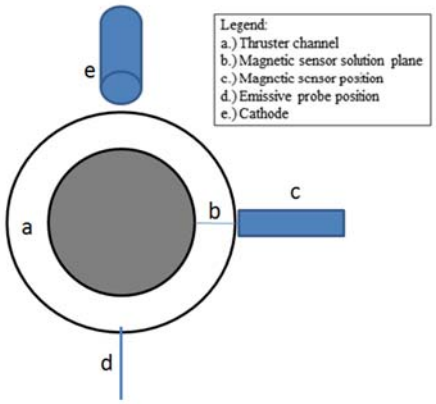

Figure 28: Sensor location around thruster [25]

One issue with this setup is the emissive probe will mask any optical emission located directly behind it from the high speed camera. In order to overcome this, an assumption will be made that the plasma structure will not change from -80 degrees to -90 degrees and data from the -80 degree position will be used for further analysis.

Simultaneous triggering

The collection of data will be triggered by a 5V Transistor-transistor logic (TTL) pulse. The pulse is provided by a Tektronix DPO 4032 digital Phosphor Oscilloscope, which is monitoring the discharge current. The triggering schematic is shown in Figure 29.

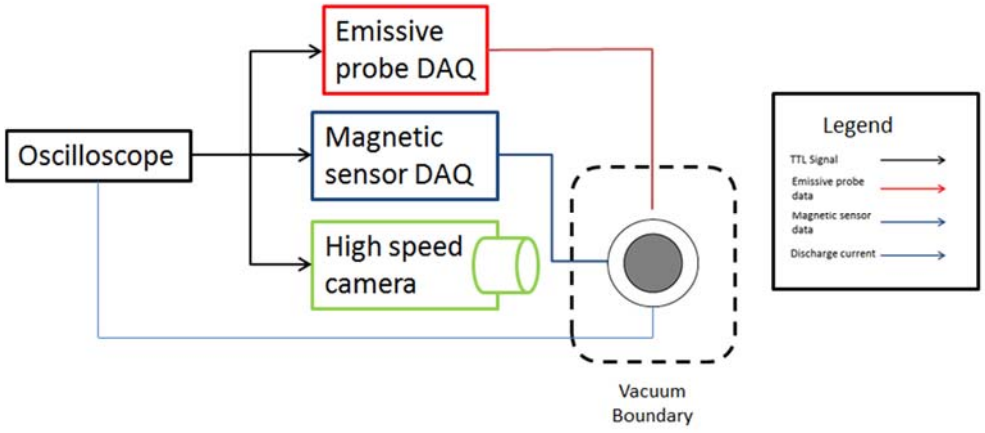

Figure 29: Triggering schematic [25]

The data acquisition will begin based on the rising or the falling of edge of the breathing mode. Based on prior research using the same equipment, the timing uncertainty is shown in table 3 [5].

Table 3: Sensor Timing Uncertainty [5]

Sensor	δt
HPV-2	$\pm 0.5\mu s$
Emissive	$\pm .008\mu s$
Magnetic	$\pm 0.25\mu s$

Experiment synopsis

Due to issues with the chamber, data was not able to be collected on the 600W permanent magnet thruster. In lieu of this, optical data collected from prior research done by Cunningham, using a 600W HET with electromagnets, will be further evaluated. The figure below represents the data that will be evaluated.

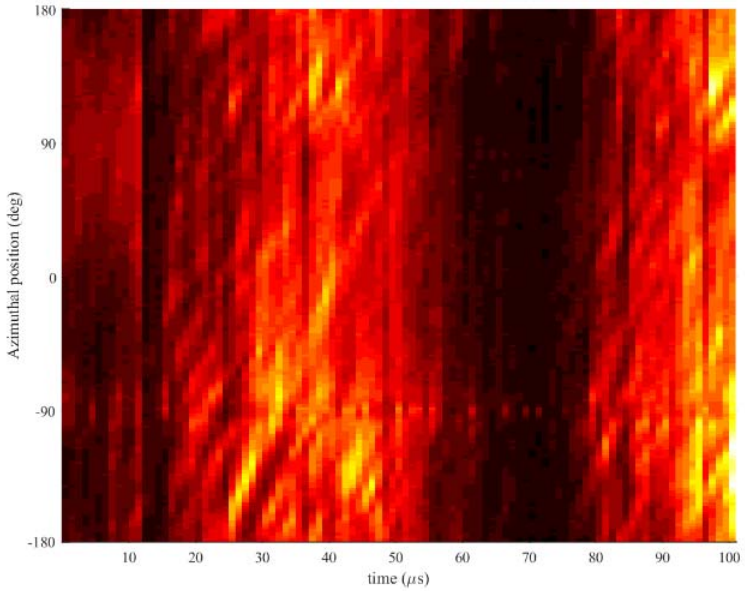

Figure 30: Example of video plot [5]

The figure was created in MatLab® by first breaking the thruster channel up into 180 increments and projecting onto a vertical line. A simplified version of this method is shown in Figure 31. Each pixel of the resulting image represents the averaged brightness of a two degree portion of the thruster channel. This process was done for each frame of the video collected by the high-speed camera, and subsequently, each frame's vertical projection was aligned horizontally to show how the intensity changes in the channel with respect to time. False color was applied in MatLab® to these figures to allow for easier visual examination of plasma structures [5]. Due to how the chart is created, there is a ± 2 degree error with respect to location and $\pm .5\ \mu s$ error due to triggering.

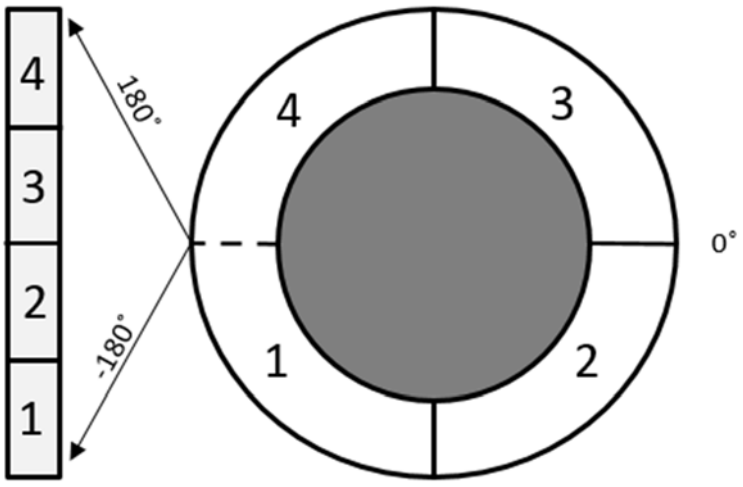

Figure 31: Schematic demonstration of channel projection

One aspect of the figures under scrutiny is the movement of the regions of high intensity over time. This will provide insight about the associated velocity profile and intensity

distribution of the plasma structures. This is a difficult problem because there are many different features occurring at the same time, in many cases on top of each other. The two most obvious are breathing mode, which is represent by the overall cyclic oscillations with respect to intensity of the channel, and spoke mode, which is represented by the higher intensity diagonal lines. There are many other phenomena occurring while the thruster is under operation, but due to the limitations set by the equipment, the frequencies at which they are cycling are not able to be directly analyzed. Another aspect of the figure under study is the frequency associated with each pixel. A discussion on the derivation of the methodology used to perform the different analysis and the results are covered in the next section.

Step through of analysis procedure

The figures under study were saved in a Red Green Blue (RGB) format. This initially posed a problem for post processing because the first method of analysis developed involved converting the image to grey scale, and then analyzing using the Matlab's® image processing toolkit. This did not work because it resized the original 180 × 100 pixel figure to a 500 × 600 pixel image, which resulted in some distortion of the image and alteration of some of the intensities by mixing the borders of the original pixels. Further analysis of the figures under study were conducted, and with aid from other students, a way to pull the intensity that set the scale for the false color, color map was developed. The resulting intensity value matrix was exported from Matlab® to Microsoft Excel for easier manipulation.

The first analysis that was done on the resulting intensity matrix was to evaluate the profile of the spoke intensity as it progressed around the thruster channel. This was done

by first selecting a spoke, and then for each column of the spoke, finding the local minimums in the column of interest around the spoke. Anything below this minimum intensity for the column was excluded from the intensity profile graphs. Each column associated with a spoke was evaluated independent of the surrounding columns. This was necessary due to each row varying in intensity with respect to other rows and each side of the feature varying in intensity. An example of the resulting intensity graphs can be seen in Figure 32. Discussions on the potential reasons for the shape and size of the curves are discussed in the next chapter.

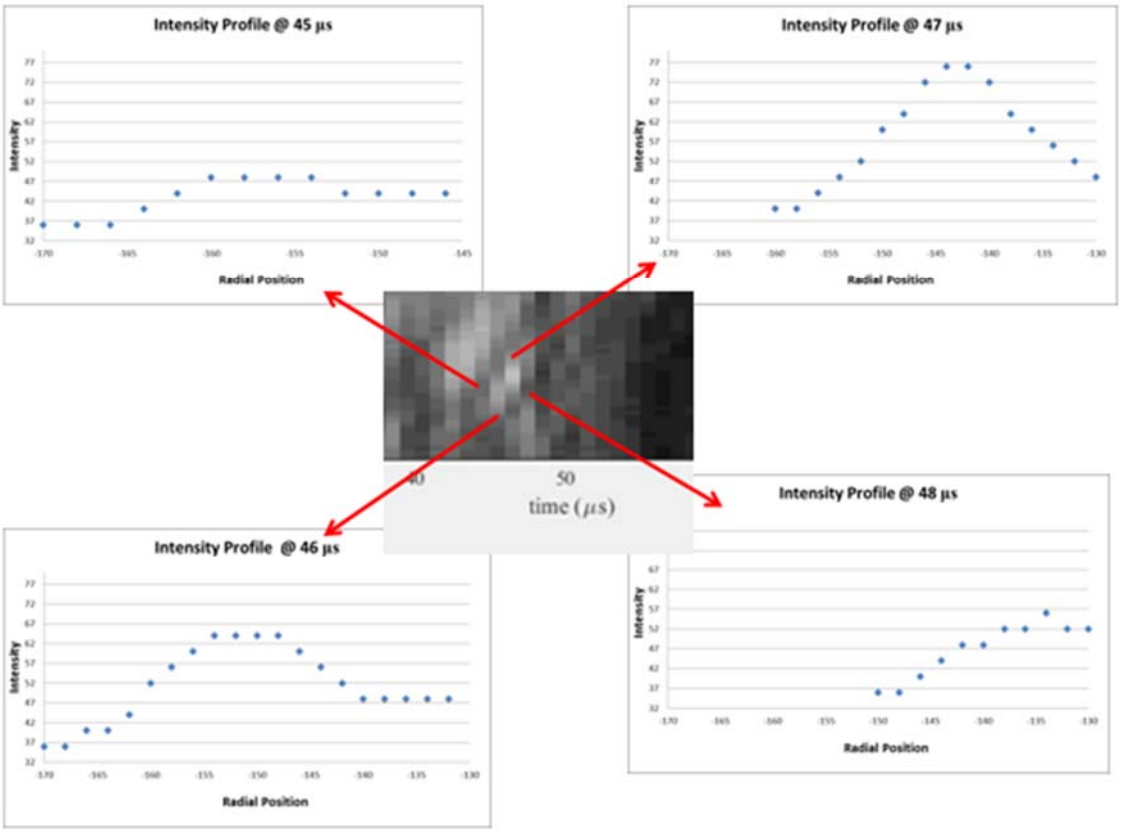

Figure 32: Spoke Intensity Profiles

The next portion of analysis done on the experimental data previously collected was a frequency analysis using the Fast Fourier Transform (FFT) method. This was done with respect to time in order to yield a matrix of temporal frequencies, and with respect to position yielding a matrix of spatial frequencies. The purpose for doing these transformations into the frequency domain is to give us insight on what frequencies are present and prevalent within the thruster. Our evaluation of the frequencies that can be studied are limited by the amount of data points in the figure, *i.e.* frames used to construct the picture and pixels used to construct the channel. This max frequency can be calculated using [27]:

$$\max measurable\ frequency = \frac{N}{2T} \tag{27}$$

In the previous research, there were 102 frames of high speed camera data. Each frame lasted 750ns with a spacing of 1μs between each image. This results in a max measurable frequency of 500 kHz. In the spatial FFT, the max frequency that can be evaluated is 14.32 cycle per revolution. These direct observation limits are hard limits at the present time due to the equipment available for testing. This does limit our ability to directly attribute anything that has a much higher frequency, as a direct cause for the different anomalous diffusion modes seen. One method that can be done to make some suggestions on if we think a high frequency phenomenon is affecting thruster operation, is to use attenuation effects to see if it shows up at a lower frequency. An example of this can be seen in Figure 33. The peaks of the cosine waves represent the center of the frequency bins. If the measurement equipment can only measure between –T and T, but the frequency of interest lies outside of this measurement range, the frequency of interest

cannot be directly measured. What can be done is to look at the smaller amplitude frequencies which are made from the attenuation of the main signal. In the case below, if an important frequency was thought to exist at 2T, 0.5T, or -0.5T, it could be evaluated based on the signal aliasing. As can be seen from the figure, there is a lot of noise associated with signal aliasing. This results in a low confidence that what is seen is the signal of interest, but it does provide a way to select sample rates for future study.

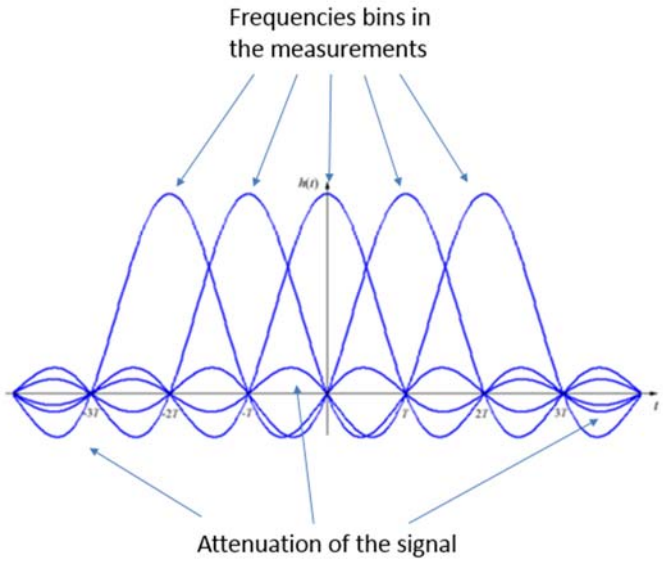

Figure 33: Aliasing explanation [28]

An everyday example of signal aliasing is when a car tire appears to spin backwards in a video. This is due to the actual frequency of tire rotation showing up as an aliased frequency in the video. The methodology used to find the aliasing frequency is below. First, the folding frequency must be found; this is done with the equation below where f_n is the folding frequency and f_s is the sampling rate.

$$f_n = \frac{f_s}{2} \tag{28}$$

Next, the ratio of $\frac{f}{f_n}$ is calculated. Where f is the frequency of interest. The ratio of $\frac{f}{f_n}$ is then found on a folding diagram, such as the one listed in appendix A3 in Introduction to Engineering Experimentation, and the ratio of $\frac{f_a}{f_n}$ can be determined. At this point, the equation below is used to calculate the aliasing frequency (f_a) [27].

$$f_a = \frac{f_a}{f_n} * f_n \tag{29}$$

Results of FFT transformations on the intensity color plot can be seen in Figure 34 and Figure 35.

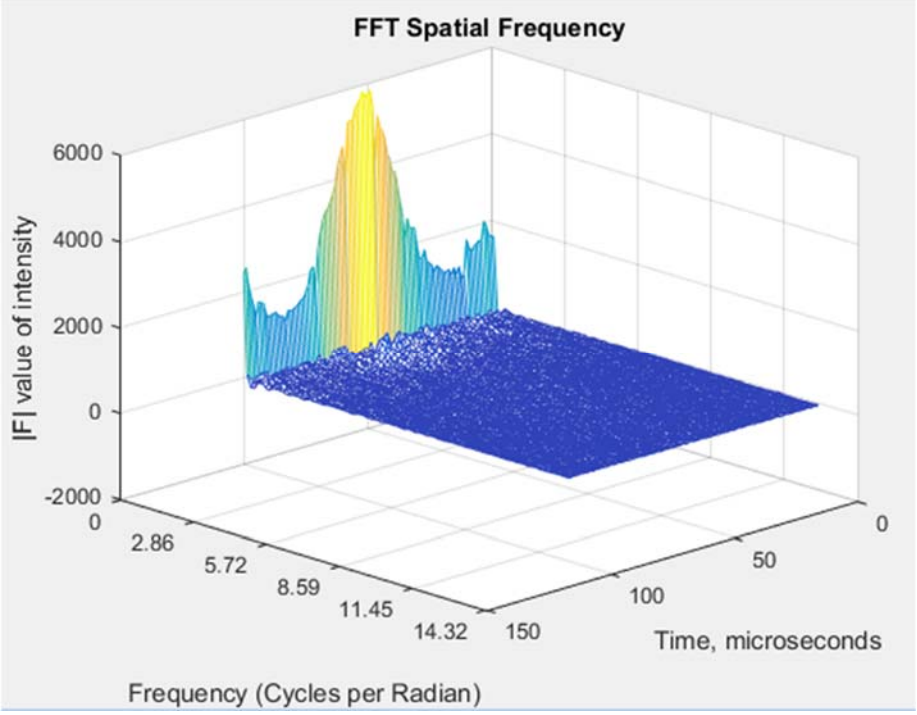

Figure 34: FFT Spatial Frequency Transformation (Unrolled plot 4)

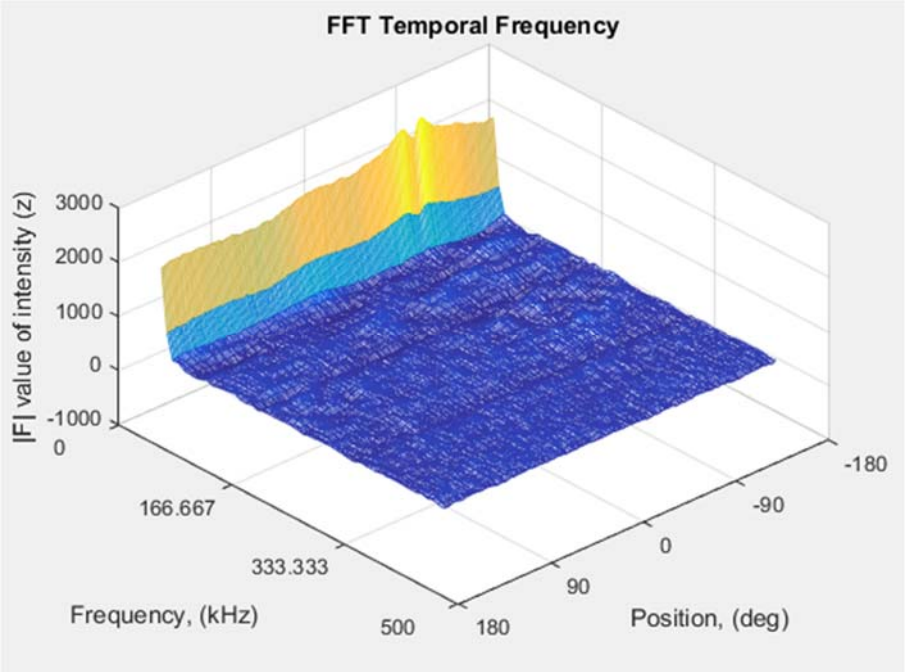

Figure 35: Temporal FFT Transformation (Unrolled plot 4)

The above FFT transformation of the entire matrix is useful for making global observations on thruster operation, but did not allow for in-depth analysis in specific areas of interest, thus the next step was to isolate times or radial positions of interest and plot those. An example of this further break down can be seen in Figure 36 and Figure 37.

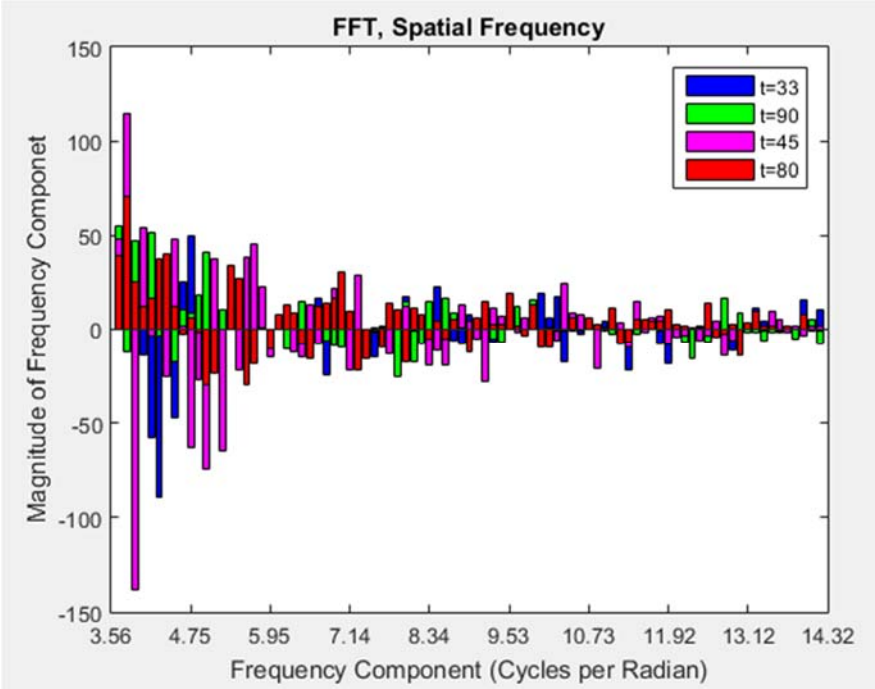

Figure 36: Spatial frequency break down (unrolled plot 4)

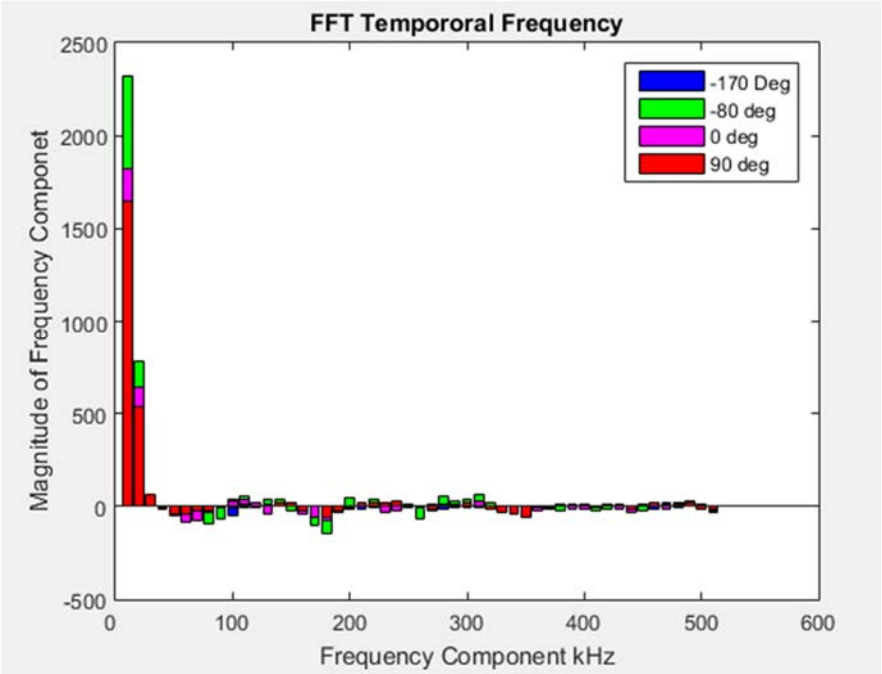

Figure 37: Temporal frequency break down (unrolled plot 4)

Determining signals of interest

As can be seen in the figures above, there are many frequencies seen in the operation of a Hall thruster. One way we can identify a frequency of interest is to count the number of features and divide by the time step. Figure 38 illustrates this process

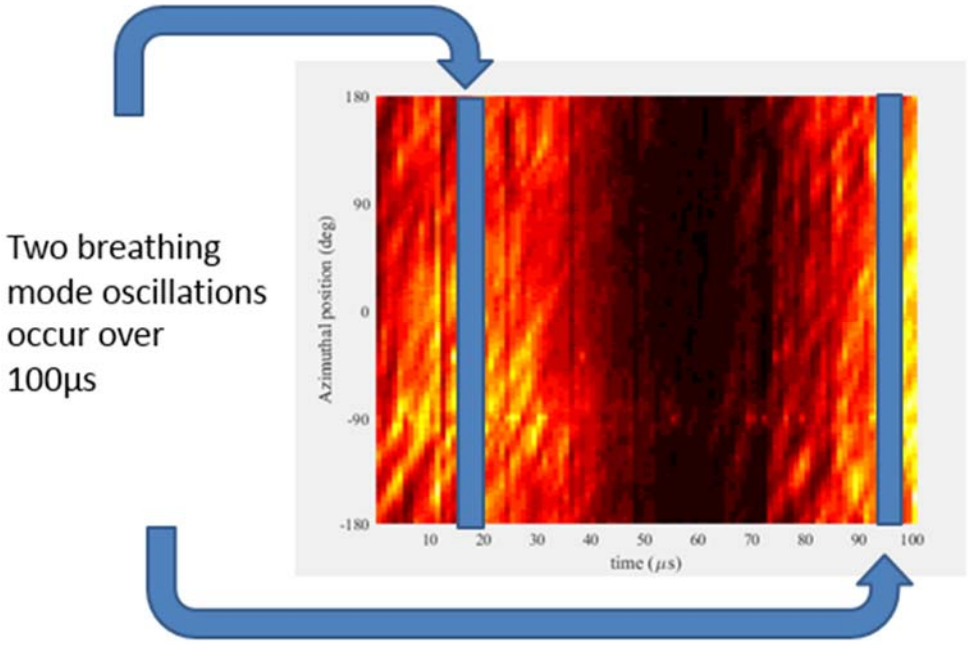

Figure 38: Breathing mode oscillations

In Figure 38, two breathing mode oscillation peaks occur over a time period of 100 µs with a spacing between the peaks of 80 µs. Dividing the two oscillations by the time period separating them yields a frequency of interest of 25 kHz. This measurement can then be correlated to frequency spike in the temporal frequency graph. This same process can be done with both temporal FFT data and spatial FFT data.

Chapter summary

In this chapter, the proposed experimental methodology and methodology for data analysis was discussed. Had the experiment worked, this experimental setup would have yielded optical emissions data from the high speed camera, Hall current variation with respect to time from the magnetic sensor, and plasma potential variation with respect to time from the emissive probe. The issues that prevented the collection of data are discussed in the next chapter, as well as analysis on prior collected data. The implications from data analysis will also be discussed in the subsequent chapters.

IV. Analysis and Results

Chapter Overview

In the previous three chapters, an introduction to the research was given, followed by pertinent information needed to understand the problem, and finally, in the previous chapter, the experimental setup, methodology for running the experiment, collecting data, and a preview of the data analysis were discussed. In this chapter, the problems and solutions of initial testing will be discussed, as well as results from analysis of data previously collect. This chapter will be followed by the final chapter, which will discuss results and recommendations for future research.

Operation of the thruster

When testing started, the chamber had significant issues with wiring, so the first thing done was a complete rewiring of the chamber with respect to the power supplies powering the test articles. After that was competed, a thruster that was known to work was hooked up. After minimal trouble shooting, it was started and run successfully. After the successful run, the thruster under study was hooked up. For the purpose of this experiment, the chamber was pumped down 18 times, and there were 38 separate tests run on the thruster. The thruster was successfully operated 9 times over the period of testing.

Trouble shooting the thruster

Thruster operation will be broken into two parts: running the thruster on krypton and running the thruster on xenon. The reason for this separation is because it provides a

natural break in testing. While operating on krypton, the thruster did not run and while running on xenon the thruster was started.

Operation of the thruster with krypton

The first non-working configuration of the thruster and cathode can be seen in Figure 39 below.

Figure 39: Original cathode location

When the thruster was run in this configuration at manufactures specifications for full power and maximum mass flow for xenon, it resulted in a dim glow around the channel, as can be seen in Figure 40. The specifications for xenon were used as a starting point for running on krypton based on prior experience with another 600 W Hall thruster.

Figure 40: krypton, manufacturer specifications

The initial thought for why the thruster was not working was due to issues with the wiring of the thruster. Therefore, all the connections to the thruster and cathode were checked for continuity, correct current, and correct voltage and from the PPU. These things all checked out, so the next attempt to fix this problem was to increase the mass flow to the cathode and thruster. This was thought of because the thruster was being run on krypton, when it was designed to run on xenon. Based on prior experience with similar thrusters, it was known that there would need to be some adjustment in mass flow between the two gasses. As the mass flows were increased to 20% and 40% above manufacture specifications, the intensity of the optical emissions would increase, but full ionization never happened. Figure 41 shows this operating condition.

Figure 41: Thruster operating 20% above manufactures specified mass flow

The next attempt to fix this was to move the cathode closer to the anode, as seen in Figure 42. Based on the theory listed in chapter two, moving the cathode closer would decrease the power needed to start and run the Hall thruster. The resulting increase in optical intensity can be seen in Figure 43.

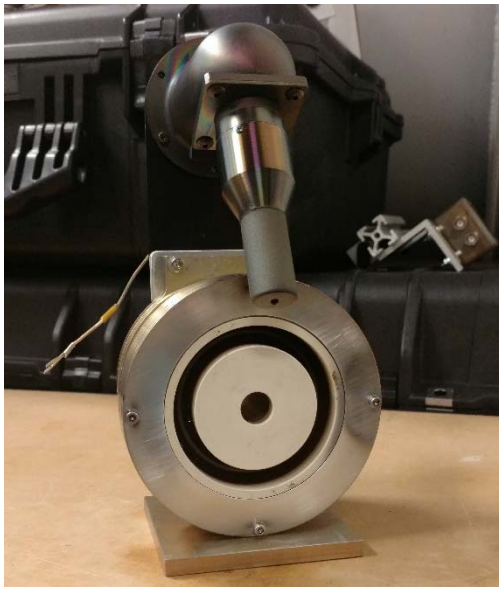

Figure 42: updated cathode mounting position

As noted, there was a noticeable increase in intensity. In the new configuration, brief moments of ionization would take place, but they were not sustained and often resulted in the power supply shutting off. As the mass flow through the cathode and anode were increased from manufacture specifications, the intensity of the light radiated from the thruster channel and the frequency of brief ionization taking place increased.

Figure 43: Thruster operating with new cathode mounting location

While testing in the final physical configuration shown in Figure 42, at the operating conditions listed in Table 4, the frequency at which the thruster would start ionizing the propellant was at its maximum. The resulting current spikes from the short periods of ionization would shut off the power supplies after a few cycles and require a restart.

Table 4: Krypton Operating Parameters

Discharge voltage	300v
Anode mass flow	25sccm
Cathode mass flow	5sccm
Keeper current	0.5 A
Heater current	5A

Due to the length of time the thruster operated, pictures showing the ionization were not possible. It is worth noting, however, after a run at the above operating conditions, the power supply tripped and the PPU firmware was corrupted. Initially, after this malfunction, the thought was there was a problem with the PPU, which was stopping the thruster from operating correctly so new firmware was uploaded and the test was re-run at the above conditions. The results of this test were the same as prior tests with a few cycles of ionization taking place, but the power supplies would eventually trip and require a restart.

After a test which involved many cycles of starting for short periods of time, the chamber was vented and the thruster was evaluated where it was noticed that there were scorch marks on the thruster face. This can be seen in Figure 44. The location for the scorch marks appears to be somewhat random. Two possible explanations for their appearance are:

1 – As the thruster heated up, debris on the thruster face melted and the remnants are etched in the face of the thruster. When handling the thruster, gloves were always worn and care was taken to not introduce contaminants. One event, which could have

introduced contaminates to the thruster surface was calibration of the magnetic sensor. The plastic in the clamp could have slightly embedded in the surface of the thruster. As a result of this observation prior to each subsequent test, if the thruster was handled, it was wiped down with isopropyl alcohol to aid in the removal of any dust or debris as recommended by the operation manual.

2: High energy particles emitted from the thruster bounced off of the walls of the chamber and impacted the thruster surface. Evidence of this can be seen if one looks at where the magnetic sensor is located. Around the sensor the metal is discolored, but under the sensor the metal looks as it did before testing.

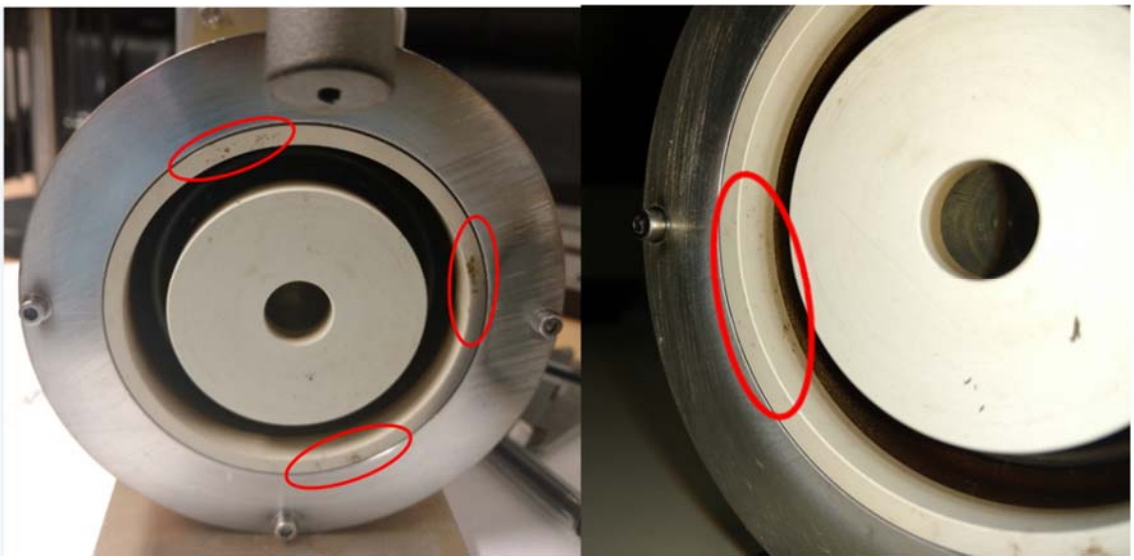

Figure 44: Scorch marks on thruster

The impact of these blemishes is not fully known due to inability to collect data on the thruster. Potential impacts are unknown but might manifest as a preferential starting location for spokes; thus for future study, noting locations of surface anomalies would be important.

Operation of the thruster with krypton synopsis.

As has been stated, initial testing of the thrusters was done with krypton. This yielded significant problems, and the thruster never operated properly. Using equations listed in chapter 2, the energy associated with the light being emitted from the thruster is 2.95 ev and 3.26 ev (violet spectrum). This showns that the krypton is being excited as it flows through the thruster, but we are not imparting enough energy to ionize. A potential reason for this is due to the magnetic field not being strong enough to capture high enough energy electrons; thus the final parameter checked on the thruster, before the switch to xenon was made, was to evaluate the magnetic field strength.

The magnetic field strength was checked twice, first using a Lake Shore magnetic sensor probe at various locations around the thruster channel, and again with a FB Wells 5180 Gauss/Tesla Meter.

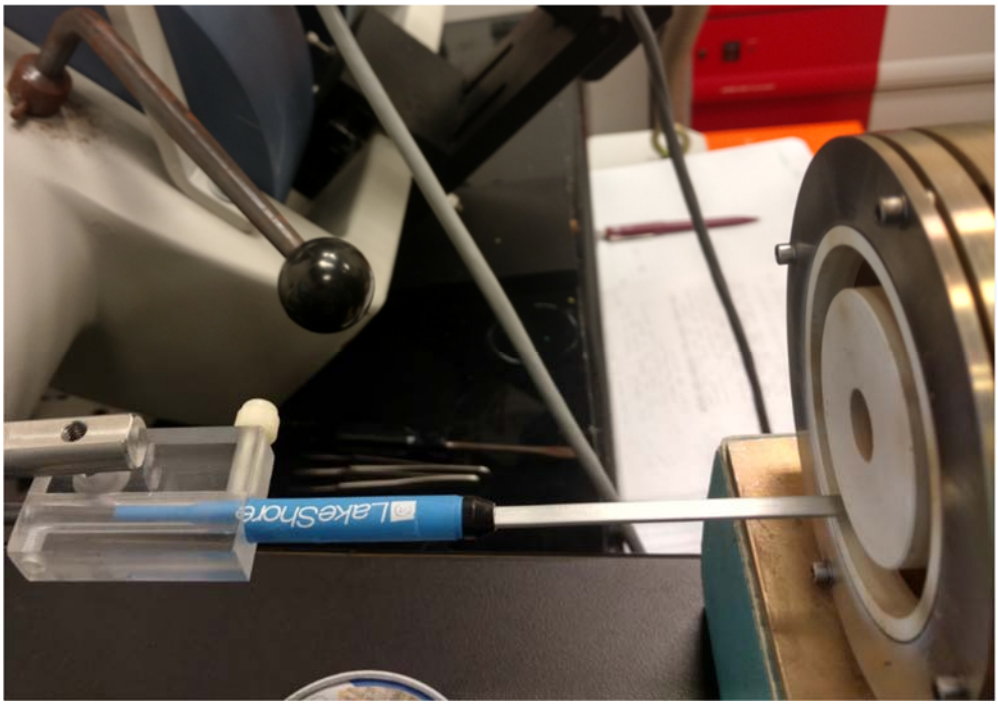

Figure 45: Magnetic field measurement setup

The first method for collecting magnetic field strength was not very precise because the probe location in the channel was not consistent. It did, however give a rough order of magnitude for the field strength, which can be seen in the graph below.

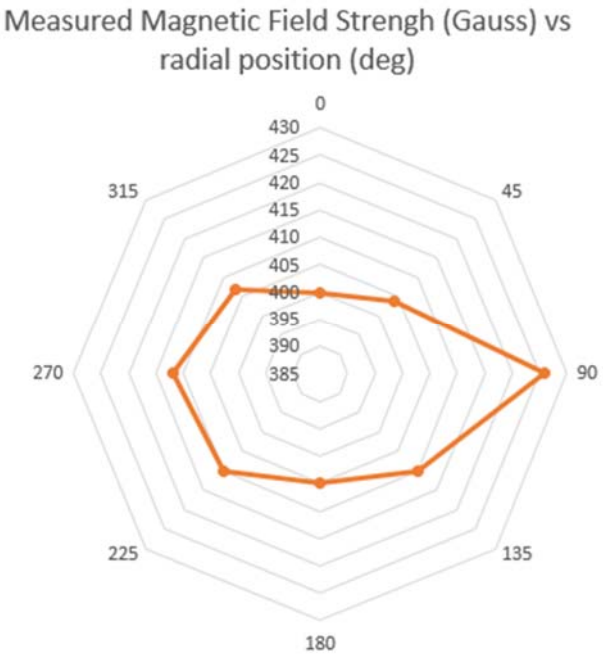

Figure 46: Magnetic field measurements

Based on the inconsistency of the data, it was decided to repeat the measurements. This time a spacer was used to keep the location in the thruster channel consistent with respect to axial location and depth. The results can be seen in Figure 47. One area of concern is the deviation between the two measurements. This is due to a different magnetic field sensor being used. The second sensor was a hand held Gauss meter that was less accurate than the first, and the sensor was initialized next to the vacuum chamber, which could have thrown off the magnetic field strength measurements.

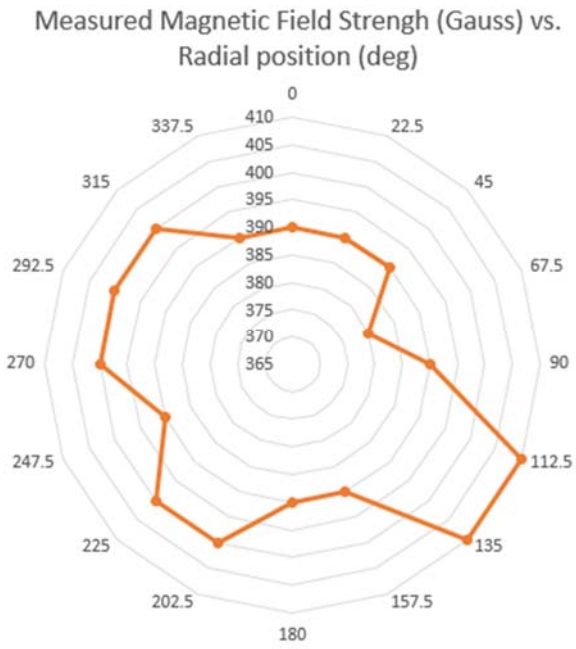

Figure 47: Magnetic field measurements

After comparison of the two results, it was noted that magnetic field strength deviations were consistent, 26 Gauss for the first measurements and 30 gauss for the second measurement with an error of ±.1 Gauss from the meter and ±20 Gauss depending on location of probe in thruster channel. Based on the potential error from the measurements, it was determined that the deviations between the measured magnetic field strength and advertised magnetic field strength of 400 Gauss were not off enough to cause the thruster to operate incorrectly thus it must be another problem.

Operating thruster with xenon

The final parameter which was changed that allowed the thruster to operate was the switch from krypton to xenon. After the switch to xenon, the thruster started almost immediately. We can tell the thruster is running correctly based on the optical emissions

shown in Figure 48, and if one looks at the center of the thruster where the jet plume from the annulus interacts with itself. The operational conditions for this test are listed in chapter 3.

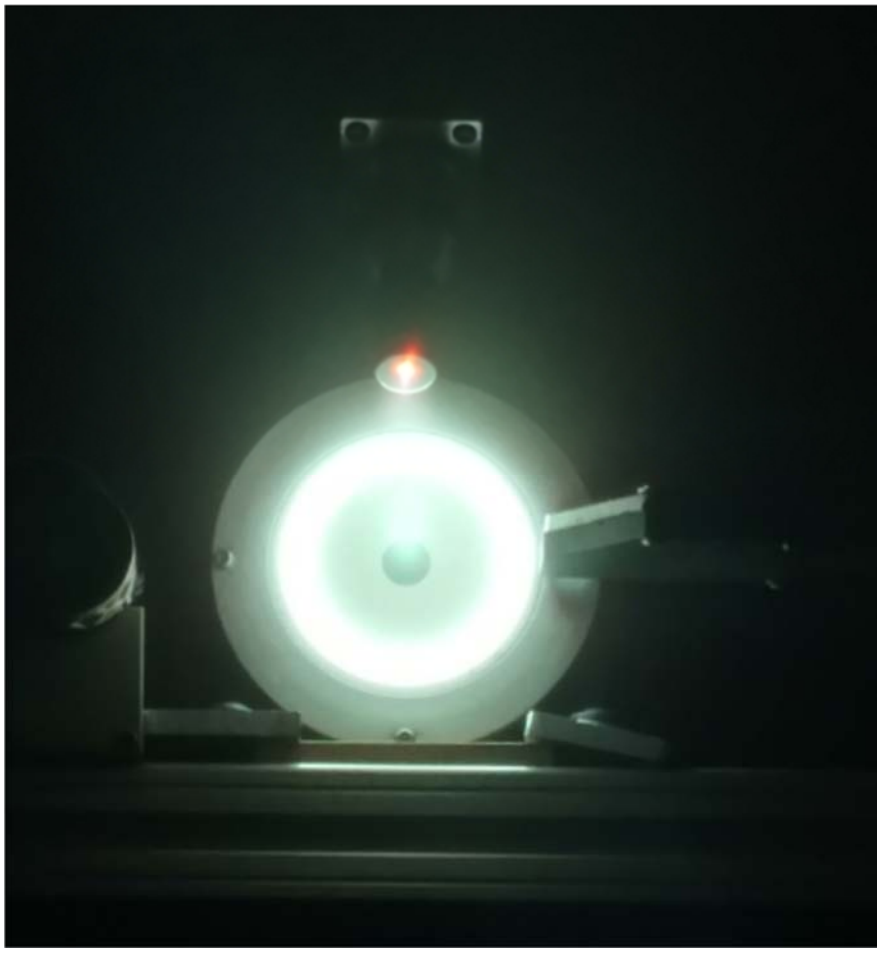

Figure 48: Thruster operating on xenon

Chamber issues

Shortly after the issues with the thruster were sorted out, the chamber started to act up. Initial problems were the pumps were overheating and shutting off or tripping a breaker in the control box. When all the pumps were in operation and the thruster was running, it was noticed that the pressure increased above the safe operating limits of the

thruster. Pressures for three subsequent tests are shown in the table below. These pressures were reached between 30s-60s of operation. A caveat to be included with the measurements, is the pressure had not reached a steady state value before the thruster was shut off. In Test four, the lower pressure results from only the mass flow controllers being on and no power being applied to the thruster.

Table 5: Pressure readings during test

Test	Pressure (Torr)
1	1.63e-4
2	1.495e-4
3	1.328e-4
4	1.433e-5

A few potential reasons proposed to explain the rise in pressure are, the location of the thruster while in operation, degradation in the pumps, high energy ions making their way to the RGA, artificially inflating the pressure, and finally plume direct impingement of the cold plates. A combination of the first two are the most likely because a similar thruster was run at the same mass flow with no issues. Figure 49 below shows the thruster location in relation to the cold plates and the RGA port. As seen, the thruster is close to the RGA port, so it is very likely that high energy ions bouncing off of the walls could make their way to the measurement filament and artificially increase the pressure. After discussion with Liu, one mitigation strategy is to replace the graphite sheets on the chamber walls [29]. This was suggested because the old graphite sheets have started to degrade and fall apart. These sheets absorb the energy and in practice have lowered the

pressure seen in the chamber while running the thruster. Before this could be implemented Pump E completely failed and ended testing of the thruster.

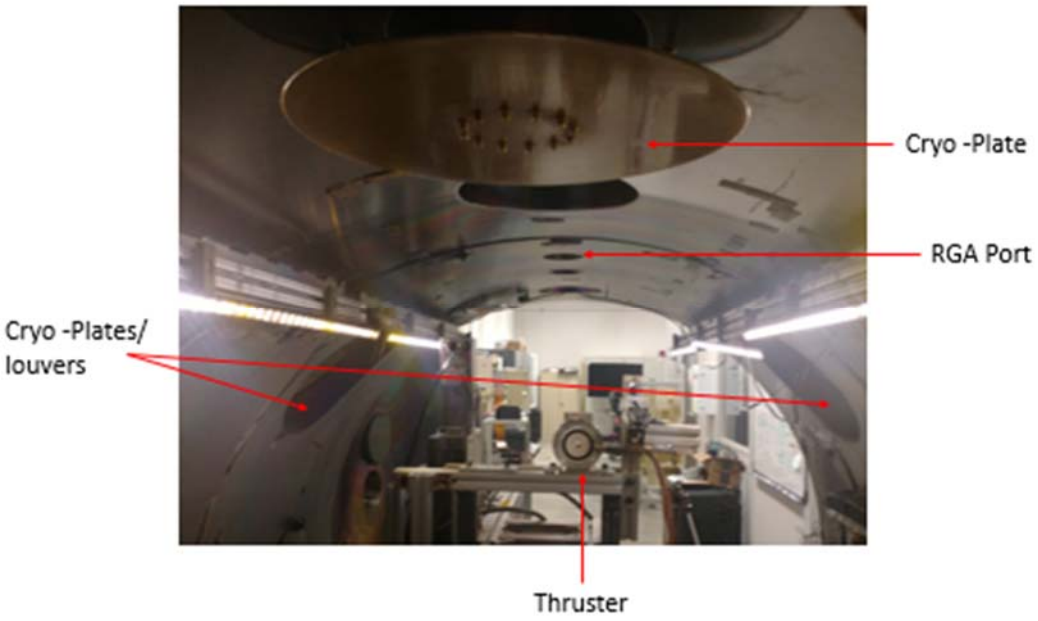

Figure 49: Chamber layout

Data collection

Due to issues with the chamber, data, other than optical emissions from a low resolution camera were not collected. From this point, it was determined that time would be better spent analyzing prior collected data, which is discussed in the next section.

Spoke intensity distribution analysis

Another area of interest for the present research is the distribution of the intensity of a spoke as it travels in the azimuthal direction. The reason this is an area of interest is because it could provide insight on how the ionization progress takes place. There are some limitations on the observations that can be made due to the data used for analysis. One is we have a limited understanding of what the optical emissions mean. Because the

images are panchromatic and only across the visible range we cannot directly observe the wavelengths of the emitted photons. Liu *et al.* was successful at correlating the spoke's angular velocity to some observed phenomena though [21]. Another limitation is based on the orientation of the high speed camera. The Images collected were of the entire plasma plume, not just at the exit of the thruster. This means that the resulting images are a combination of the optical emissions from the entire plasma plume as illustrated in the figure below.

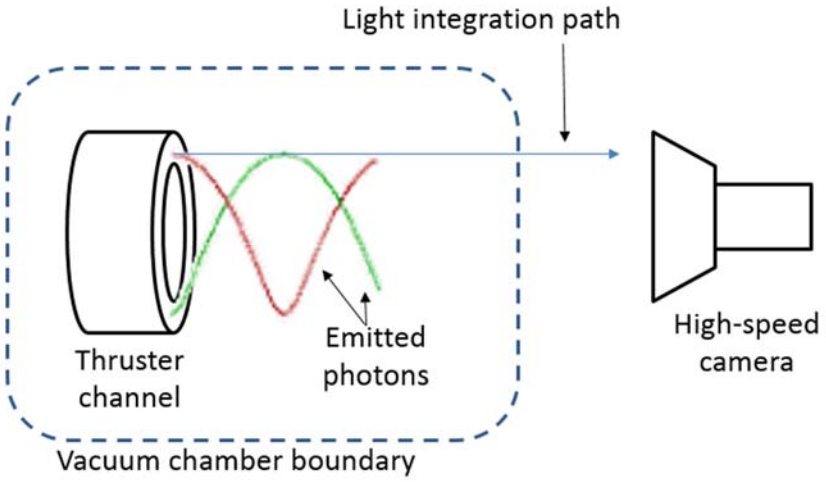

Figure 50: Light integration path

Due to the number of spokes in each image not all spokes were evaluated, on average 2-3 spokes per image were selected based on the criteria below when possible.

Criteria for spoke selection: first, when possible, the spoke shouldn't cross the -90 degree position. This is because the emissive probe masks this area on the thrusters, making the optical emission data from this location unusable. In some cases, spokes were chosen that passed through this point, so the data for the -90 degree position was not taken into account for analysis. Second, for the present analysis, the spoke had to be a single spoke; spokes that ran together were not considered. Lastly, if possible, spokes

were chosen such that they did not start in the same radial location. This allows for a more complete view of the of the thruster but, was not always satisfied because the spokes tended to show a preferential starting location in the lower half of the thruster, with no distinguishable spokes in the upper half of the thruster. This resulted in some plots having multiple spokes under study originating in the same area, but at different time steps.

An additional note on spokes, based on prior research, there is evidence that spokes can occur in the darker regions of the breathing mode based on plasma potential readings [5]. Due to the sensitivity of the high speed camera, the spokes were not distinguishable, and therefore not analyzed in the present research.

The first spoke presented for analysis is Spoke 1, from Unrolled Plot 3 and is highlighted in Figure 51 below. The optical emissions from spoke lasted 7μs from t = 78 μs to t = 84 μs. The highest intensity portion of the spoke traveled from 108 degree radial location to 154 degrees.

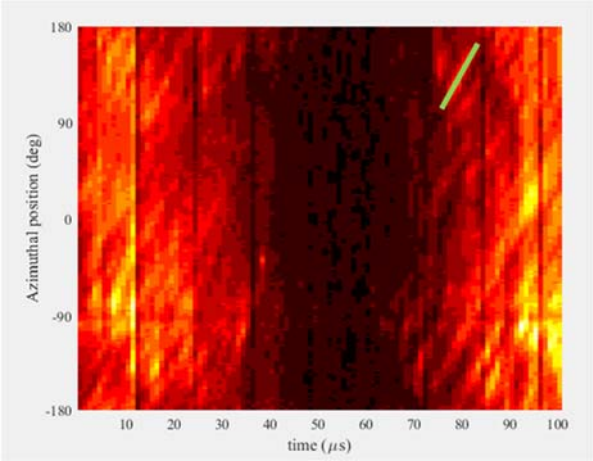

Figure 51: Unrolled Plot 3 Spoke 1

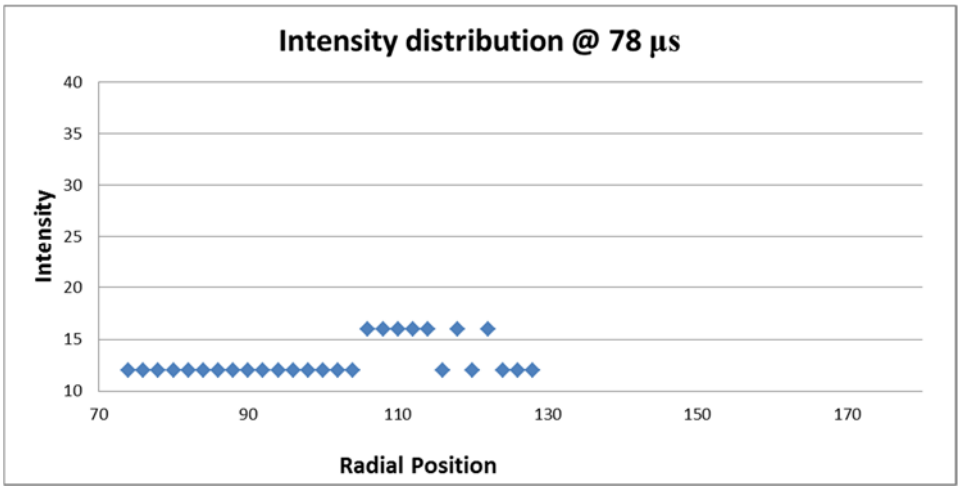
Intensity distribution @ 78 µs
Intensity
40
35
30
25
20
15
10
70
90
110
130
150
170
Radial Position

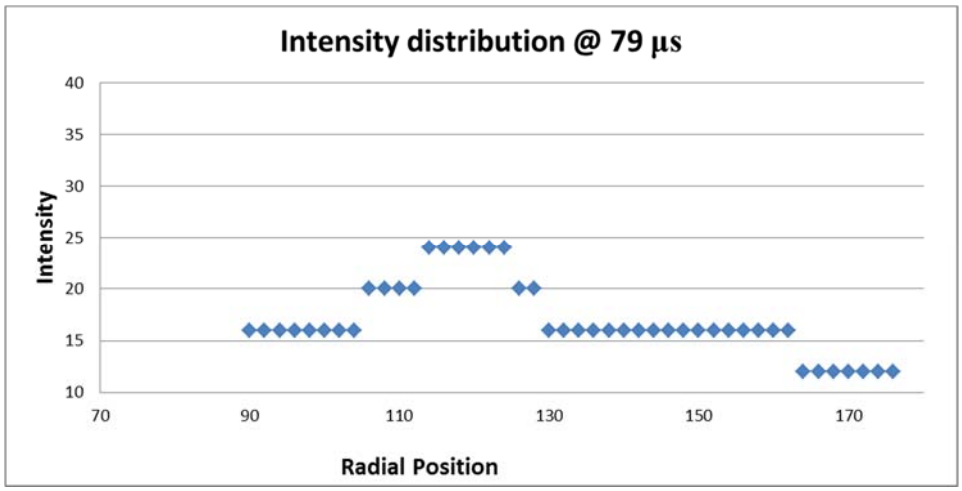
Intensity distribution @ 79 µs
Intensity
40
35
30
25
20
15
10
70
90
110
130
150
170
Radial Position

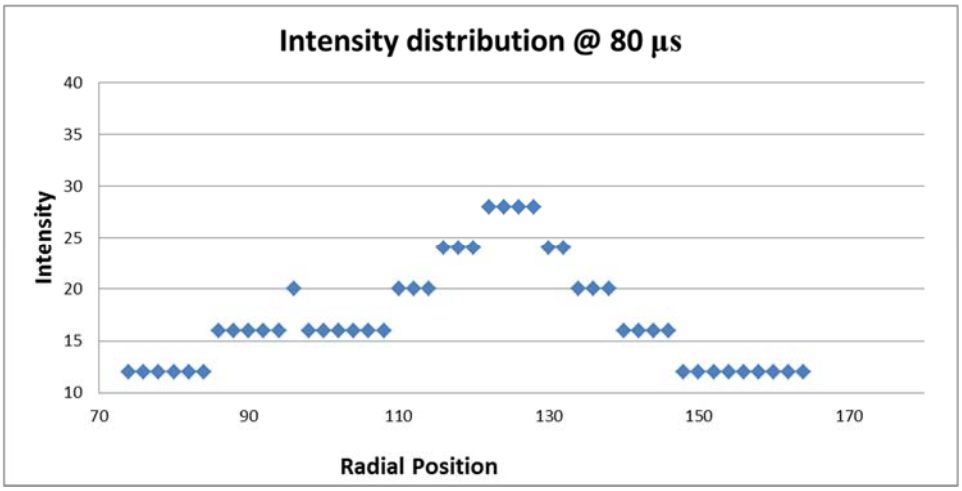
Intensity distribution @ 80 µs
Intensity
40
35
30
25
20
15
10
70
90
110
130
150
170
Radial Position

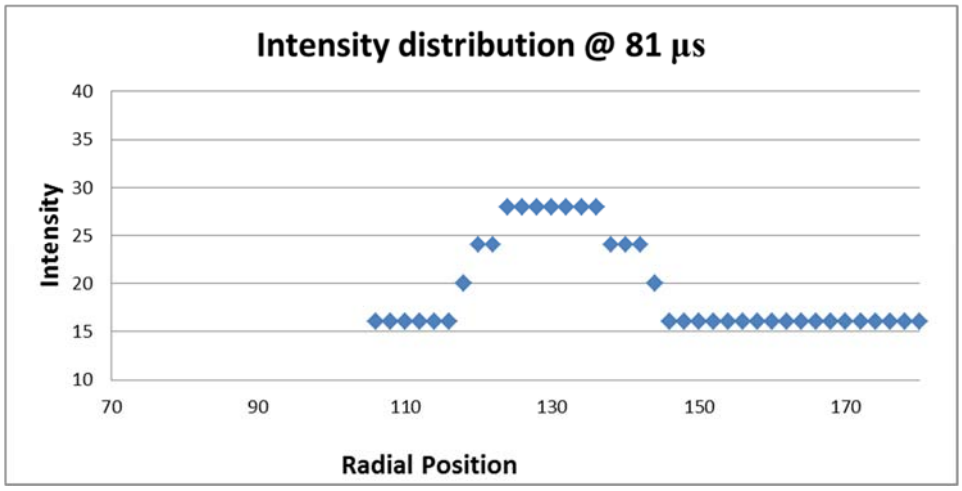
Intensity distribution @ 81 µs
Intensity
40
35
30
25
20
15
10
70
90
110
130
150
170
Radial Position

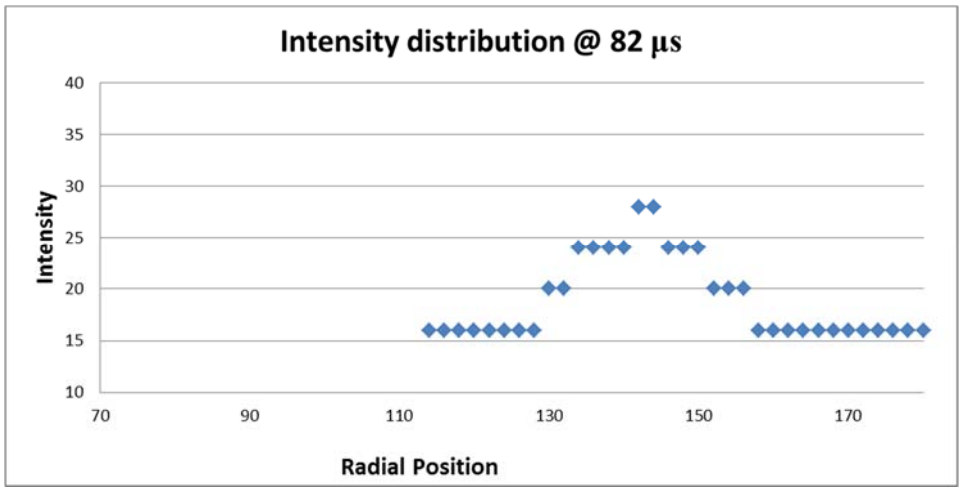
Intensity distribution @ 82 µs
Intensity
40
35
30
25
20
15
10
70
90
110
130
150
170
Radial Position

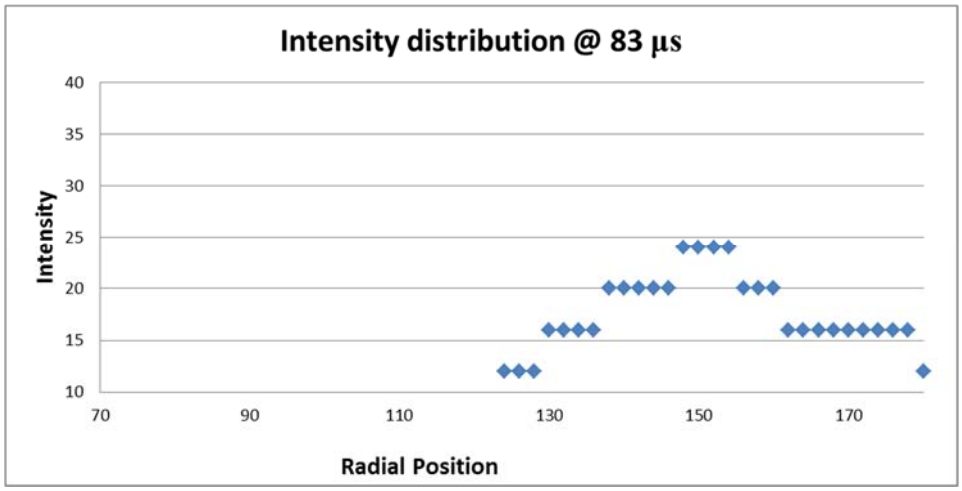
Intensity distribution @ 83 µs
Intensity
40
35
30
25
20
15
10
70
90
110
130
150
170
Radial Position

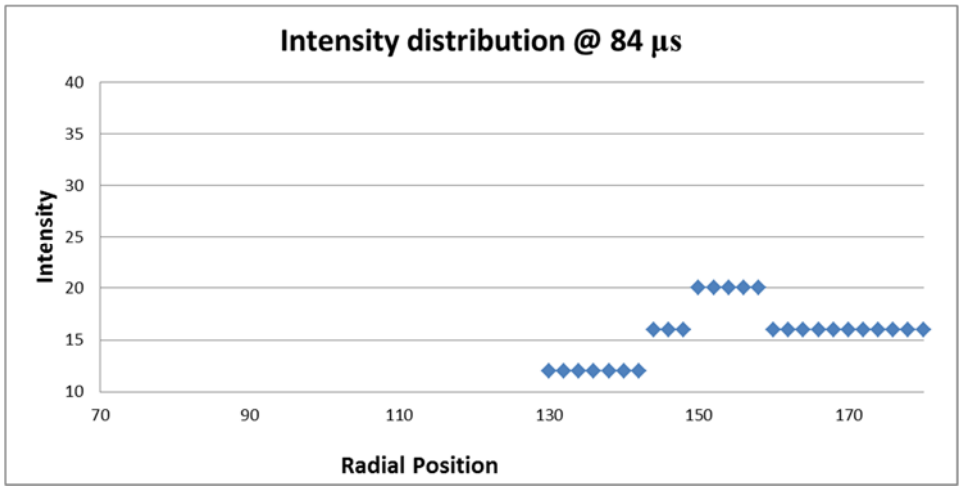

Figure 52: Spoke intensity propagation (Unrolled Plot 3, Spoke 1)

From these intensity graphs, we can calculate the angular velocity of the spoke. This is done by comparing the initial radial location of the high intensity location to its final location and then dividing by the elapsed time. In the presented case, the spoke travels at 109,706 radians per second. The spokes analyzed in this research range from 99000 radians per second to 133000 radians per second with a max error of 6500 radians per second based on potential location and timing error. This equates to a spoke velocity ranging from 3 km/s to 4 km/s which is slower than what was seen in experimentation on a 200 W Hall thruster by Liu and slower than what was seen in Janes and lowder's research [22] [14]. These velocities are however close to experimentation done on another 600 W Hall thruster [21]. All of the data used for analysis from the prior research, the spokes travel counter clockwise around the thruster in the direction of the $\vec{E} \times \vec{B}$ force which agrees with findings from prior research [5] [14] [21] [22].

Another aspect of interest is the distribution and resting point of the intensity profile. For the above spoke, the intensity drops off uniformly on both sides of the spoke at each time step. The final settling point is not always the same, for example, at t = 84 µs

the intensity on the right side of the peak is higher than the left. One potential explanation for this can be attributed to the integration path for the optical emissions as seen in Figure 50. As the spoke travels around the thruster face there will be a bias in the intensity data due to the orientation of the high speed camera. Figure 53, from Spoke 3 on Unrolled plot 2, shows another large difference between the right and left side of the plot. In this case it is because this spoke followed another spoke, and after the spoke under examination passed by, the intensity dropped back down to the baseline state of the breathing mode. An example of this in its entirety can be seen in Appendix A, Unrolled plot 7, Spoke 1.

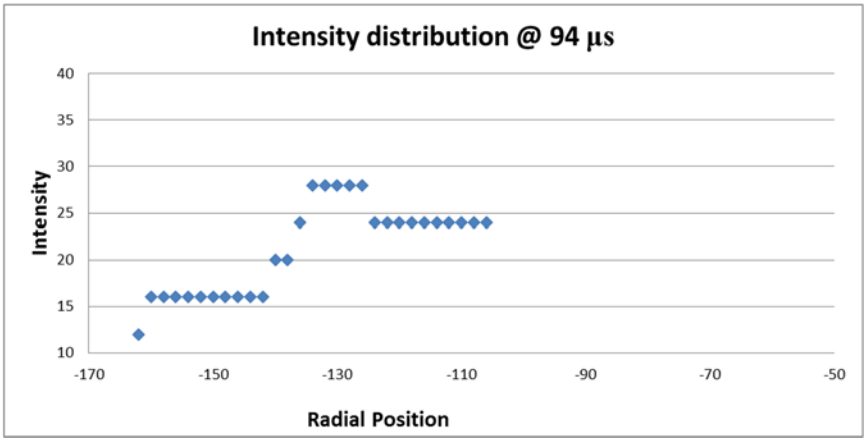

Figure 53: Intensity distribution (Unrolled plot 2, Spoke 3)

It is worth noting that the step size for the increase and decrease in intensities appears to be the same for a spoke at any particular time step. This suggest that the energy levels associated with the wave lengths of the optical emissions on each side of the spoke are similar, but since the images taken are panchromatic, we cannot determine if we are seeing excited neutrals, ions forming, or ions recombining from any single image.

An additional phenomenon that was noticed in prior research, is the apparent preferential spoke location in the thruster channel of 180 to 360 degrees. The thruster was examined for any surface anomalies that could contribute, but the surface wear looked uniform. The magnetic field strength was also measured, and appears similar to the PM Hall thruster with no distinguishing characteristics for the lower half. Another potential explanation relates to how the power and propellant are delivered to the anode, which can be seen in Figure 54 below. Due to internal resistance within the anode, the voltage closer to the anode power connection point would be incrementally higher than the voltage at the propellant feed line connection point. Using a multi-meter, the difference in resistance between the upper and lower portion of the anode to the power connection point was 0.1 Ohms, which happens to be the maximum resolution of the multi-meter in use, thus we can only say the resistance is higher than 0.05 Ohms. This difference will result in a slightly stronger E field in the upper part of the thruster, which would not affect performance significantly, but could drive a preference for spoke initiation. Analyzing the propellant feed, it can be seen that it is also a single delivery point. This will result in a pressure gradient favoring the propellant feed line side of the thruster.

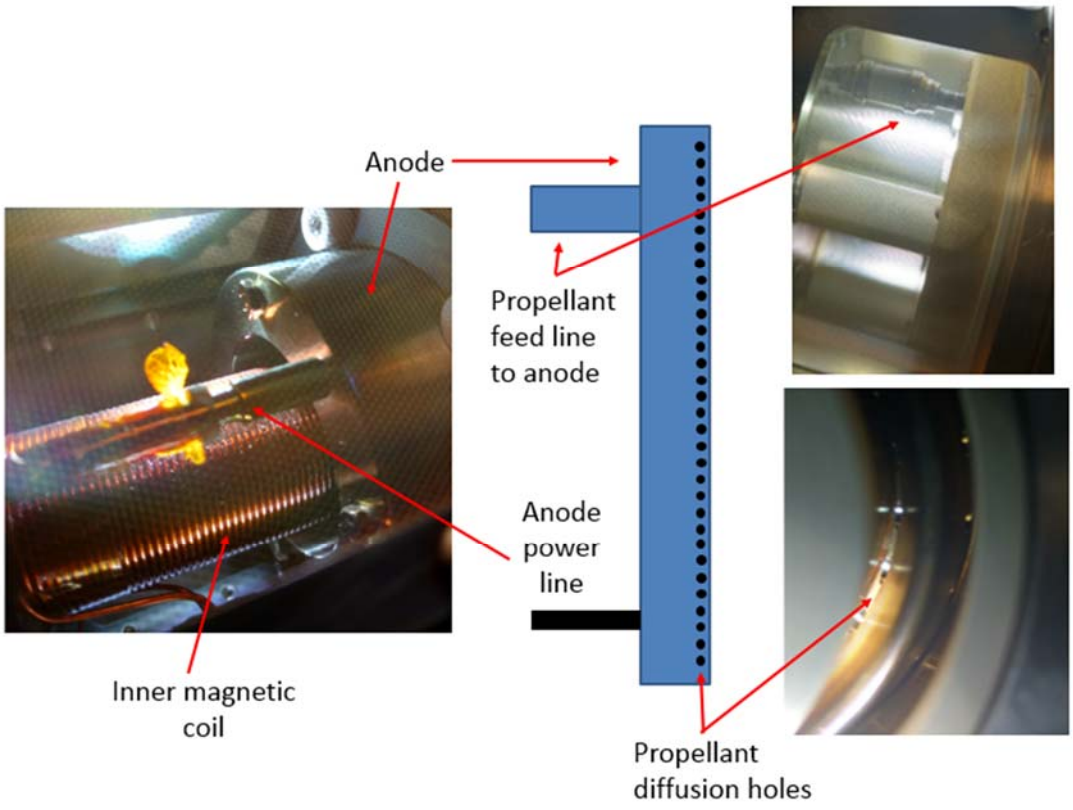

Figure 54: Anode cross section

If this is put this together, it can be seen how the slightly stronger E-field in the top of the thruster could capture higher energy electrons creating an electron wave which would then travel around the thruster face to the lower region where there could be a slightly higher density of excitable particles, thus ionizing more xenon atoms and releasing more photons increasing the observed optical emissions. In addition, the operating conditions used to highlight spoke mode for these tests called for a reduction in mass flow through the anode [5]. This could create a pressure gradient and anode mass flow gradient between the upper and lower portion of the anode further supporting the theory mentioned above. This can also be approached from another angle, if one looks at a

simple model showing Ions vs neutrals shown in Figure 55, created with the assumption of a constant mass flow, ionization rate, and no losses. From this, it can be seen that they rise and fall inversely to each other, and if we then couple this with an unequal distribution of propellant, a localized oscillation in the ionization process could occur.

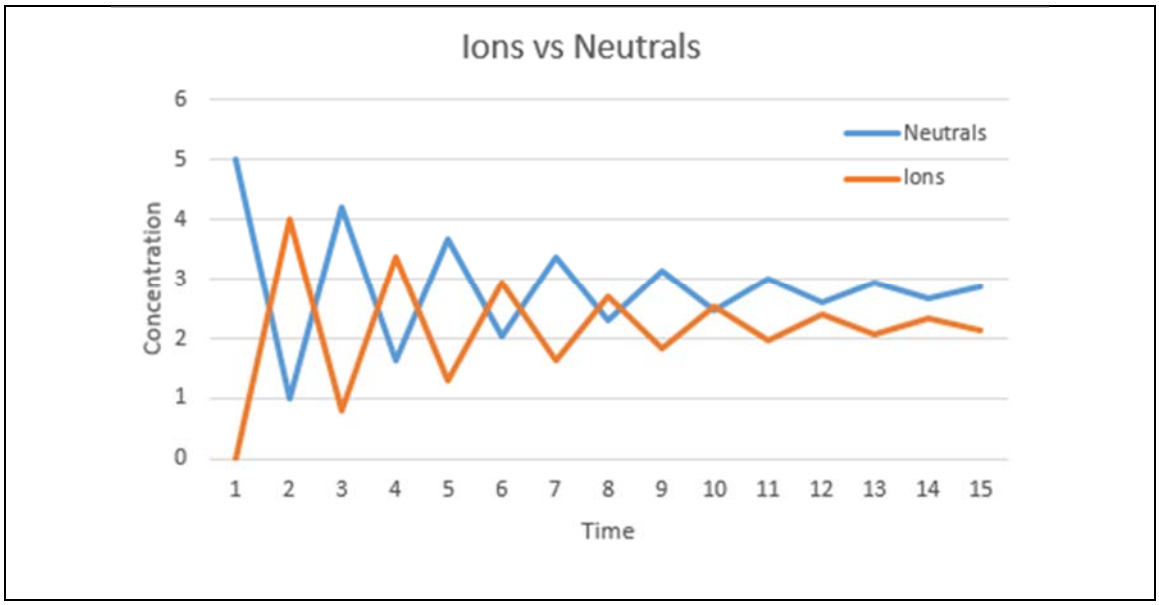

Figure 55: Ions vs. Neutrals

It is difficult to prove this from the information at hand, but if we look at the number of diffusion holes in the thruster and correlate that to a frequency, it could help isolate a contributing factor to spokes. More information on this can be found in the next section where the plots are analyzed in the frequency domain.

Frequency domain analysis: Breathing mode frequency analysis

The starting data set for the frequency domain analysis is shown in Figure 56 and is from unrolled plot 1 in the appendix A. The reason this data set was chosen is because it highlights the breathing mode for the Hall thruster while suppressing the spoke mode. This will provide a baseline for comparison to other graphs where spokes are the main feature under analysis.

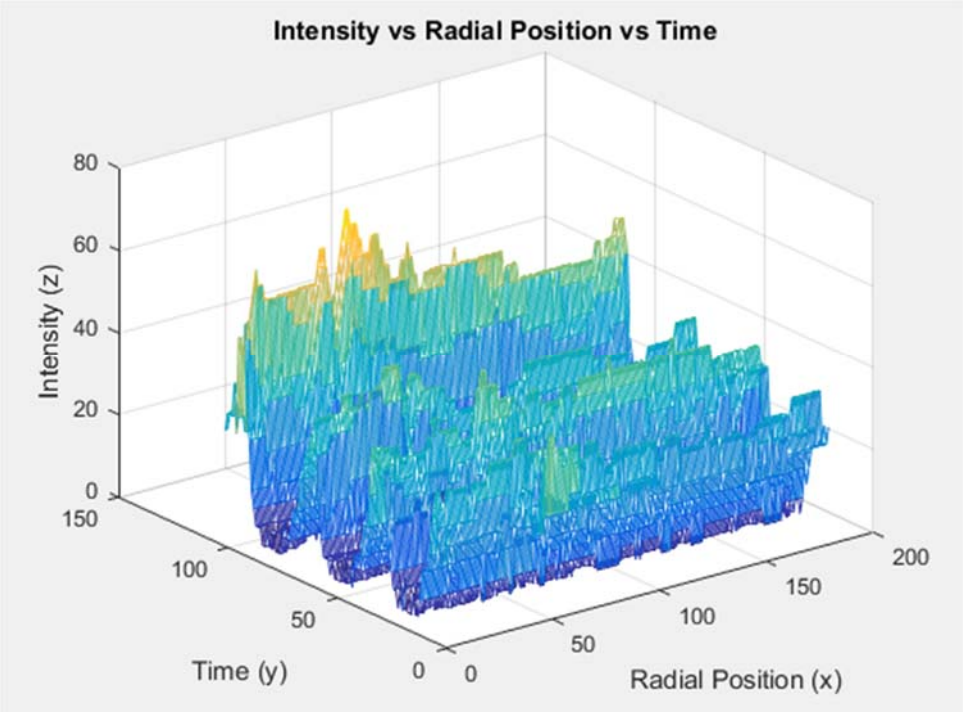

Figure 56: Baseline for frequency analysis (unrolled plot 1)

FFT Temporal frequency analysis, breathing mode

The first analysis was done on the transpose of the original matrix, such that the time is along the Y axis and radial position is along the X axis. Then a FFT was done along the columns to yield the graph below. The sample size that data was collected from was 100 samples in 100 μs. The max frequency we can then measure when a FFT is done with respect to position is 500 kHz with a resolution of 10 kHz. When a FFT is done with respect to time, 180 samples were taken over 2π radians, which gives a max frequency that can be measured of 14.32 cycles per radian.

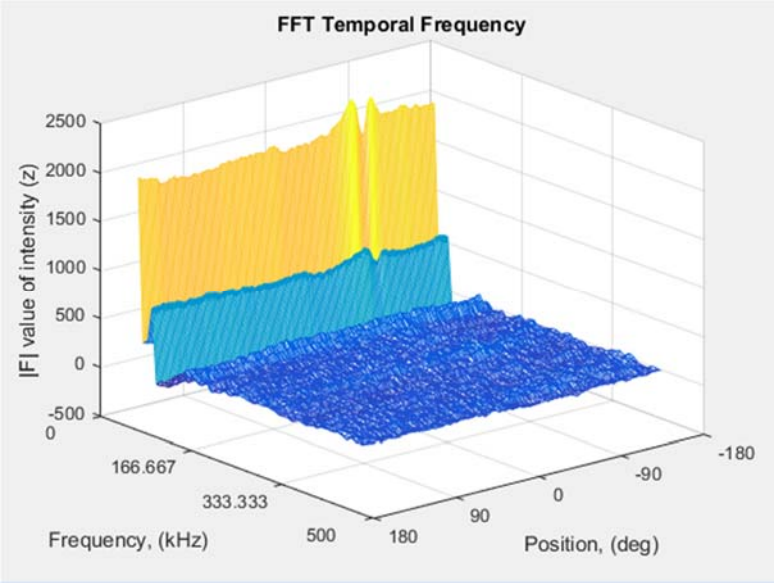

Figure 57: Baseline temporal frequency (unrolled plot 1)

From Figure 57 above, we can see that there is a general trend for the frequency components. As was seen in Figure 57, there is a very large DC component, which is followed by various other frequencies. One interesting feature in Figure 57, is the spike at -90 degrees. This spike is consistently seen in all of the temporal frequency charts and can be attributed to the emissive probe. Although the 3D plot allows for a good view of general trends, it is somewhat hard to look for specific trends; therefore the plots were again broken down to look at specific radial locations. The locations chosen are -180, -75, 0, and 90 degrees. These points were chosen to give a complete view of the thruster face. The significance in the number of points chosen stem from the ability to read the resulting graphs. When more than four data sets were overlaid on the same graph, the graphs began to look like they were made up of all noise. From the graph in Figure 58 below, we can see the initial frequencies follow a general trend that is shared across the thruster face. Because of this, we can conclude that over the time that measurements were

taken, the thruster variations were fairly uniform across the face of the thruster. A frequency of interest that was identified is the breathing mode. In the case of the figure below the breathing mode frequency was 40 kHz, and for that bin, all of the points of interest have a spike, which consequently is about the same magnitude as well.

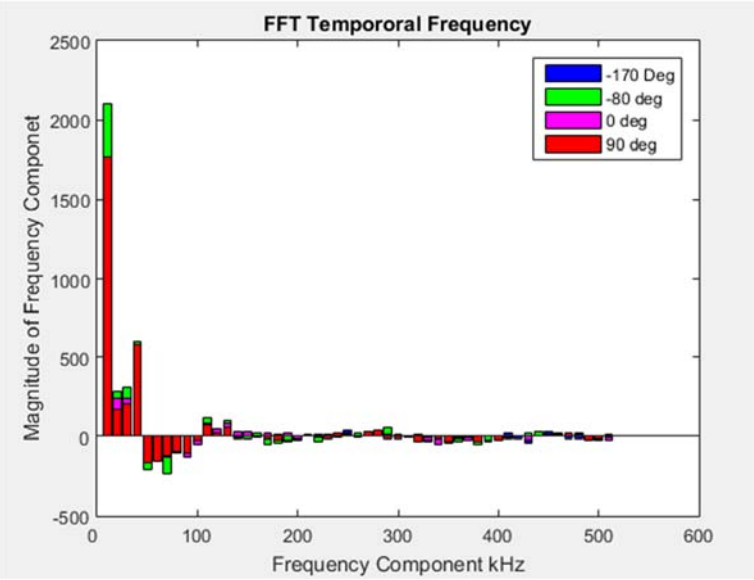

Figure 58: Selected temporal frequencies unrolled plot 1

FFT spatial frequency analysis, breathing mode

The above process was then repeated for each time step, yielding the 3D mesh graph below. One interesting component about this graph, is the spike in the DC component (flat constant level of intensity across all angles at an instant in time) of frequency associated with the maximums of the breathing mode. This highlights the fact that the overall intensity of the thruster channel is increasing and decreasing its optical emissions as the thruster breathes.

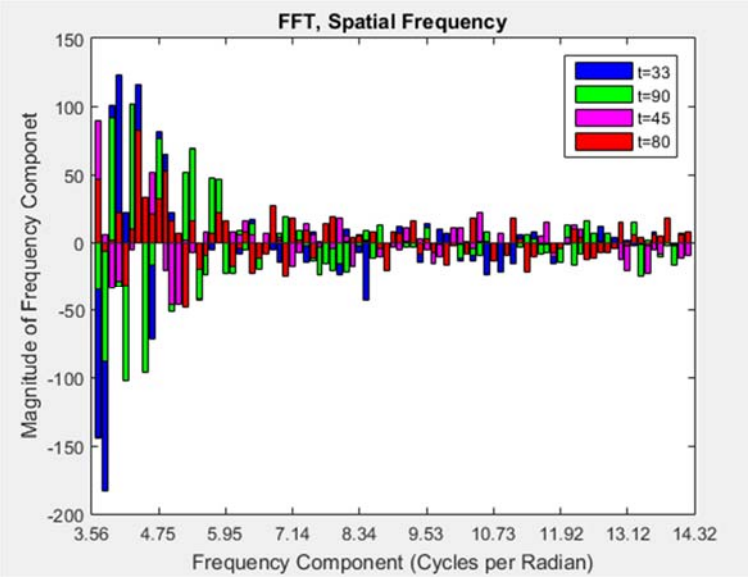

Figure 59: Breathing mode spatial frequency, (unrolled plot 1)

For Figure 58, the DC component of the frequency was not included in the graph. This is to better highlight any other frequencies that might be of interest. The time components selected represent areas of interest, primarily areas of high and low intensities for breathing mode. When the High and low intensities were plotted on top of each other, there does not seem to be any noticeable trends. When the scale of the plot is taken into account the resulting frequencies are an order of magnitude smaller than the DC component so there is the potential that there is noise mixed in with potential frequencies of interest.

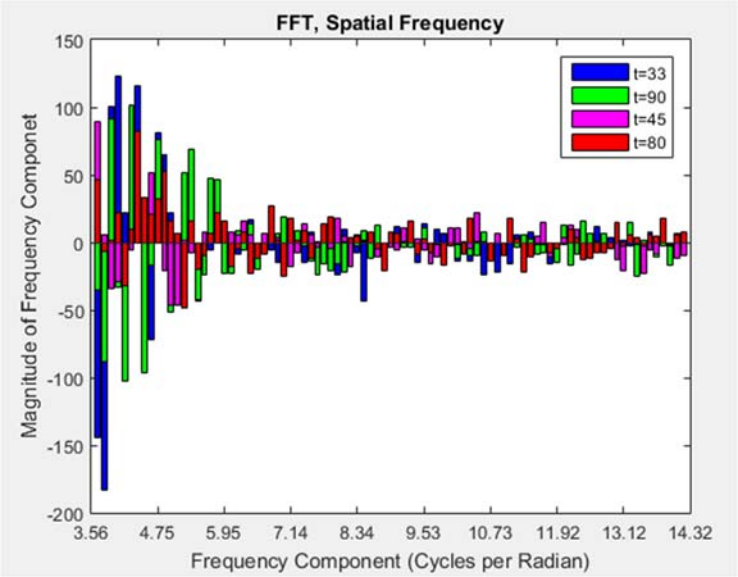

Figure 60: Selected breathing mode spatial frequency, Unrolled plot 1

FFT Temporal frequency analysis, spoke mode

The data set used for examples in the following section are from unrolled plot b which can be found in Appendix A. The graph in Figure 61 was created in the same way as Figure 57, and shows the temporal frequency across the thruster face. As before, the mesh plot shows global trends well but it is hard to identify any specific frequencies of interest.

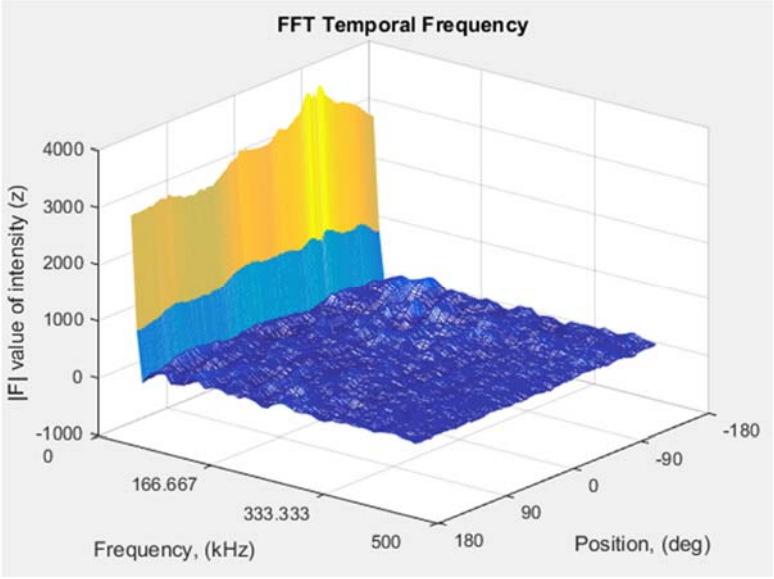

Figure 61: Spoke mode temporal frequency, Unrolled plot b

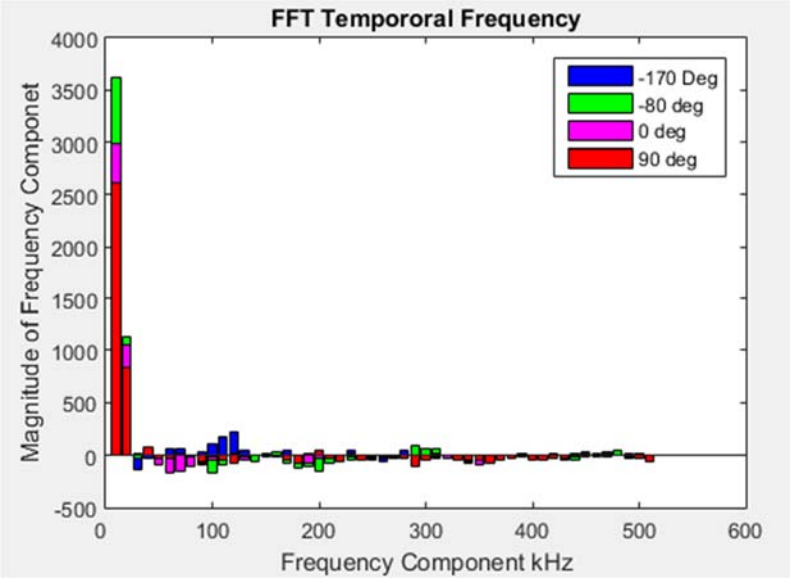

Figure 62: Selected spoke mode temporal frequencies, Unrolled plot b

To highlight particular areas of interest, Figure 62 was created. A point of interest with this figure is, even though the mode of operation selected was chosen to highlight spokes, the breathing mode is still prevalent. While this data was being collected, there were two

breathing mode cycles; thus the breathing mode frequency is 20kHz. When 20kHz is evaluated on the graph, the corresponding magnitude of the frequency component is high, and all of the frequencies have a component at that location. In addition, if the high intensity portions of the spokes that pass through the -180 Degree location on the thruster face are counted, the resulting frequency associated is 80 kHz, which also corresponds to a peak in the frequencies. If the same is done for the zero degree position, the resulting frequency is 50 kHz, which corresponds to a frequency minimum. This process was repeated for all the test cases listed in the appendix and the resulting frequencies often correlated with a frequency min or max. The cases where it did not work were when there were large areas of high intensity measurements caused by multiple spokes running together within the image. In these cases, the human can distinguish multiple spokes, but due to the resolution of the data, the computer saw less spokes. An example of this can be seen in Figure 63 below, which was taken from unrolled plot 4.

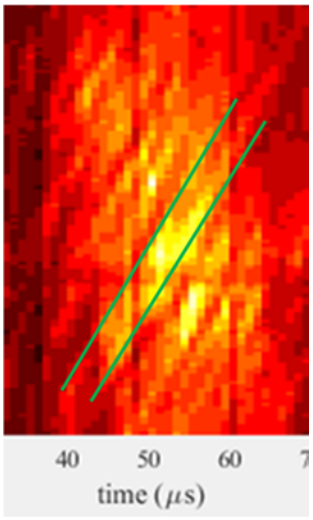

Figure 63: Example of spokes running together

This means that the resulting frequency that is calculated by hand for the number of spokes at that time will not be directly represented in the temporal frequency analysis figures. Another frequency that we would expect to see in the temporal FFT plots is the cyclotron frequency. Using the methodology described in chapter two, the cyclotron frequency was calculated to be 703 kHz. This frequency is above the frequencies that we can directly measure, so we then looked for the aliased frequency using the methodology described in chapter 3. The results of this calculation say that we should see a common frequency in the 300 kHz range. When the plots were evaluated, there was a common trend of the frequencies being grouped together in the 300 kHz range, as shown in the figure below.

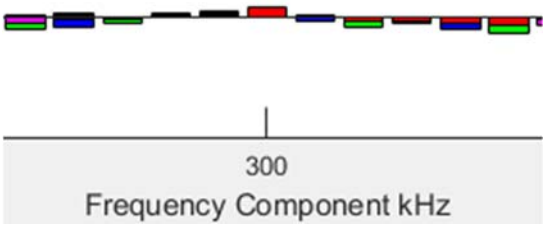

Figure 64: Aliasing of cyclotron frequency, Unrolled plot 2

Aliasing alone does not prove that what we are seeing is the cyclotron frequency, and what we are seeing is in the range of the noise of the frequency plot, but it is promising that a consistent trend was evident for both the breathing mode example and the spoke modes. In order to prove this theory, new testing equipment would need to be acquired that has the ability to measure frequencies in this range.

FFT Spatial frequency analysis, spoke mode

The graph in the figure below was created in the same manner as the previously described spatial frequency analysis graph. A feature that is immediately apparent is the breathing mode. This is seen as the two peaks along the time axis in Figure 65.

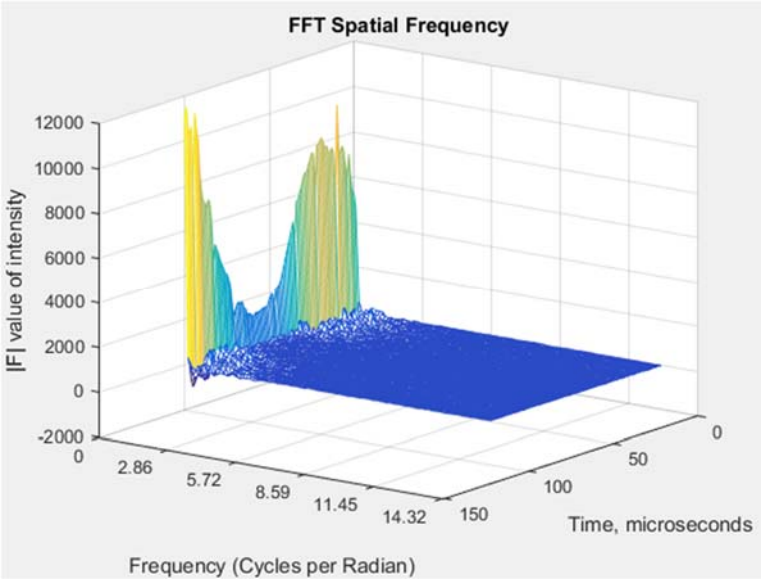

Figure 65: Spoke mode spatial frequency, unrolled plot b

The plot was then broken out at different time steps yielding Figure 66.

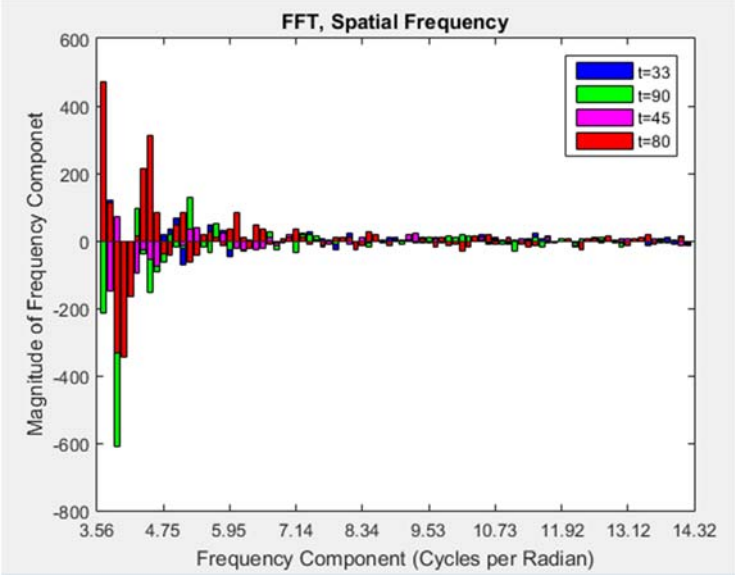

Figure 66: Selected spoke mode spatial frequencies, unrolled plot b

A feature that stands out in Figure 66 is the large set of negative frequencies at t= 90 μs. After examination of the unrolled plot b, it was found that there were 5 areas of high intensity. When that is converted to the frequency domain, it correlates to a frequency of 0.8 cycles per radian, which falls in that trough. This is true for t = 5μs where there are 4 areas of high intensity correlating to a frequency of 0.63 cycles per radian, but as mentioned earlier there is an error based on the resolution of the image. If a closer look at t=5μs is taken, it can be seen that there are instances where multiple spokes that run together, artificially lowering the frequency. An additional area of interest that was hinted at earlier in the chapter is a frequency associated with the xenon distribution. The thruster anode was examined, and on the core side of the anode, there were 25 diffusion holes. The outside of the anode could not be seen from the thruster face, so an assumption was made that there are 25 diffusion holes on the outer face of the anode as well. We can then look at the number of diffusion holes divided by 2π to get a frequency of 7.95 Hz. When we zoom in at this frequency, we see that in half of the cases there is a correlation and in the other half there is no correlation at all.

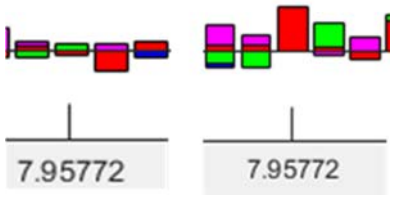

Figure 67: 7.95 cycles per radian, unrolled plot b and unrolled plot 4

From this data no, conclusions can be made for two reasons. First, the frequency in question is within the realm of noise for this plot. Second, there were only correlations in

half of the plots, so there is not enough evidence to prove a direct correlation. Because there some correlations, it would be worth a closer look for future research.

Chapter Conclusion

In this chapter, the trials associated with the successful operation of the thruster were discussed, as well as the results from further analysis of prior collected data. In the next, and final chapter, a summary of results will be given, as well as potential follow on research ideas.

V. Conclusions and Recommendations

Conclusions of Research

The original research goals for the present research were to get the thruster working, measure the changes in Hall current, plasma potential and visible emissions from the thruster, and analyze the resulting data. After significant work, the thruster was started and run, but due to issues with the chamber, no data was collected on the thruster. In lieu of analyzing data from the permanent magnet thruster, data collected prior to the present research was analyzed further. When the intensity profile was evaluated, it was noticed that the spokes shared a fairly similar normal distribution and the intensity levels varied in constant increments; but due to limitations in collection equipment, the ability to determine if ionization, excitation, or recombination was taking place was not able to be determined. A Fast Fourier Transform was then performed and frequencies associated spoke mode and breathing mode with were identified, however higher frequencies such as cyclotron frequency and Hall current frequency were not able to be directly identified.

Significance of Research

One exciting aspect of this research is the successful use of a permanent magnet in the Hall thruster. While this does not represent a huge power savings, it does reduce the complexity and weight of the thruster by eliminating the power supplies and control mechanisms associated with the magnets. As seen in the present research, the permanent magnet does restrict the propellant that can be used in the thruster because the magnetic field cannot be adjusted. This limitation would be of little impact in operational use, because there will only be one type of propellant for the Hall thruster on the space

vehicle. Due to lack of testing, there are some questions about the life of the magnets and how they change over many heat cycles associated with starting and stopping, thus for future testing, when the thruster can be run for extended periods of time, careful evaluation of the magnetic field is recommended.

Another aspect of interest for this research is the evaluation done on the spokes and breathing modes themselves. The findings again confirmed prior statements concerning breathing mode and spoke mode as well as providing a basis for potential relationship between Hall thruster construction and anomaly preferences.

Recommendations for Future Research

Since this research did not result in all of the desired research objectives being met, it is suggested this thesis is attempted again. There were several significant issues which arose during the testing process that have been addressed and worked through. This will allow for data collection to be started much easier. There are many different areas that still need to be evaluated with this permanent magnet Hall thruster. The first and most obvious would be to collect data on the thruster while it is in breathing mode and spoke mode, and compare to the electric magnet thruster. Additionally, one could build an apparatus to mount the cathode in various locations around the thruster to see if there is any correlation between cathode location and preferential spoke location. Another area to pursue would be higher frequency analysis of the thrusters; this would require new equipment but would provide insight on higher frequency phenomenon. An additional avenue to pursue would be to prove or disprove the theory that spokes start in an area with a higher $\vec{E}$ field. Further analysis would need to be done on the electric field of the Hall thruster, but once this was completed the theory could be tested by mounting

multiple emissive probes around the thruster face to capture plasma potentials as spokes pass.

Summary

The Busek 600 W permanent magnet thruster tested in this research was successfully started and run a total of 9 times in the duration of testing. Further testing was not able to be completed due to issues with the chamber, however the testing infrastructure created will allow the experiment to be continued easily. The use of permanent magnets decreases over all power requirements and make the thruster make an intriguing option for long-duration, low thrust satellite operations. This thruster design shows promise for future field use but will require more testing to evaluate anomalous diffusion modes and life span estimations.

Appendix A: Spoke velocities

Unrolled plot 2 spoke 3

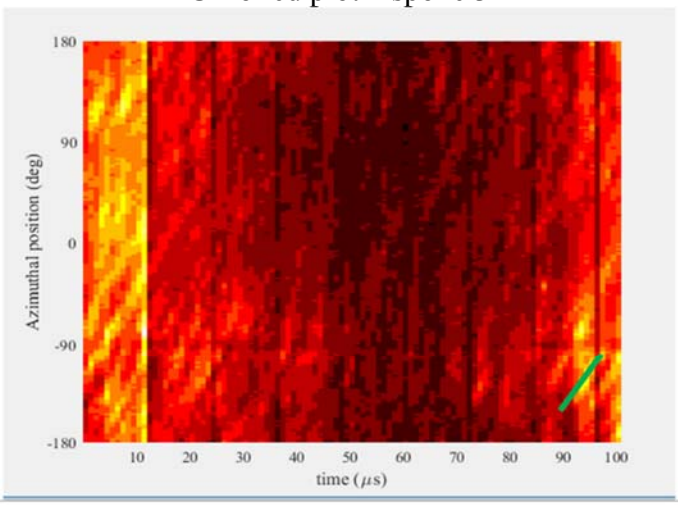

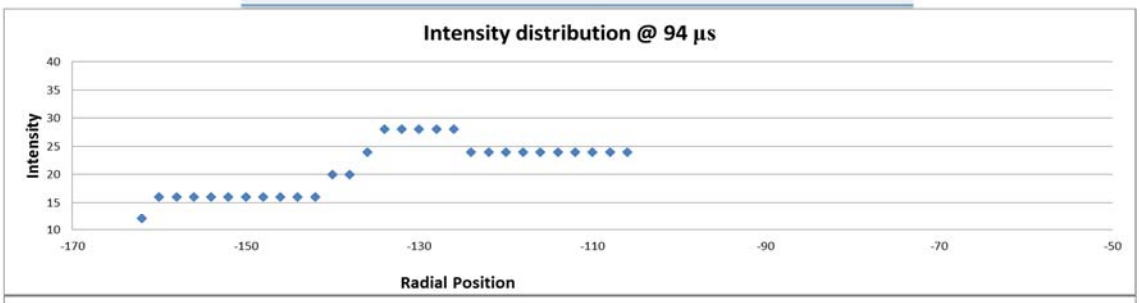

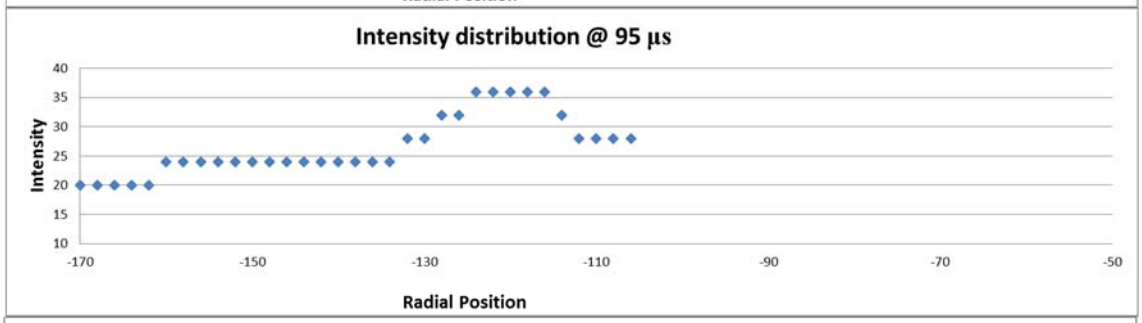

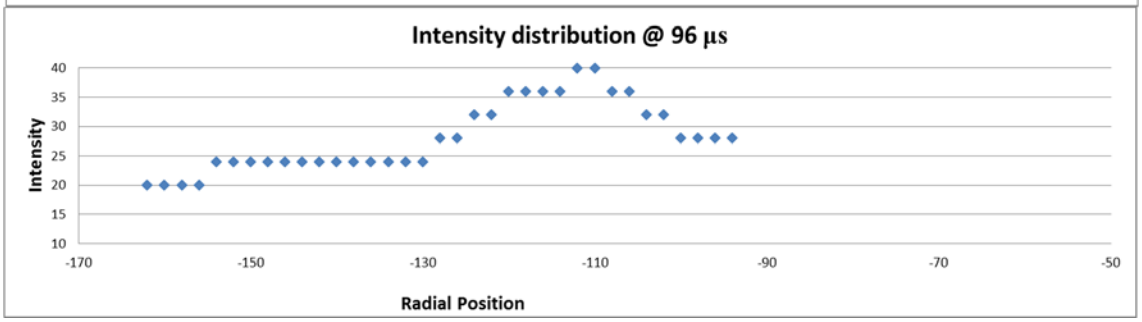

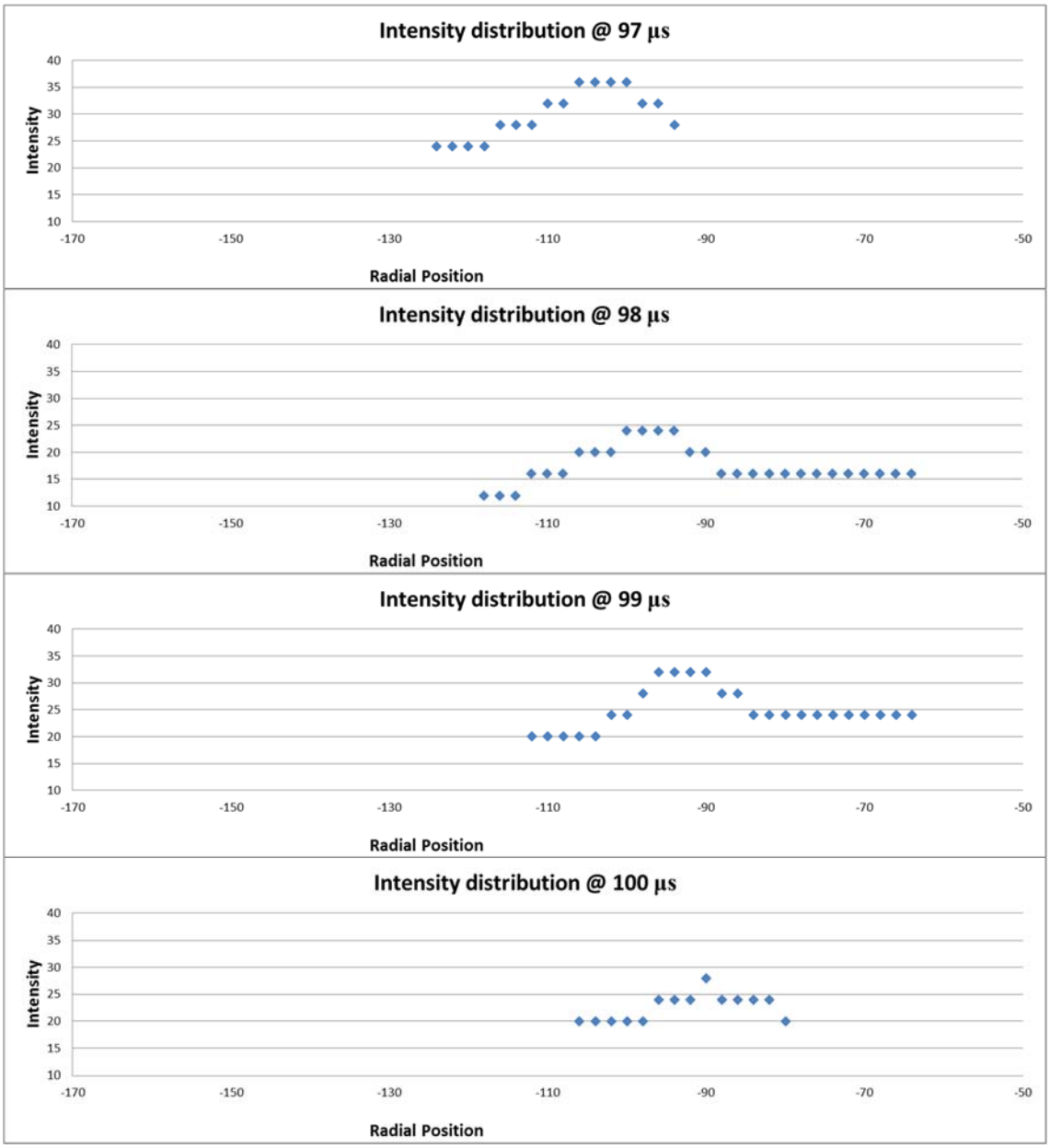
Intensity distribution @ 97 µs
Intensity
40
35
30
25
20
15
10
-170
-150
-130
-110
-90
-70
-50
Radial Position
Intensity distribution @ 98 µs
Intensity
40
35
30
25
20
15
10
-170
-150
-130
-110
-90
-70
-50
Radial Position
Intensity distribution @ 99 µs
Intensity
40
35
30
25
20
15
10
-170
-150
-130
-110
-90
-70
-50
Radial Position
Intensity distribution @ 100 µs
Intensity
40
35
30
25
20
15
10
-170
-150
-130
-110
-90
-70
-50
Radial Position

Unrolled plot 2 spoke 2

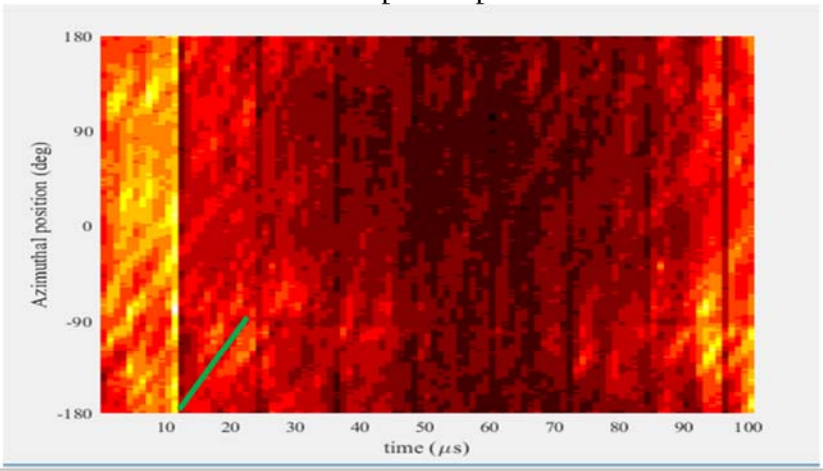

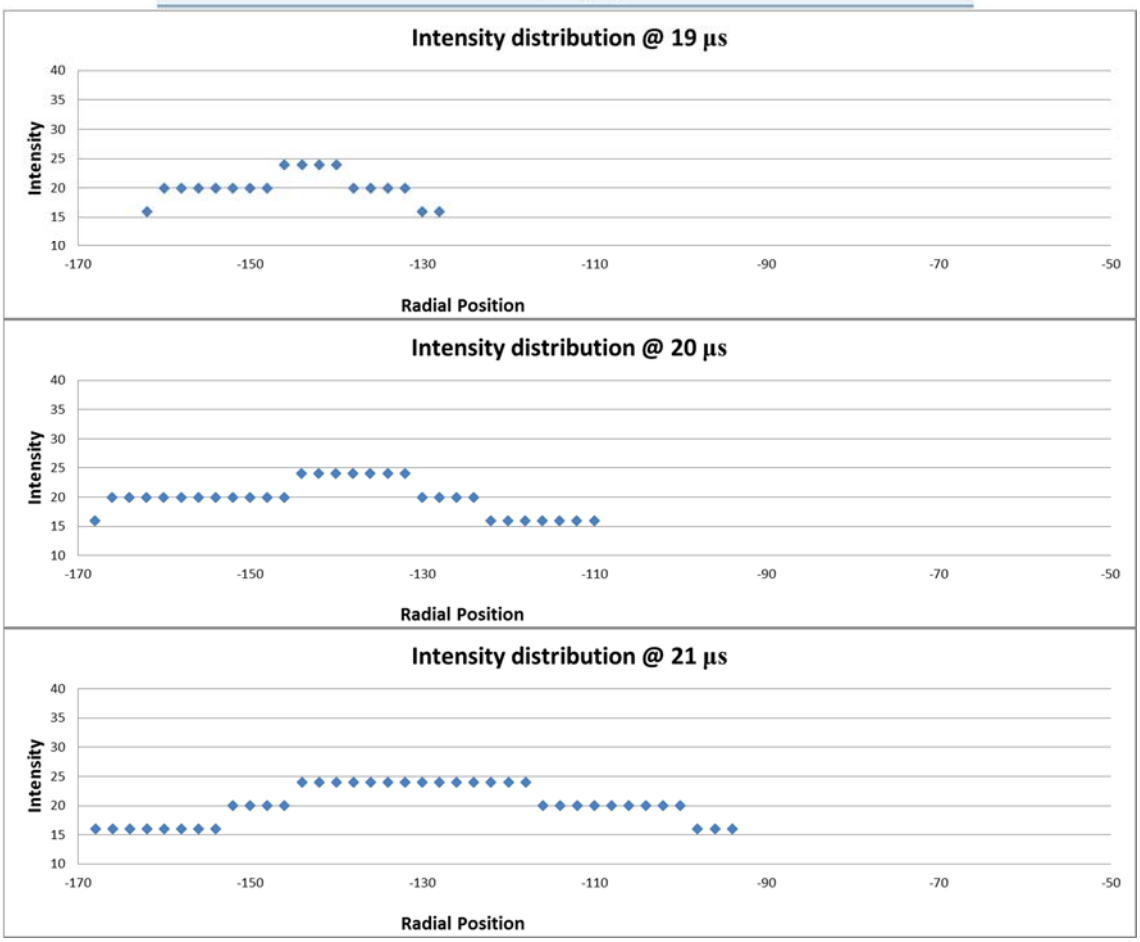

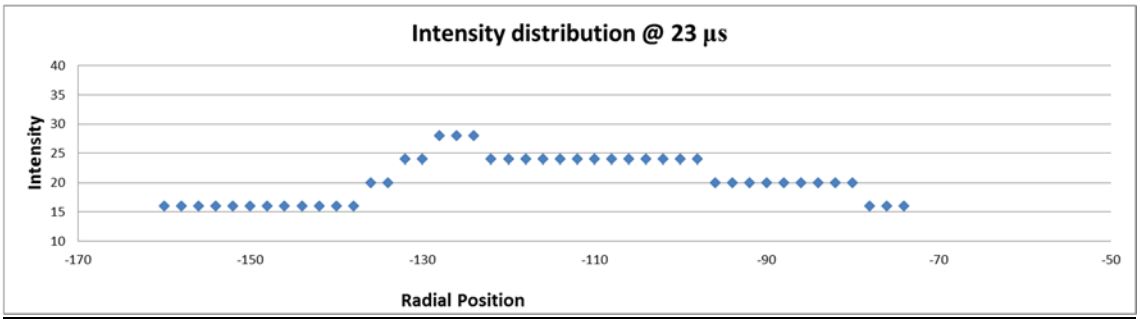
Intensity distribution @ 23 µs
Intensity
40
35
30
25
20
15
10
-170
-150
-130
-110
-90
-70
-50
Radial Position

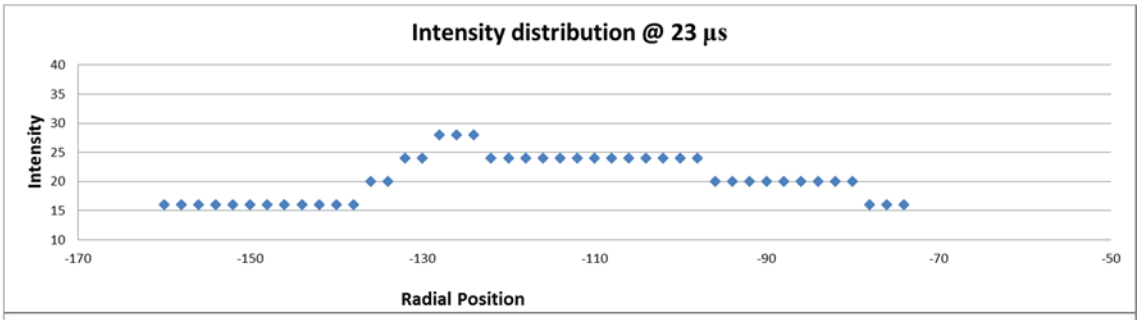
Intensity distribution @ 23 µs
Intensity
40
35
30
25
20
15
10
-170
-150
-130
-110
-90
-70
-50
Radial Position

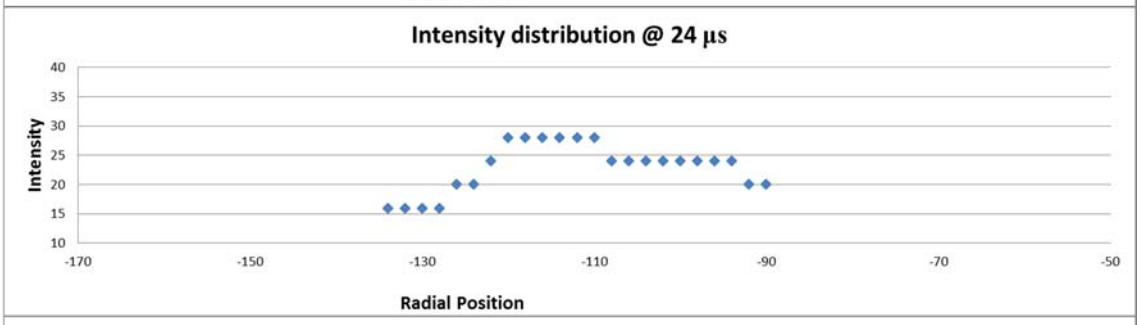
Intensity distribution @ 24 µs
Intensity
40
35
30
25
20
15
10
-170
-150
-130
-110
-90
-70
-50
Radial Position

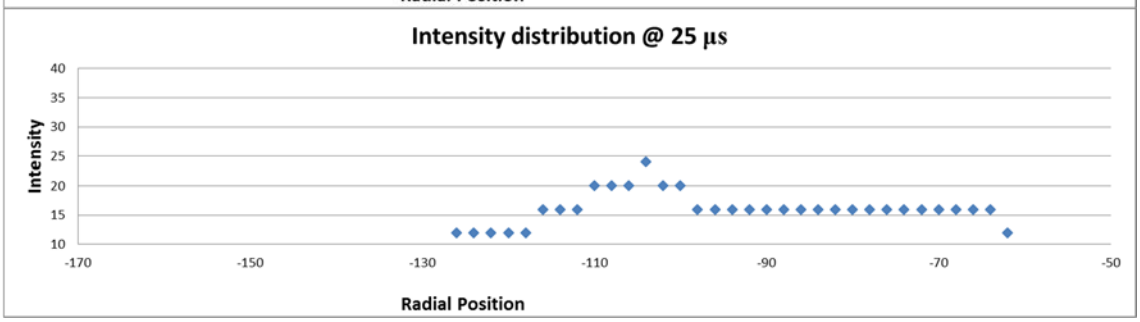
Intensity distribution @ 25 µs
Intensity
40
35
30
25
20
15
10
-170
-150
-130
-110
-90
-70
-50
Radial Position

Unrolled plot 2 spoke 1

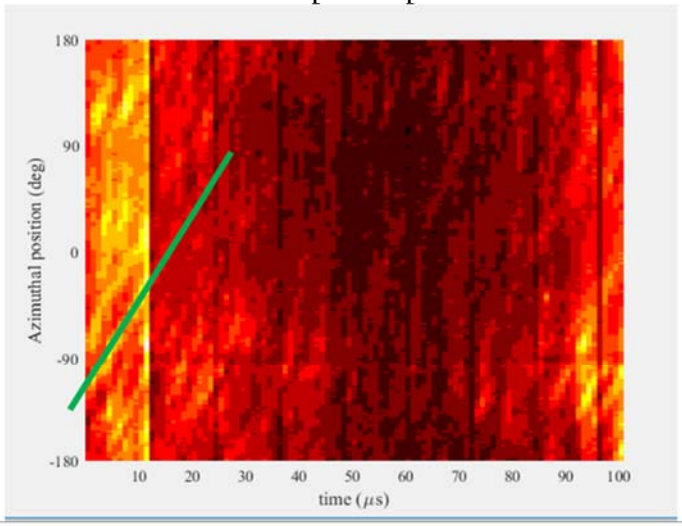

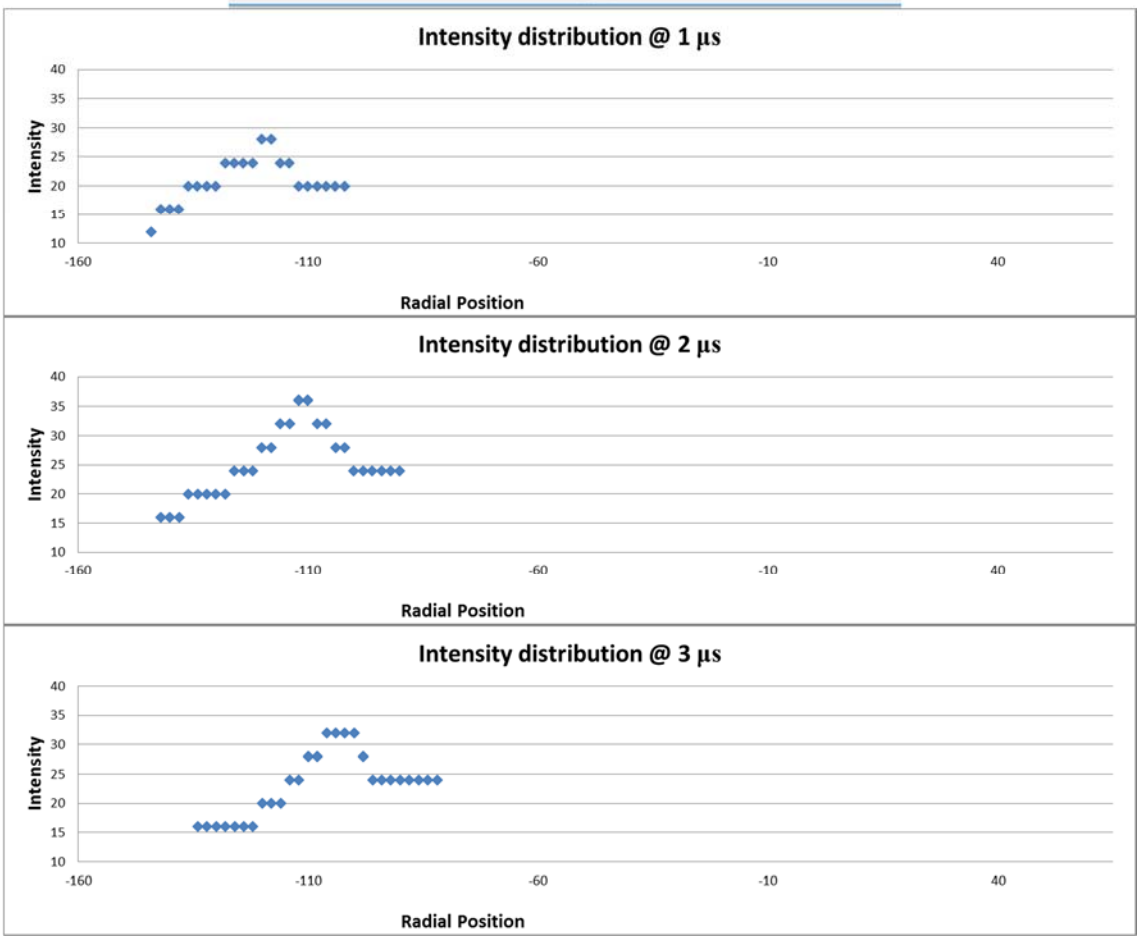

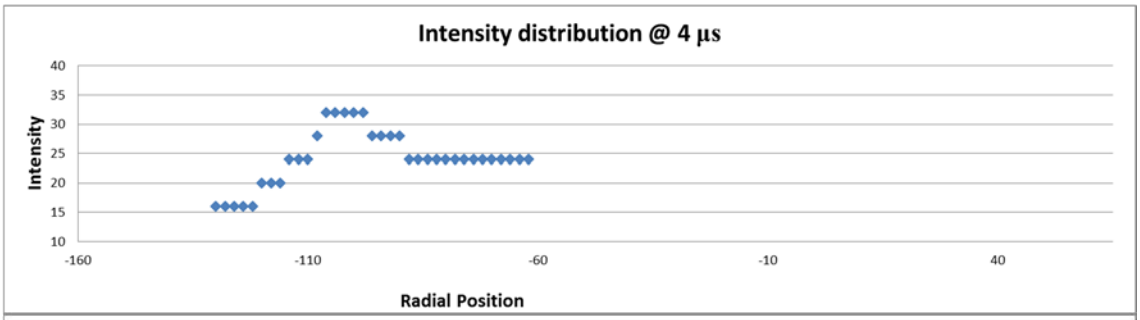
Intensity distribution @ 4 µs
Intensity
40
35
30
25
20
15
10
-160
-110
-60
-10
40
Radial Position

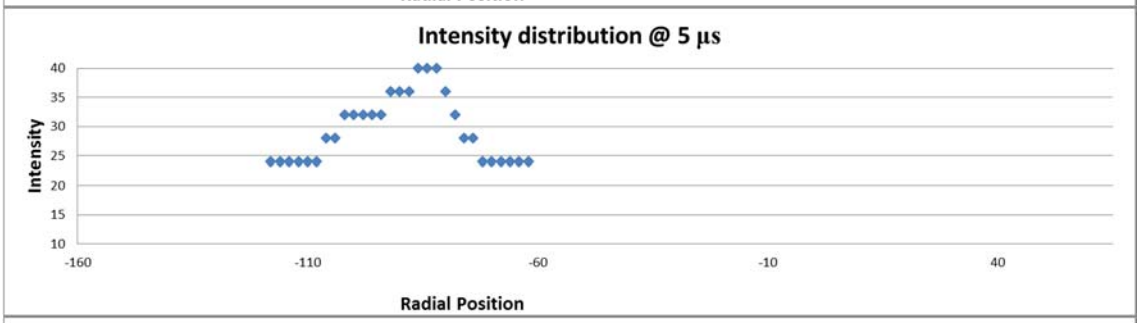
Intensity distribution @ 5 µs
Intensity
40
35
30
25
20
15
10
-160
-110
-60
-10
40
Radial Position

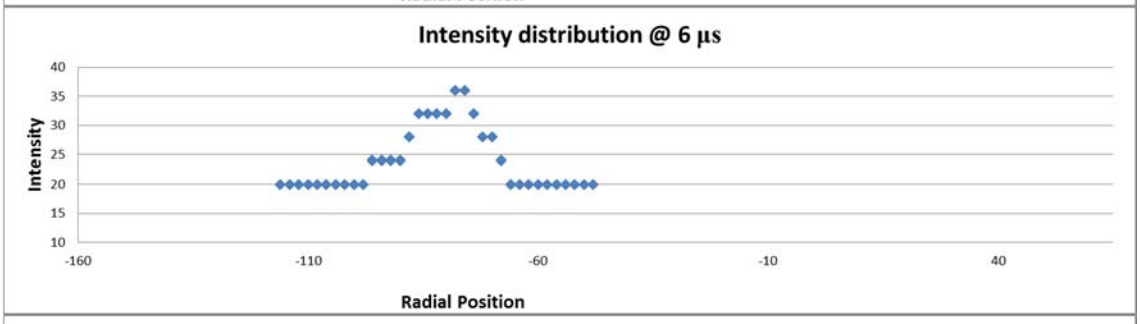
Intensity distribution @ 6 µs
Intensity
40
35
30
25
20
15
10
-160
-110
-60
-10
40
Radial Position

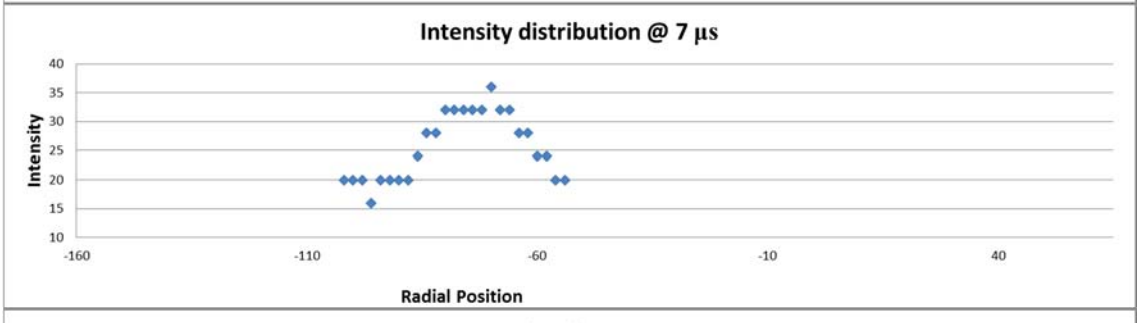
Intensity distribution @ 7 µs
Intensity
40
35
30
25
20
15
10
-160
-110
-60
-10
40
Radial Position

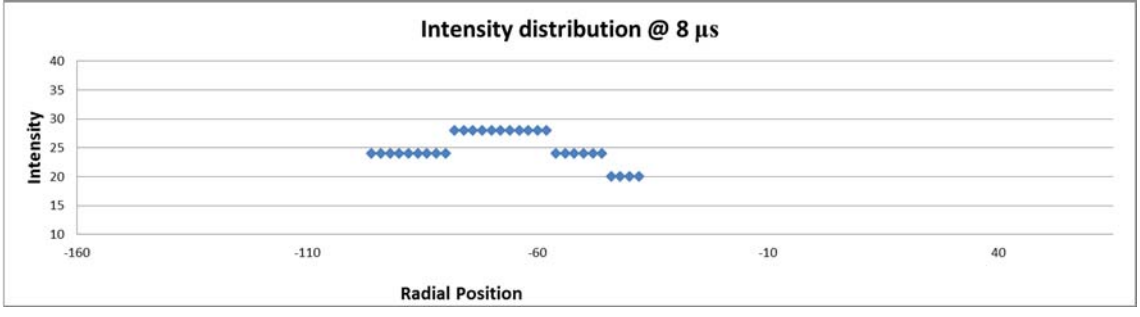
Intensity distribution @ 8 µs
Intensity
40
35
30
25
20
15
10
-160
-110
-60
-10
40
Radial Position

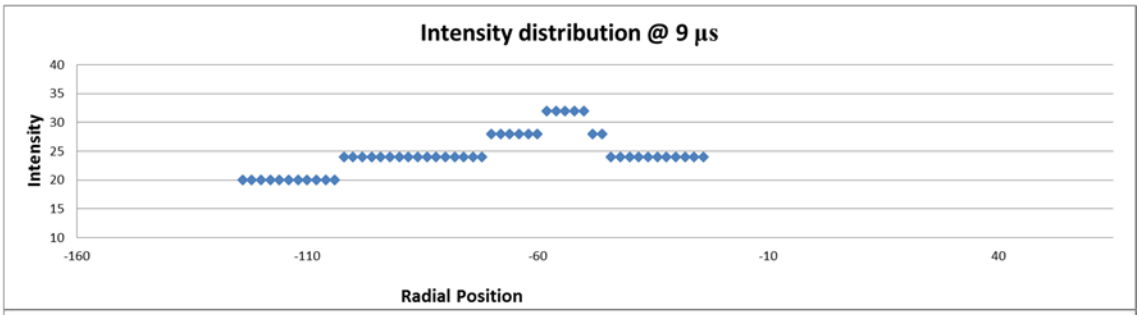
Intensity distribution @ 9 µs
Intensity
40
35
30
25
20
15
10
-160
-110
-60
-10
40
Radial Position

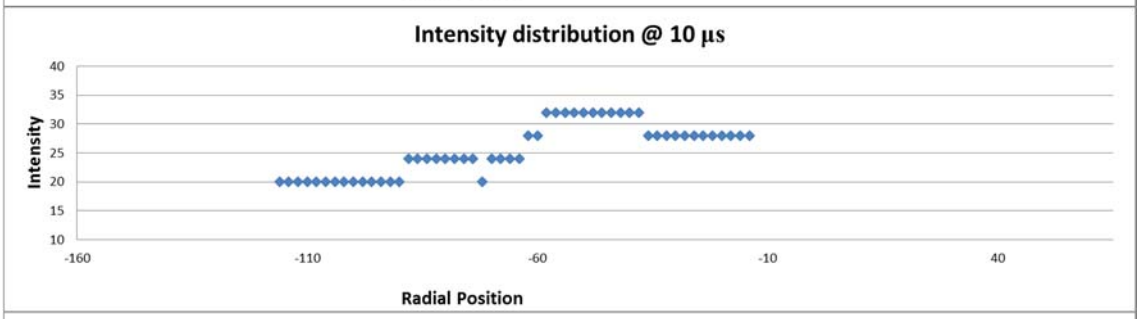
Intensity distribution @ 10 µs
Intensity
40
35
30
25
20
15
10
-160
-110
-60
-10
40
Radial Position

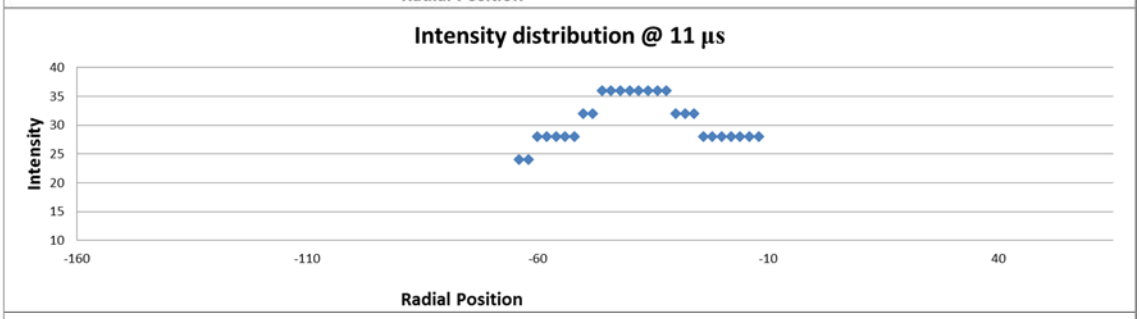
Intensity distribution @ 11 µs
Intensity
40
35
30
25
20
15
10
-160
-110
-60
-10
40
Radial Position

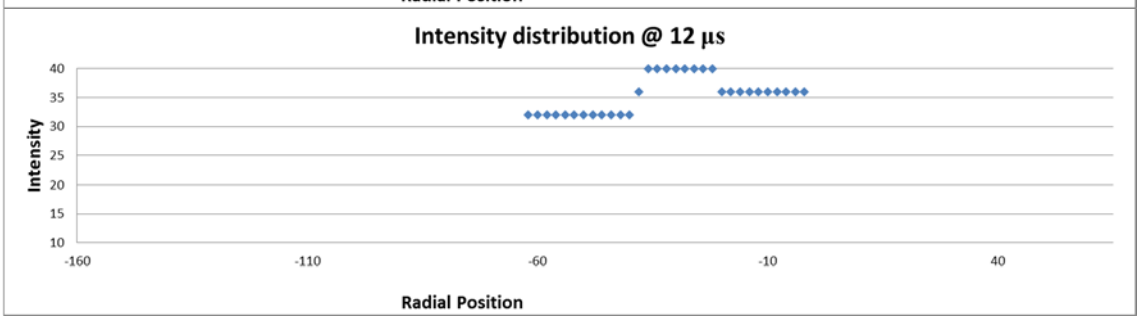
Intensity distribution @ 12 µs
Intensity
40
35
30
25
20
15
10
-160
-110
-60
-10
40
Radial Position

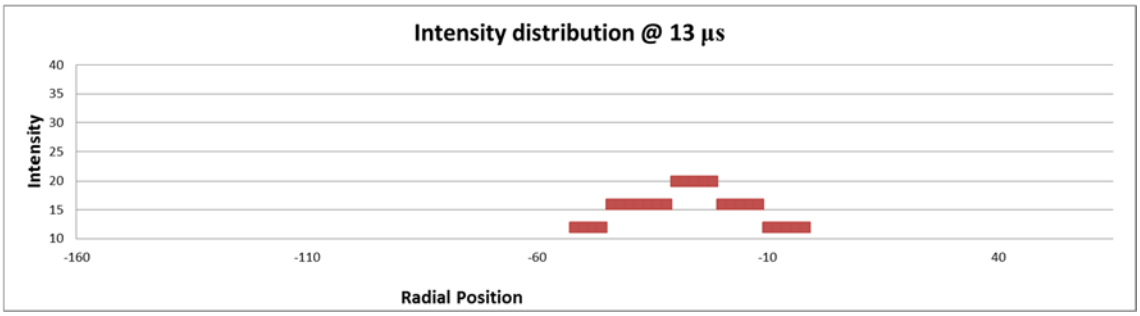
Intensity distribution @ 13 µs
Intensity
40
35
30
25
20
15
10
-160
-110
-60
-10
40
Radial Position

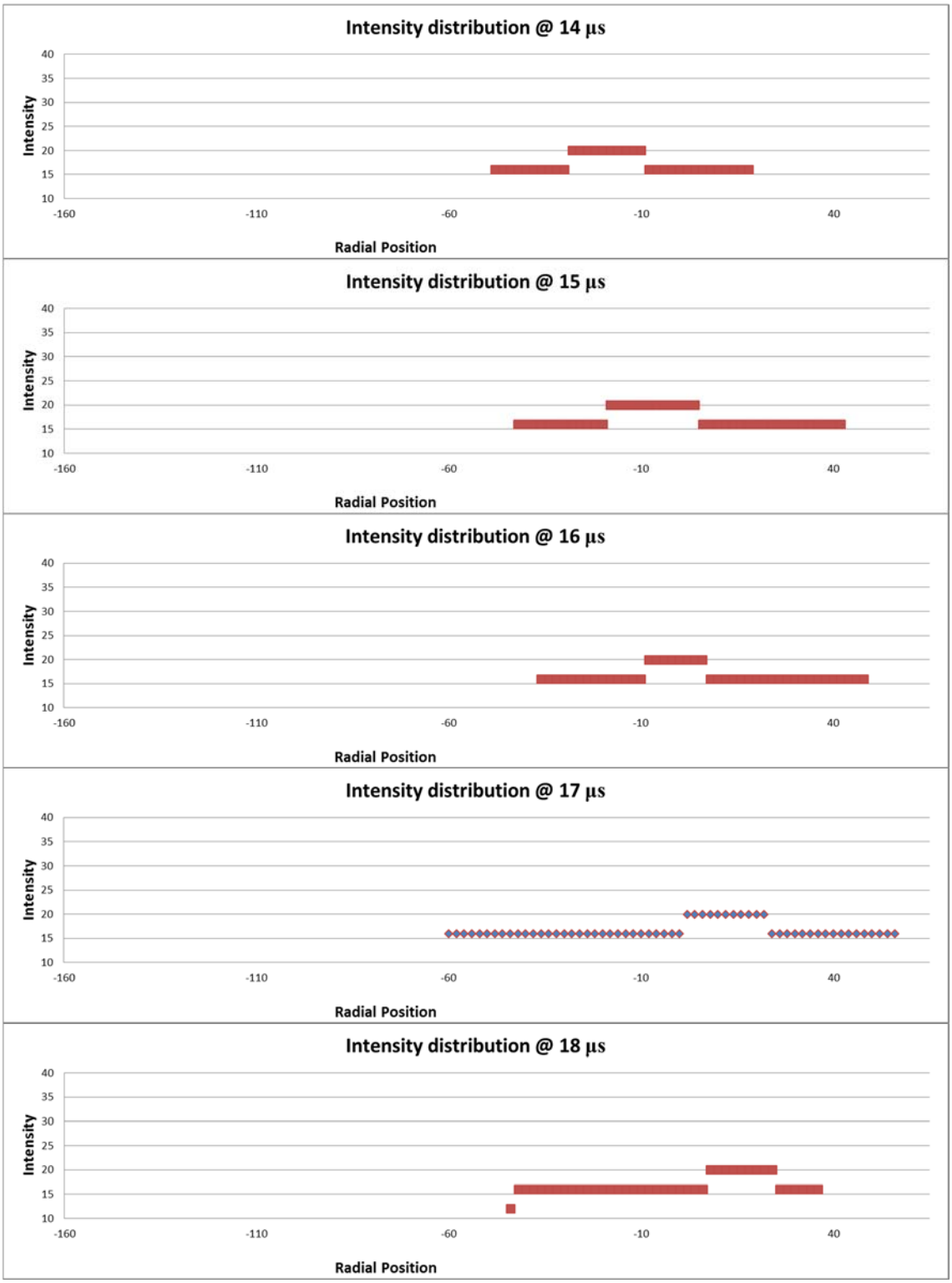
Intensity distribution @ 14 µs
Intensity
40
35
30
25
20
15
10
-160
-110
-60
-10
40
Radial Position
Intensity distribution @ 15 µs
Intensity
40
35
30
25
20
15
10
-160
-110
-60
-10
40
Radial Position
Intensity distribution @ 16 µs
Intensity
40
35
30
25
20
15
10
-160
-110
-60
-10
40
Radial Position
Intensity distribution @ 17 µs
Intensity
40
35
30
25
20
15
10
-160
-110
-60
-10
40
Radial Position
Intensity distribution @ 18 µs
Intensity
40
35
30
25
20
15
10
-160
-110
-60
-10
40
Radial Position

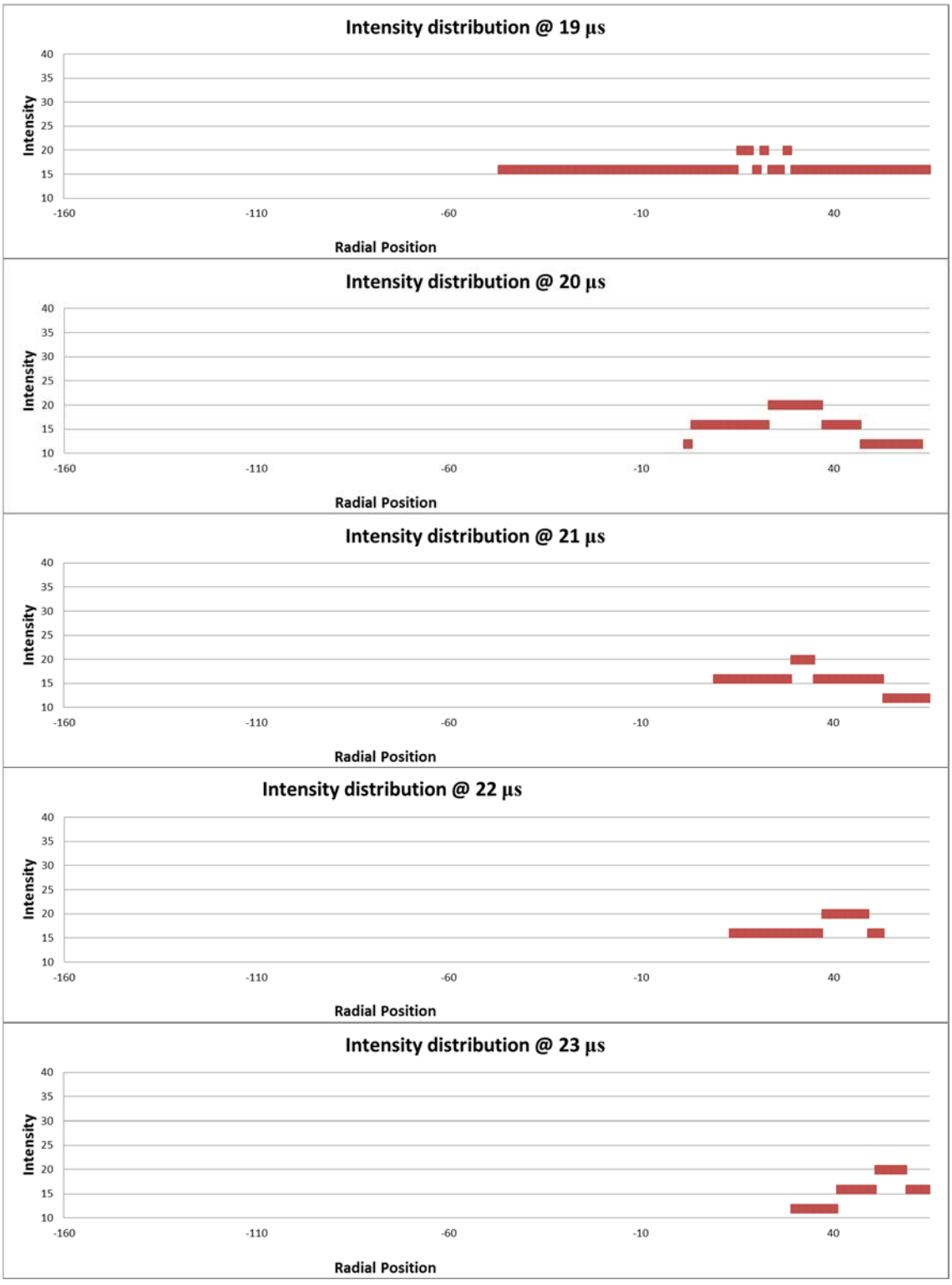
Intensity distribution @ 19 µs
Intensity distribution @ 20 µs
Intensity distribution @ 21 µs
Intensity distribution @ 22 µs
Intensity distribution @ 23 µs
Intensity
Radial Position
40
35
30
25
20
15
10
-160
-110
-60
-10
40

Unrolled plot 3 spoke 1

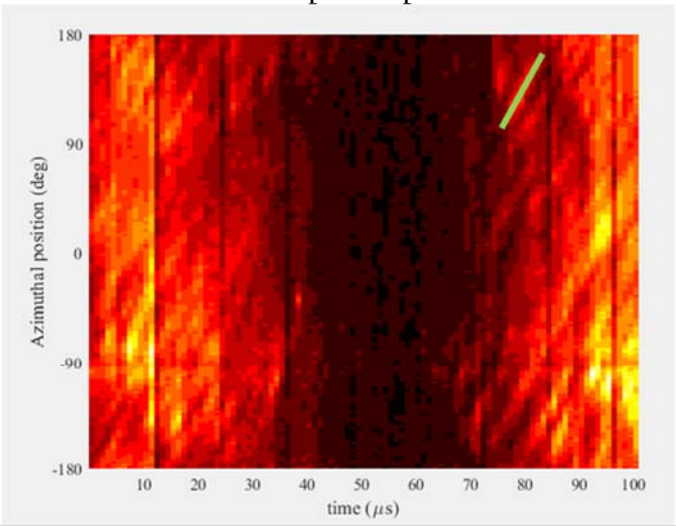

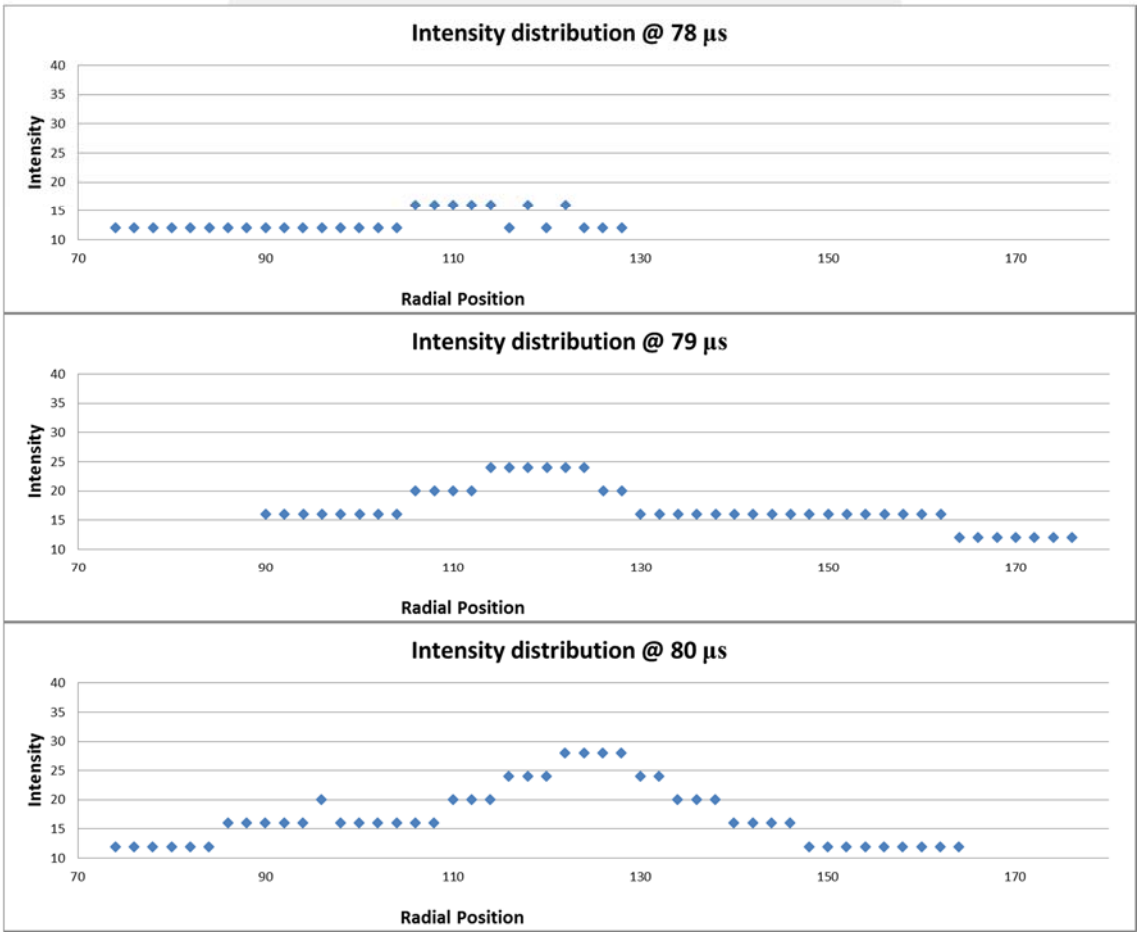

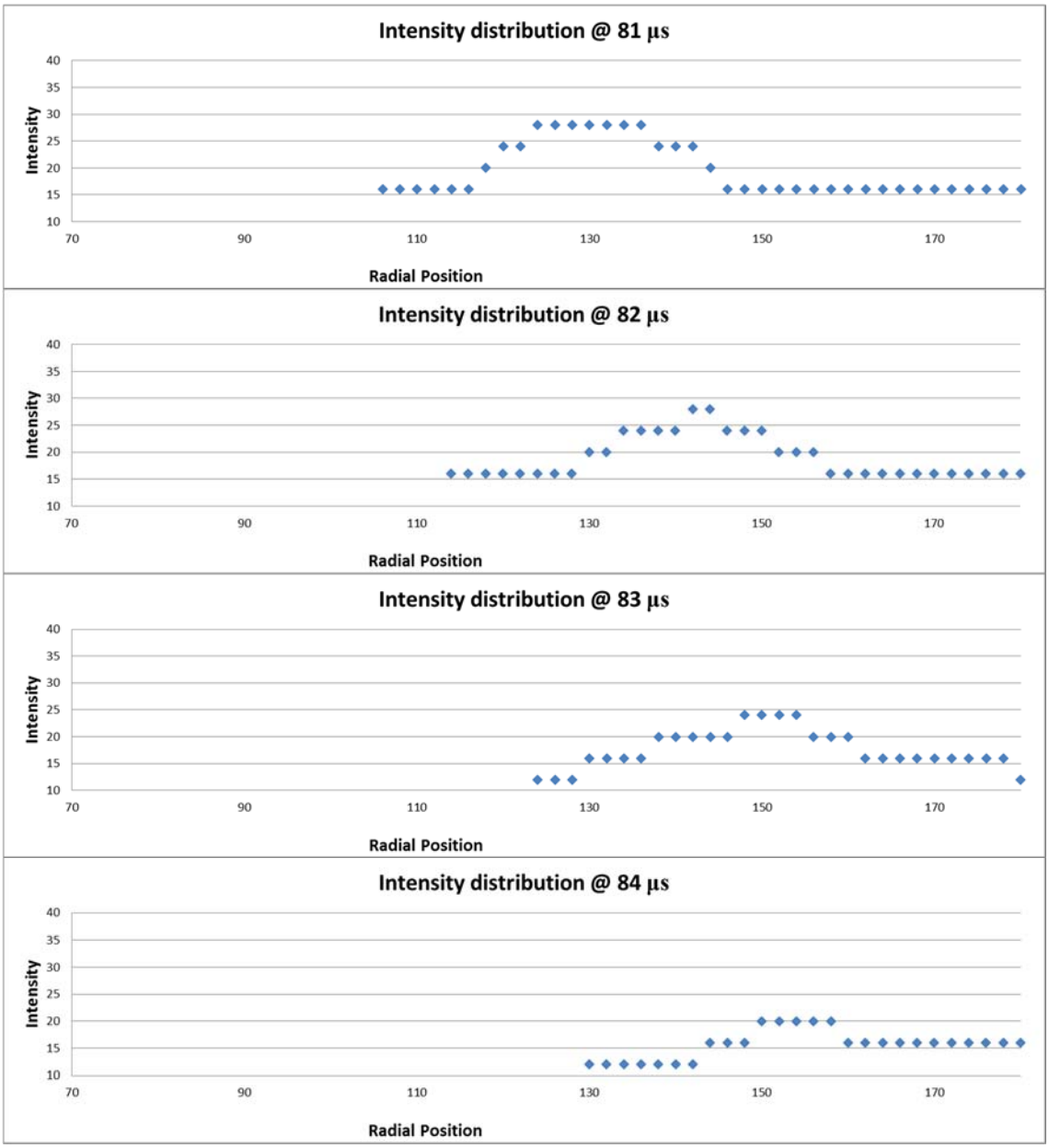
Intensity distribution @ 81 µs
Intensity
Radial Position
Intensity distribution @ 82 µs
Intensity
Radial Position
Intensity distribution @ 83 µs
Intensity
Radial Position
Intensity distribution @ 84 µs
Intensity
Radial Position

Unrolled plot 3 spoke 2

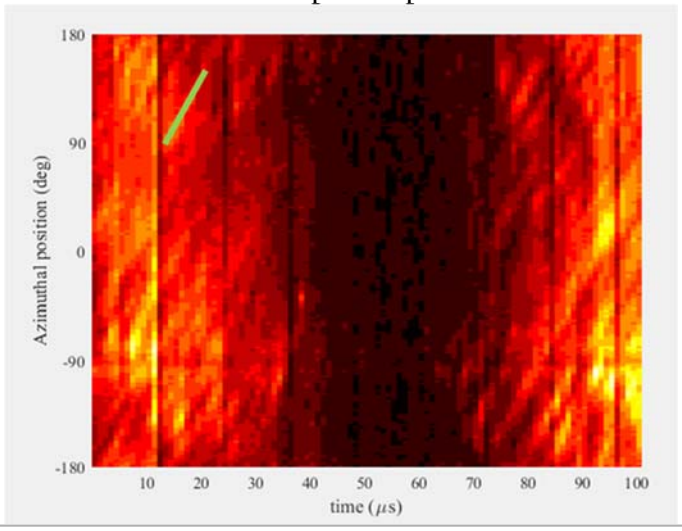

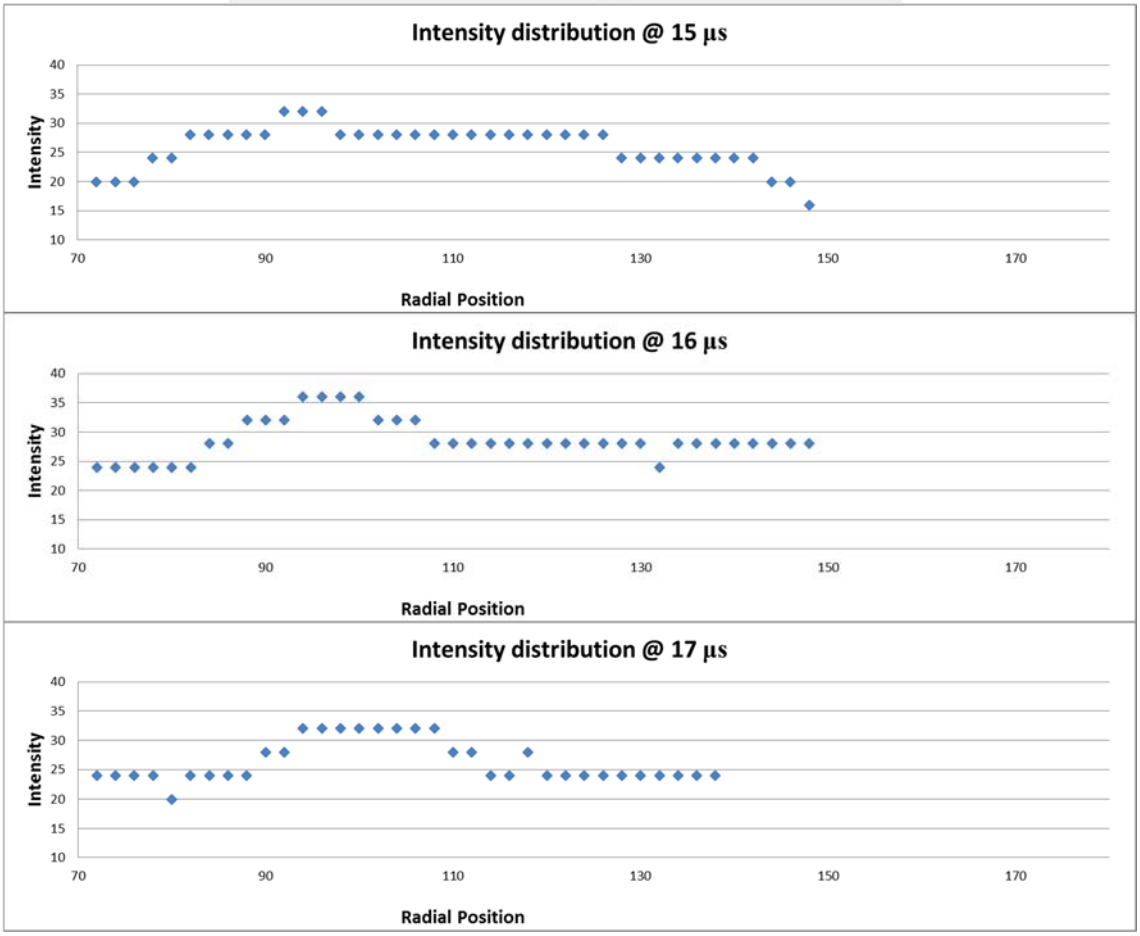

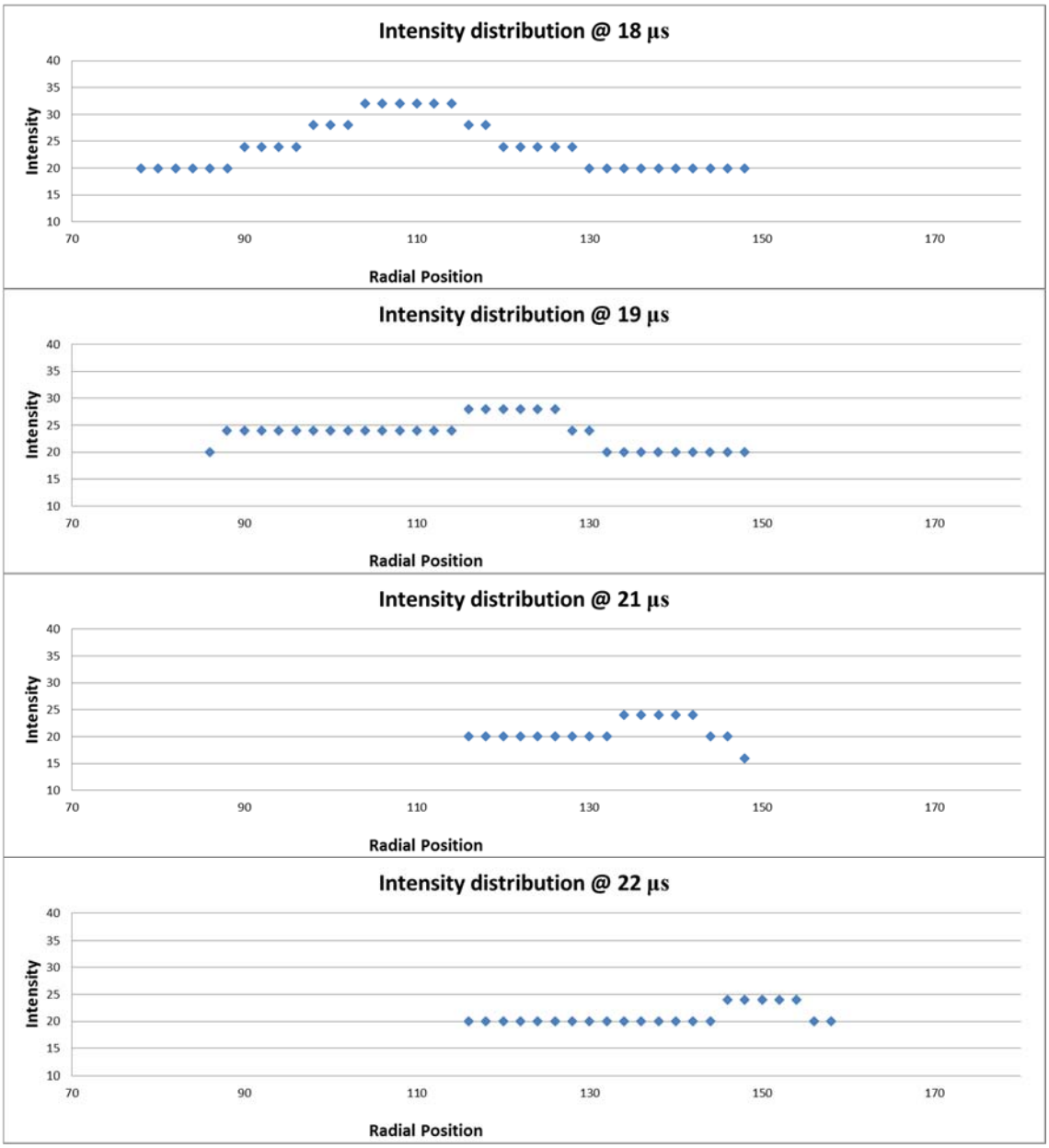
Intensity distribution @ 18 µs
Intensity
Radial Position
Intensity distribution @ 19 µs
Intensity
Radial Position
Intensity distribution @ 21 µs
Intensity
Radial Position
Intensity distribution @ 22 µs
Intensity
Radial Position

Unrolled Plot 4 Spoke 1

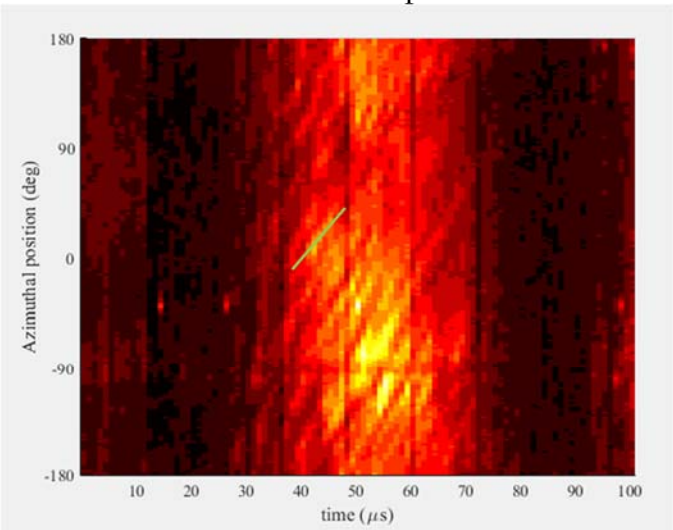

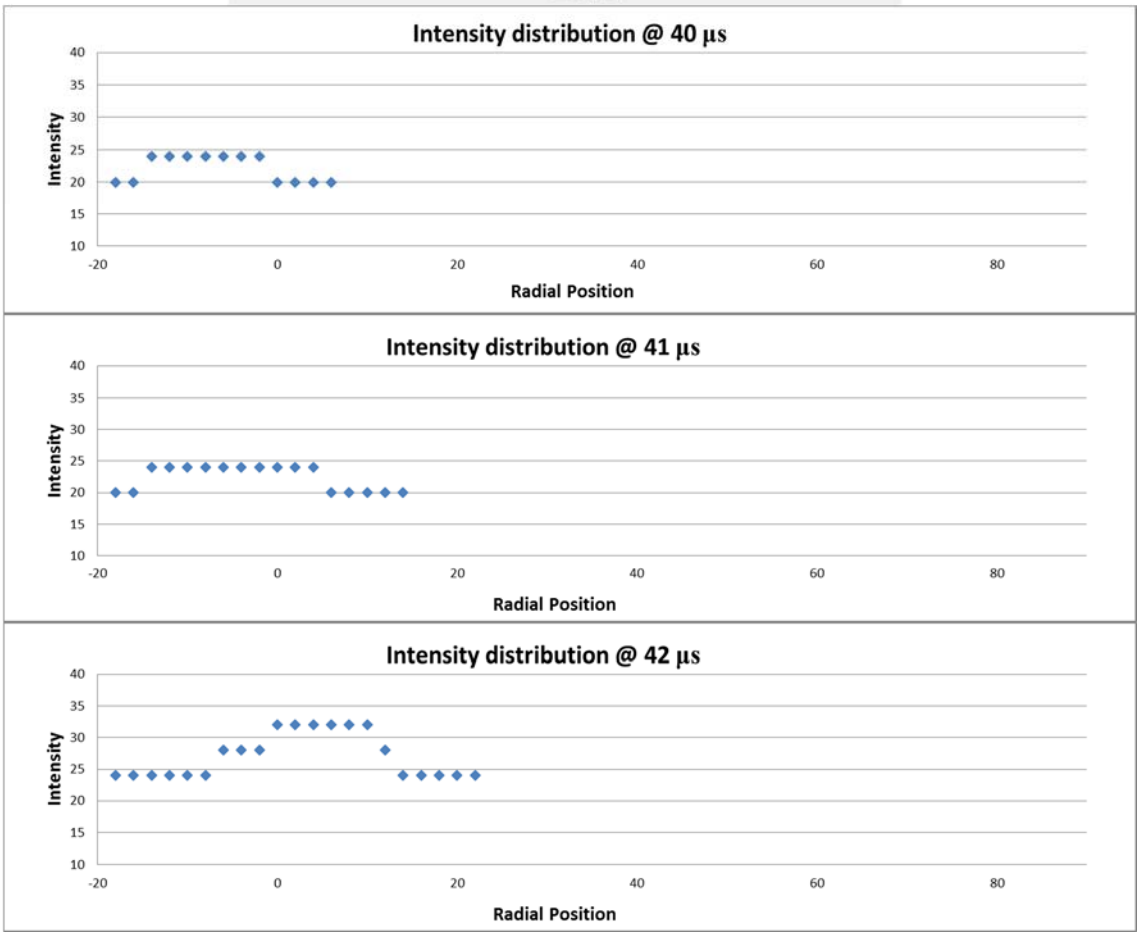

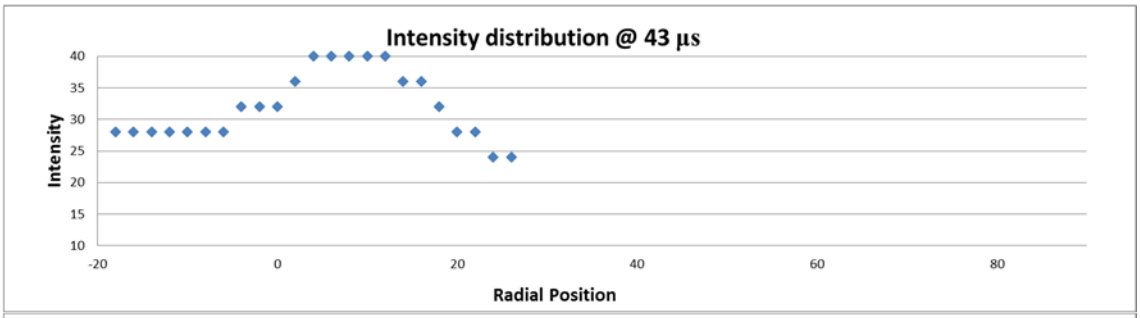
Intensity distribution @ 43 µs
Intensity
Radial Position

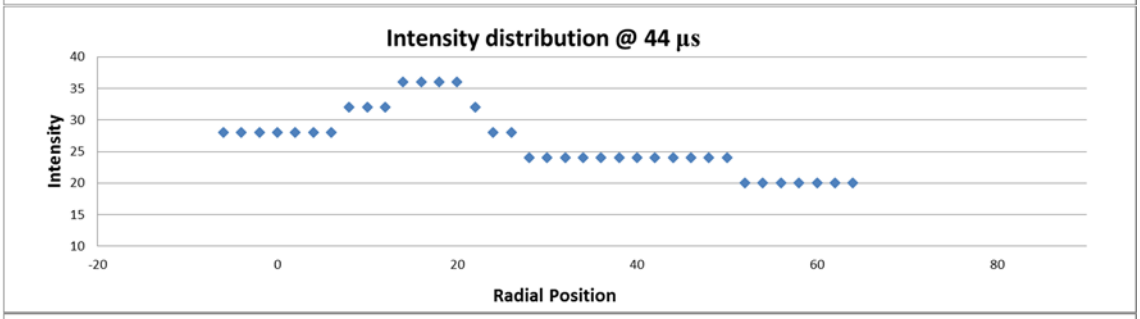
Intensity distribution @ 44 µs
Intensity
Radial Position

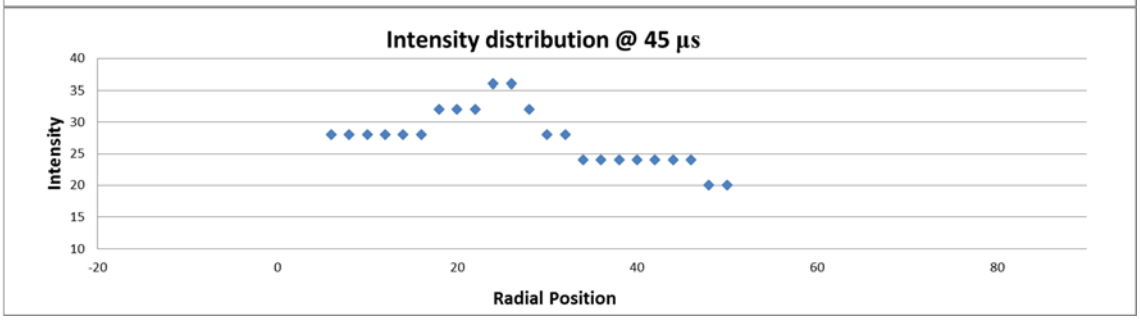
Intensity distribution @ 45 µs
Intensity
Radial Position

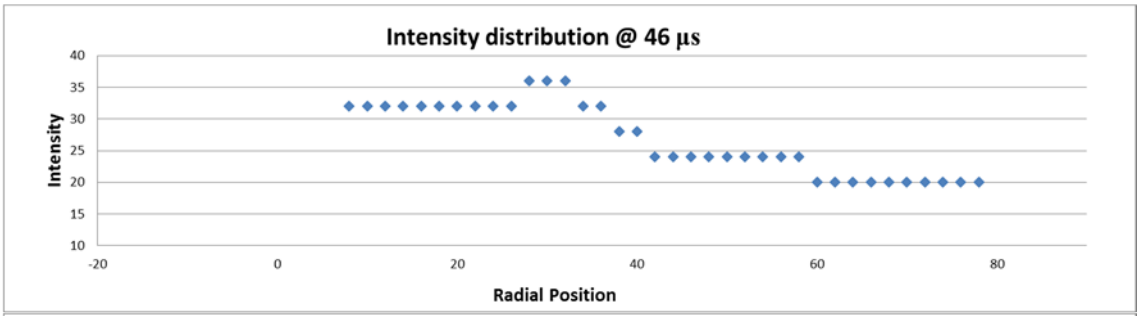
Intensity distribution @ 46 µs
Intensity
Radial Position

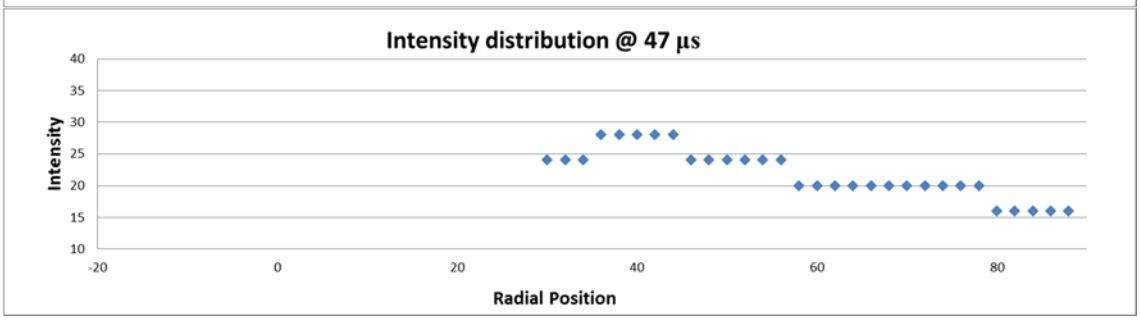
Intensity distribution @ 47 µs
Intensity
Radial Position

Unrolled plot 5

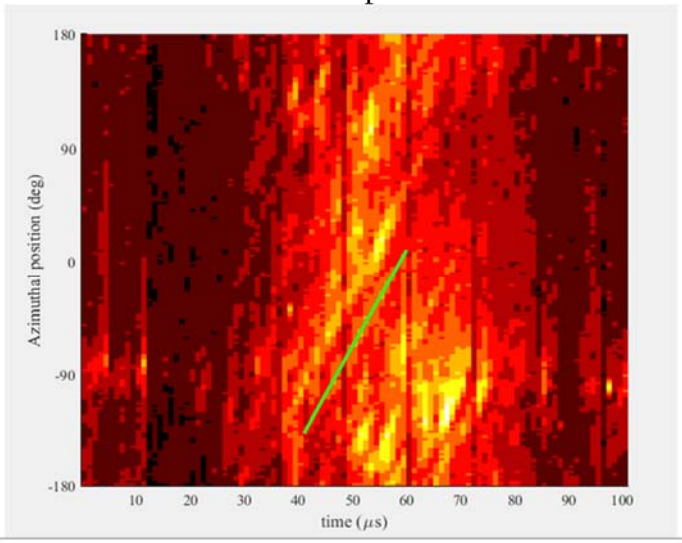

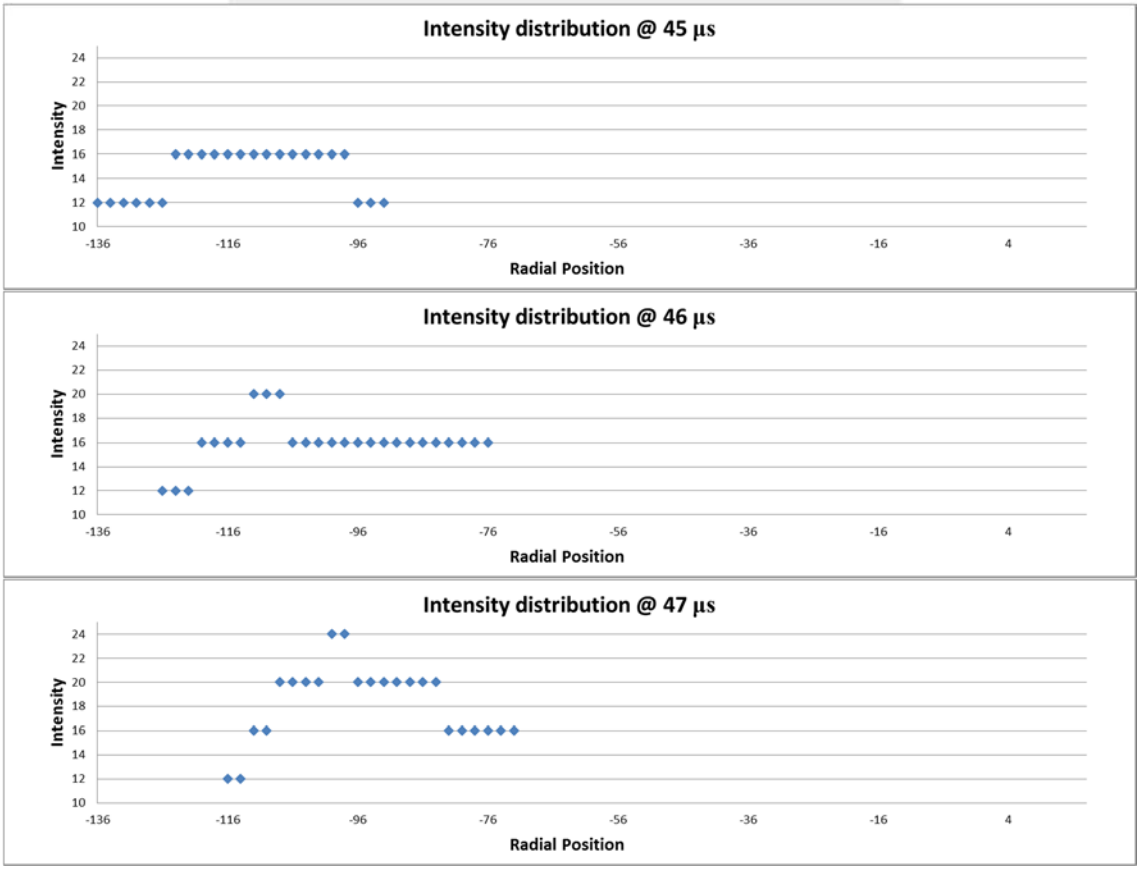

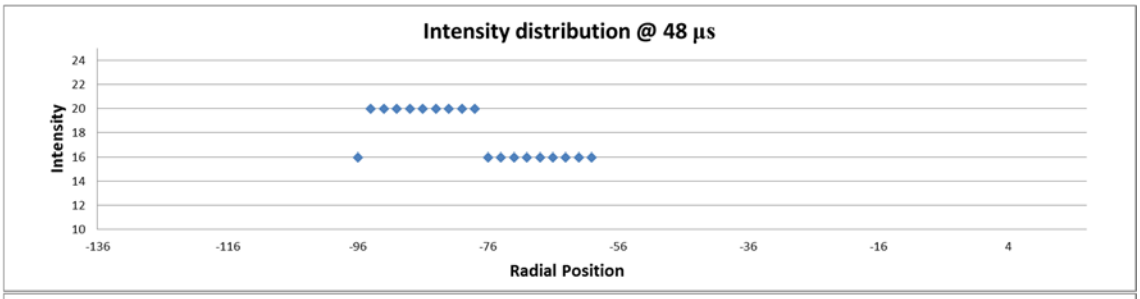
Intensity distribution @ 48 µs
Intensity
24
22
20
18
16
14
12
10
-136
-116
-96
-76
-56
-36
-16
4
Radial Position

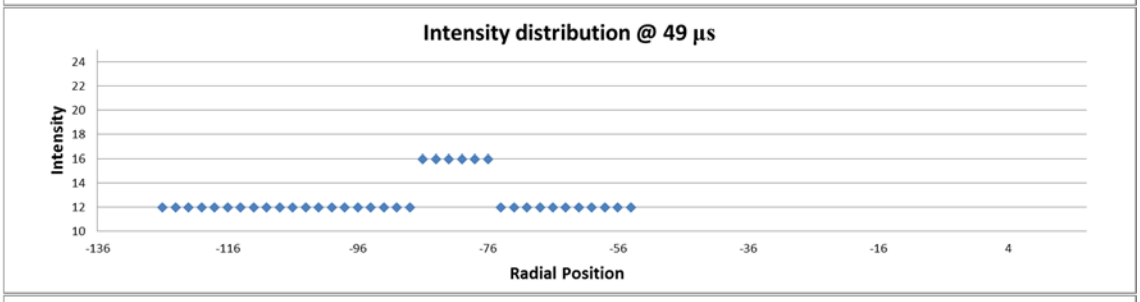
Intensity distribution @ 49 µs
Intensity
24
22
20
18
16
14
12
10
-136
-116
-96
-76
-56
-36
-16
4
Radial Position

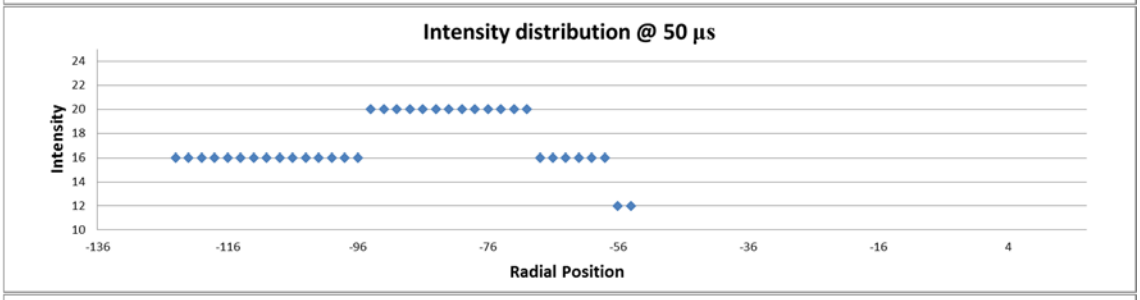
Intensity distribution @ 50 µs
Intensity
24
22
20
18
16
14
12
10
-136
-116
-96
-76
-56
-36
-16
4
Radial Position

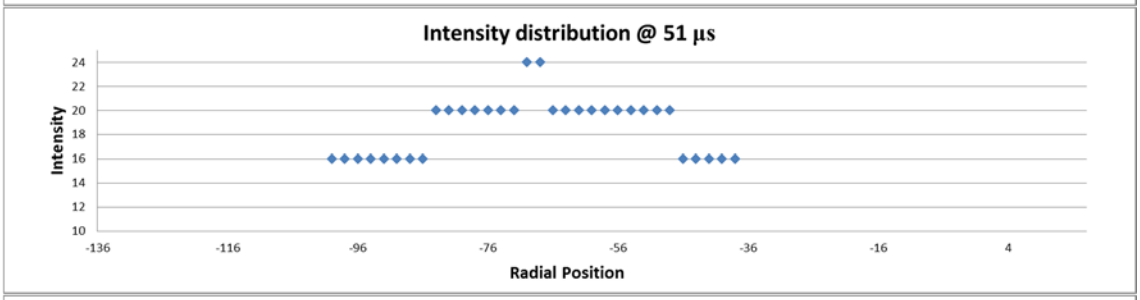
Intensity distribution @ 51 µs
Intensity
24
22
20
18
16
14
12
10
-136
-116
-96
-76
-56
-36
-16
4
Radial Position

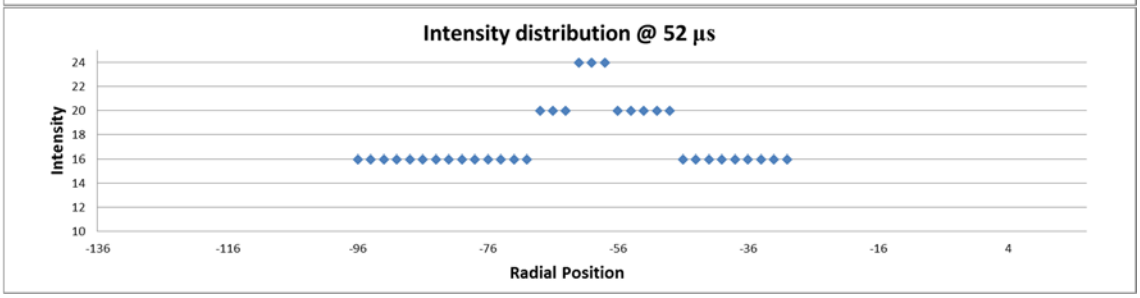
Intensity distribution @ 52 µs
Intensity
24
22
20
18
16
14
12
10
-136
-116
-96
-76
-56
-36
-16
4
Radial Position

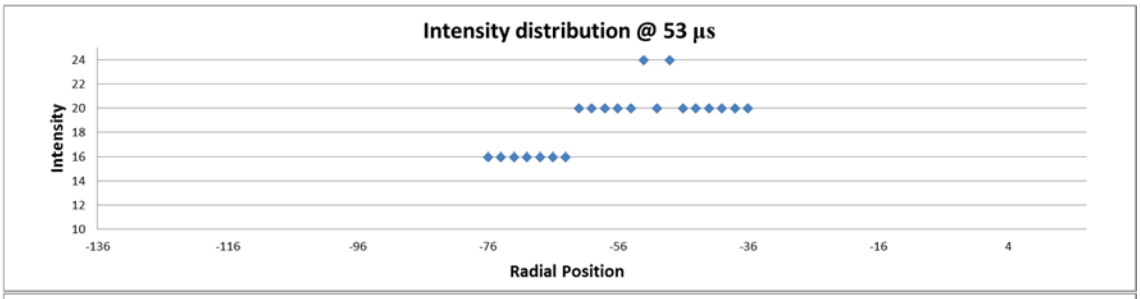
Intensity distribution @ 53 µs
Intensity
24
22
20
18
16
14
12
10
-136
-116
-96
-76
-56
-36
-16
4
Radial Position

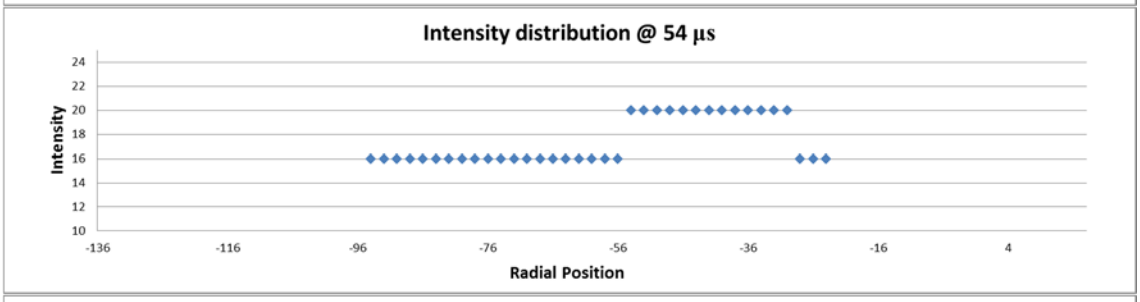
Intensity distribution @ 54 µs
Intensity
24
22
20
18
16
14
12
10
-136
-116
-96
-76
-56
-36
-16
4
Radial Position

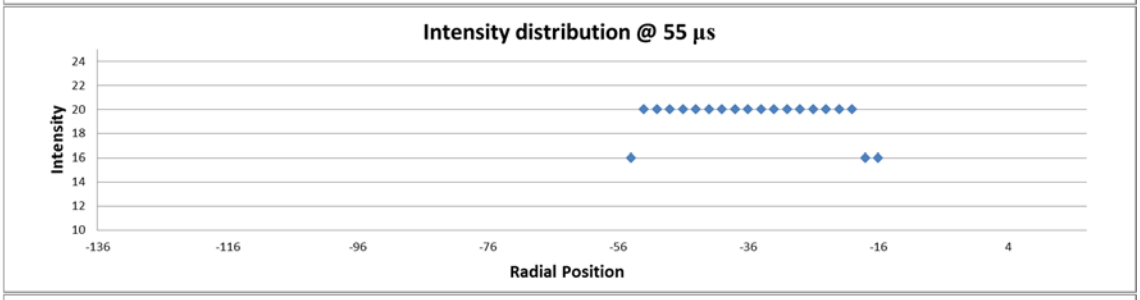
Intensity distribution @ 55 µs
Intensity
24
22
20
18
16
14
12
10
-136
-116
-96
-76
-56
-36
-16
4
Radial Position

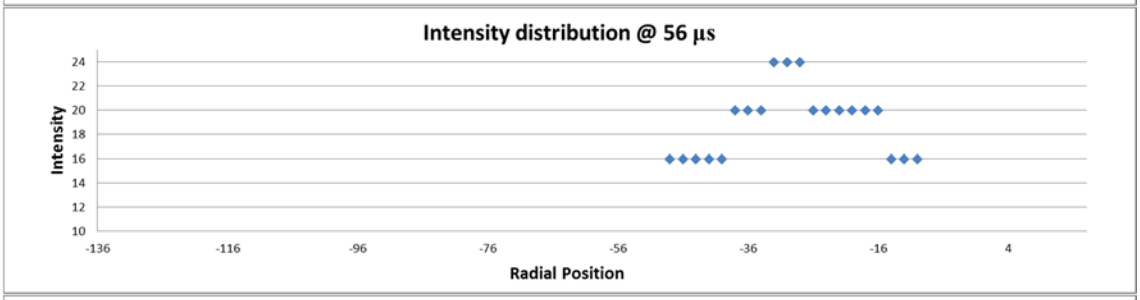
Intensity distribution @ 56 µs
Intensity
24
22
20
18
16
14
12
10
-136
-116
-96
-76
-56
-36
-16
4
Radial Position

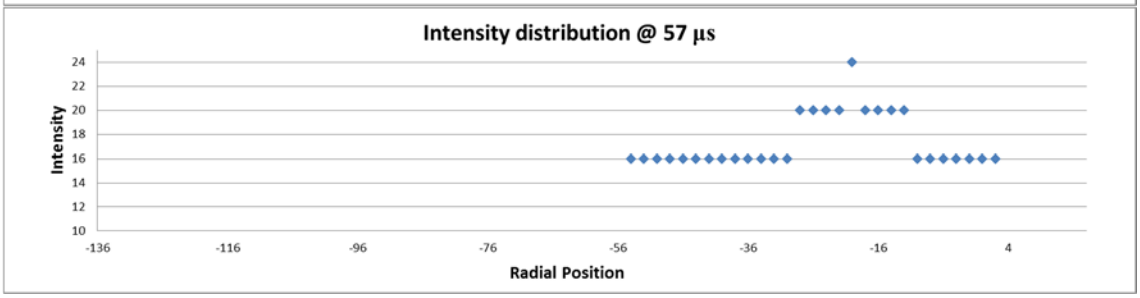
Intensity distribution @ 57 µs
Intensity
24
22
20
18
16
14
12
10
-136
-116
-96
-76
-56
-36
-16
4
Radial Position

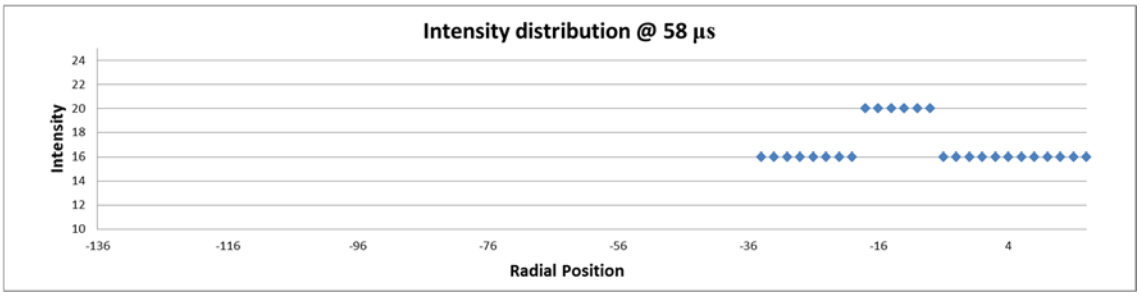
Intensity distribution @ 58 µs
Intensity
24
22
20
18
16
14
12
10
-136
-116
-96
-76
-56
-36
-16
4
Radial Position

Unrolled plot 6 Spoke 1

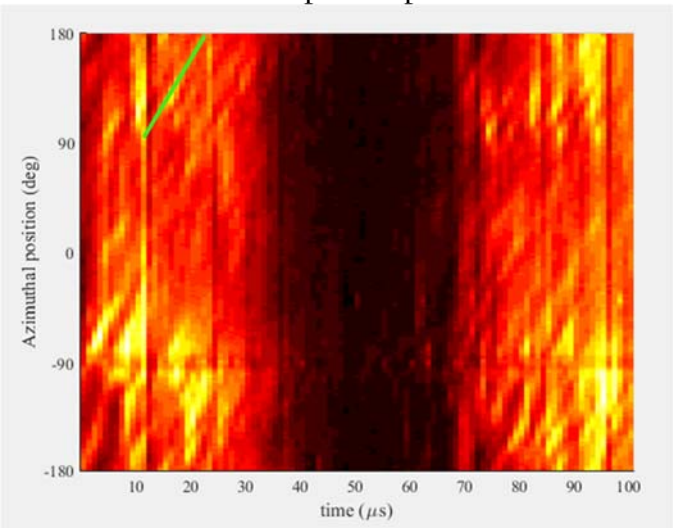

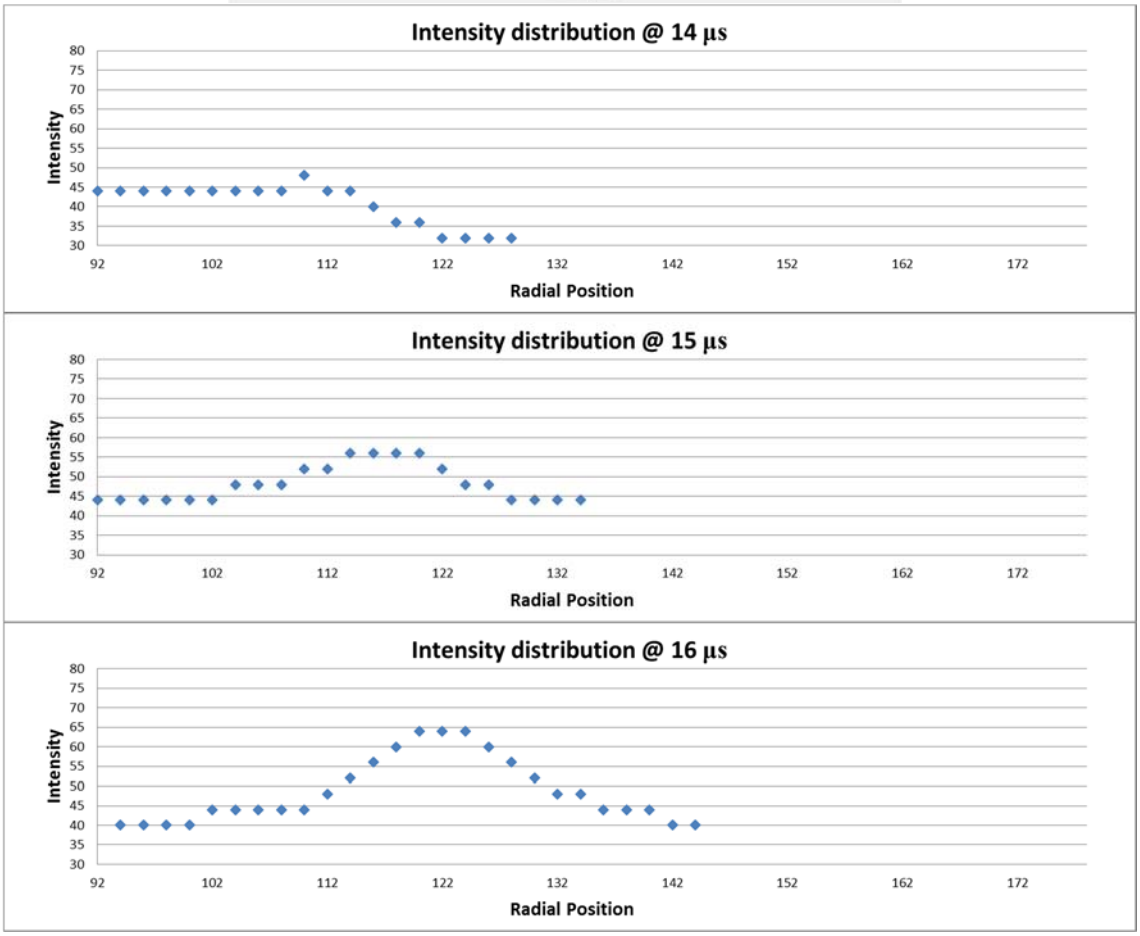

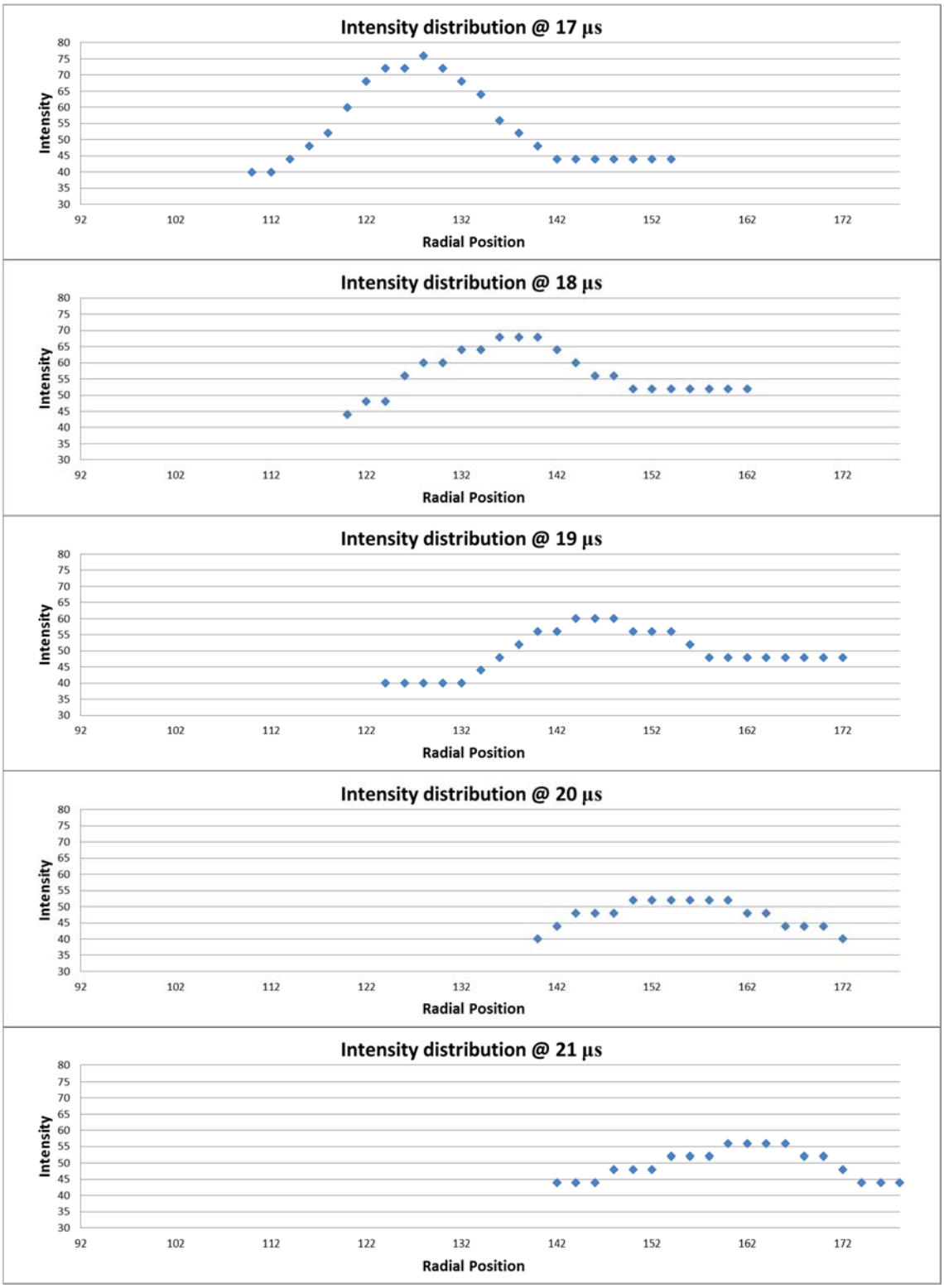
Intensity distribution @ 17 µs
Intensity distribution @ 18 µs
Intensity distribution @ 19 µs
Intensity distribution @ 20 µs
Intensity distribution @ 21 µs
Intensity
Radial Position
80
75
70
65
60
55
50
45
40
35
30
92
102
112
122
132
142
152
162
172

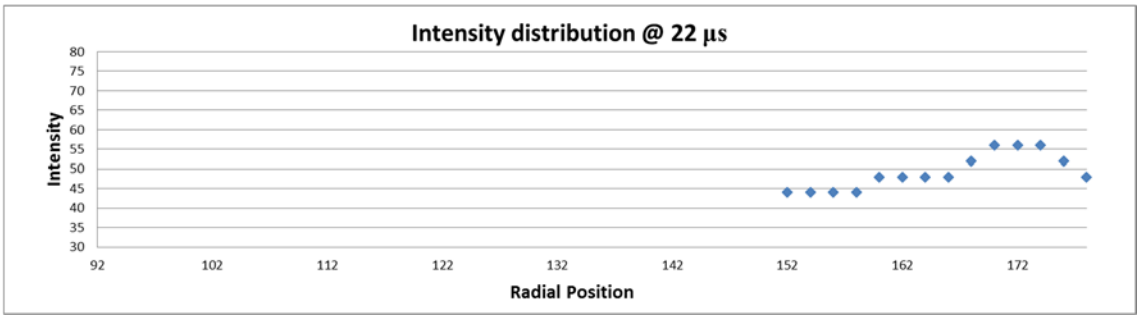
Intensity distribution @ 22 µs
Intensity
80
75
70
65
60
55
50
45
40
35
30
92
102
112
122
132
142
152
162
172
Radial Position

Unrolled plot 7 Spoke 1

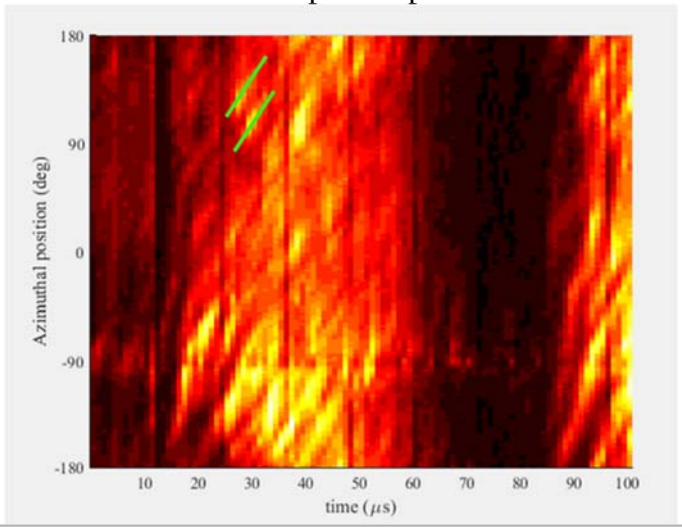

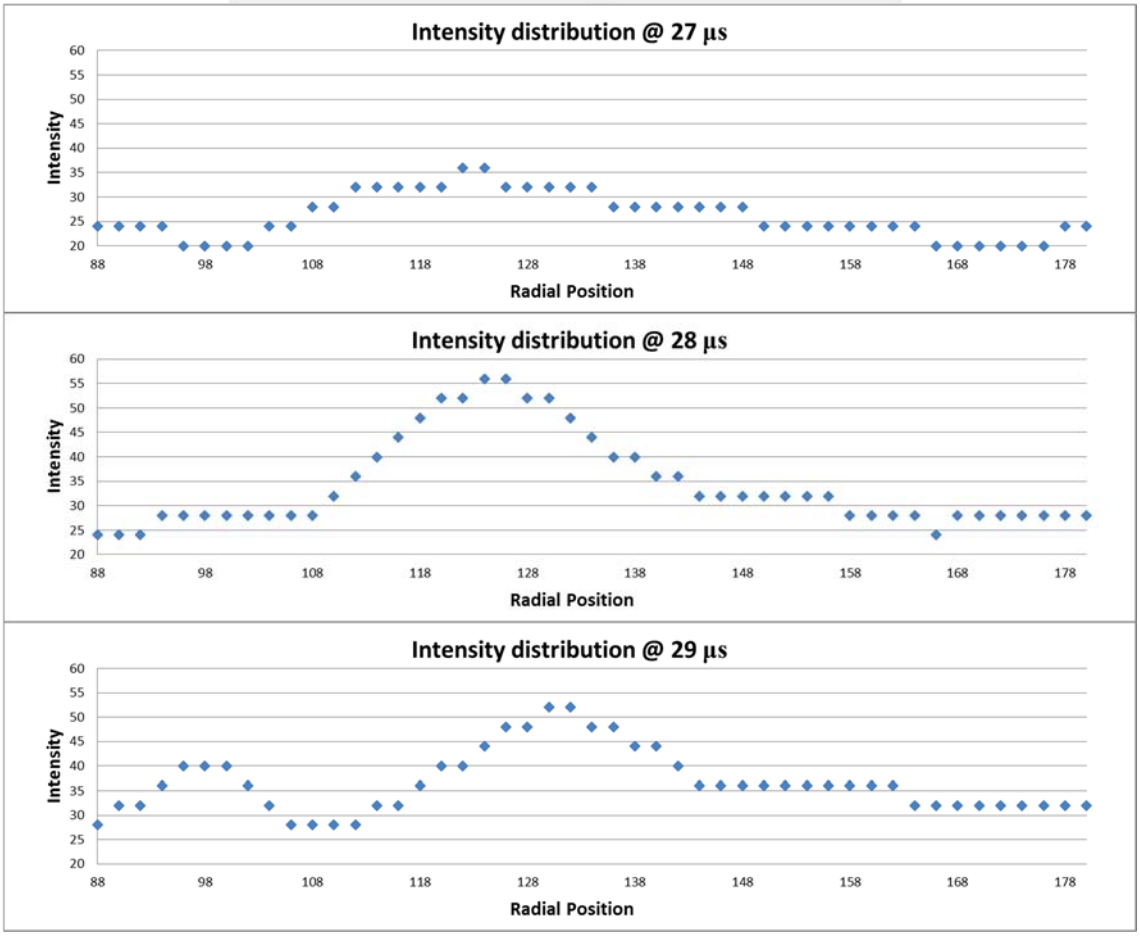

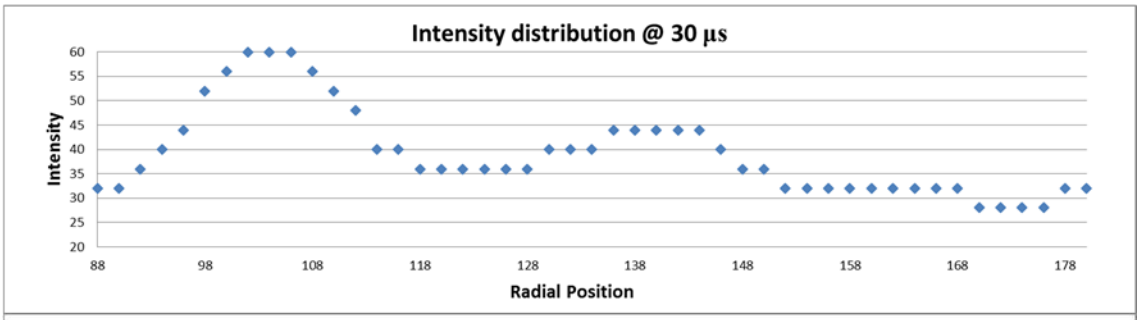
Intensity distribution @ 30 µs
Intensity
Radial Position
60
55
50
45
40
35
30
25
20
88
98
108
118
128
138
148
158
168
178

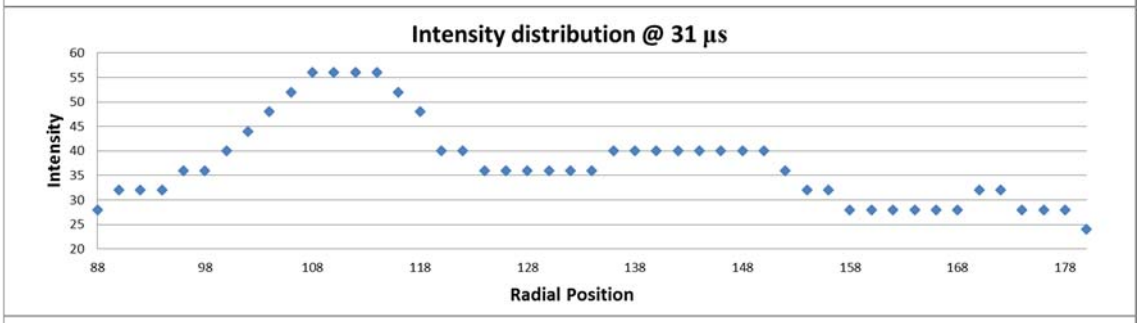
Intensity distribution @ 31 µs
Intensity
Radial Position
60
55
50
45
40
35
30
25
20
88
98
108
118
128
138
148
158
168
178

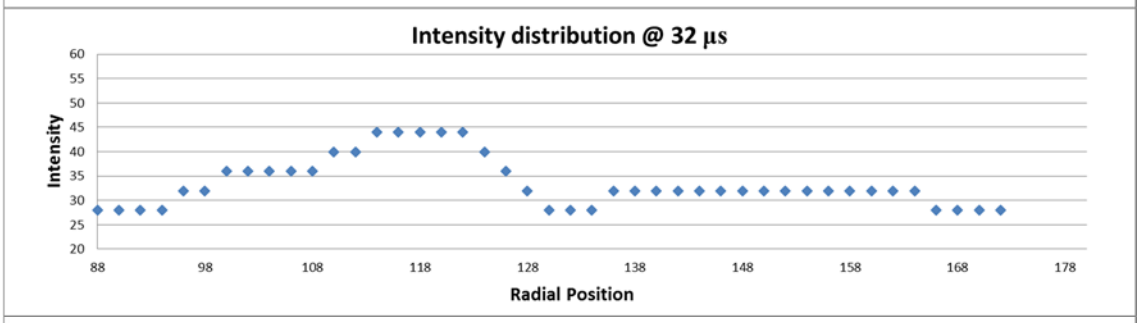
Intensity distribution @ 32 µs
Intensity
Radial Position
60
55
50
45
40
35
30
25
20
88
98
108
118
128
138
148
158
168
178

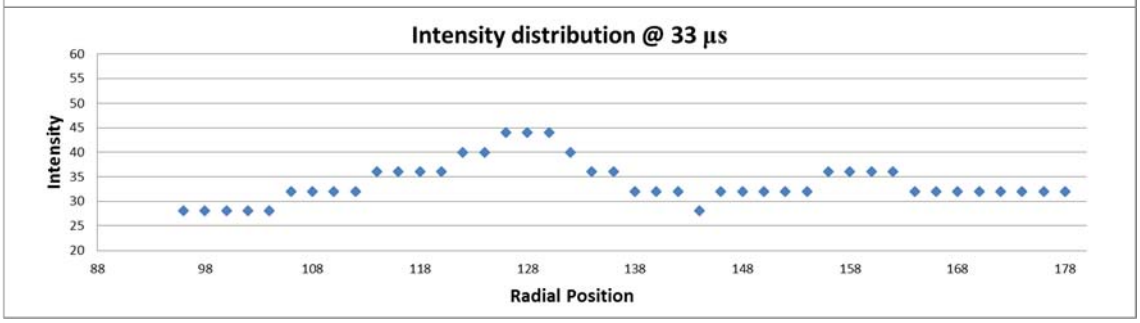
Intensity distribution @ 33 µs
Intensity
Radial Position
60
55
50
45
40
35
30
25
20
88
98
108
118
128
138
148
158
168
178

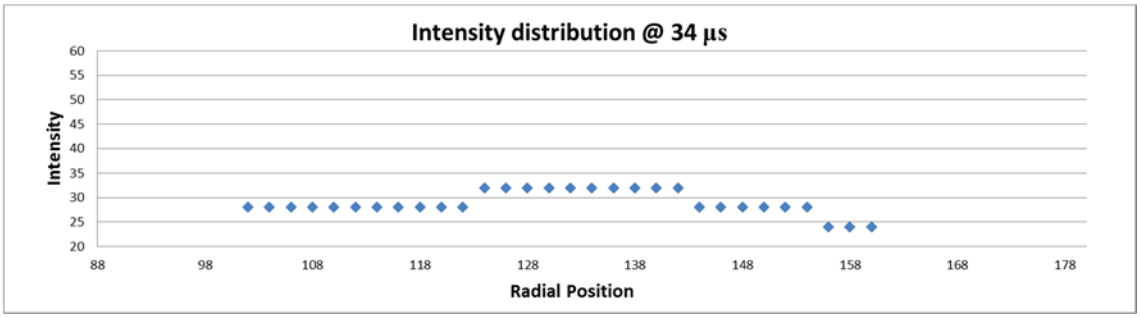
Intensity distribution @ 34 µs
Intensity
Radial Position
60
55
50
45
40
35
30
25
20
88
98
108
118
128
138
148
158
168
178

Unrolled plot b spoke 1

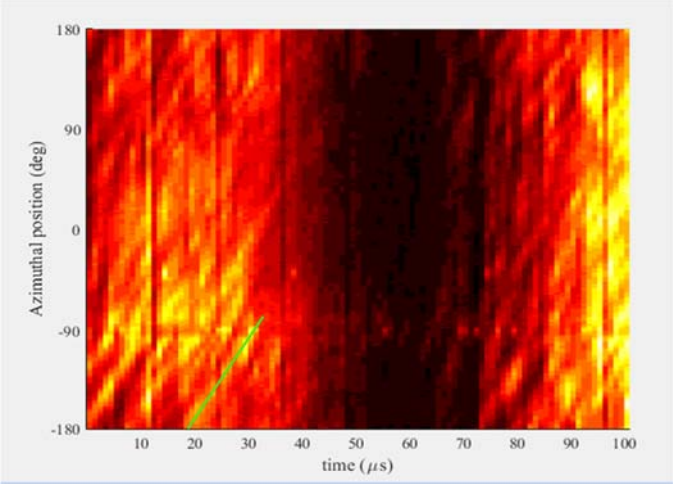

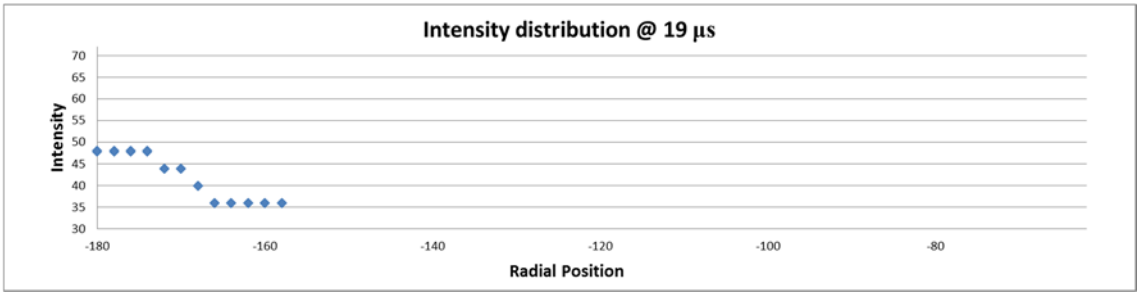

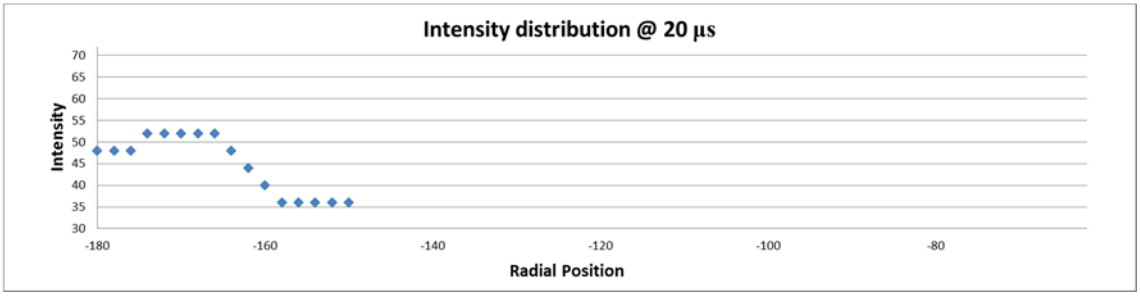

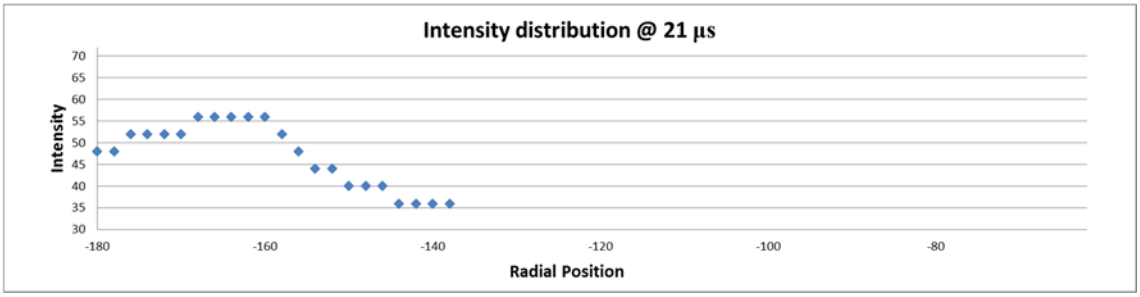

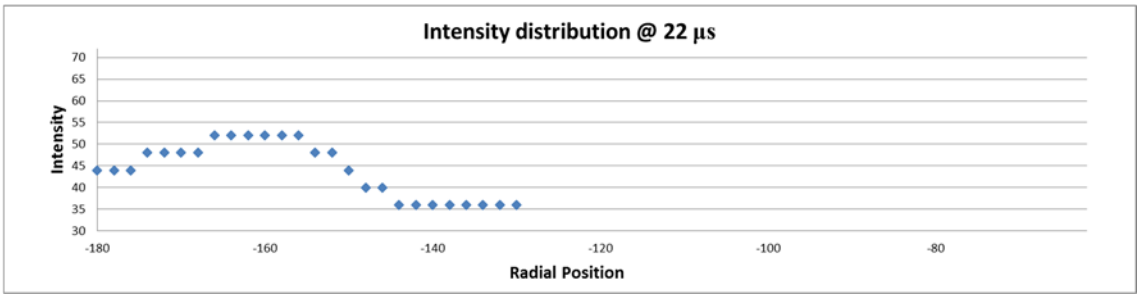
Intensity distribution @ 22 µs
Intensity
70
65
60
55
50
45
40
35
30
-180
-160
-140
-120
-100
-80
Radial Position

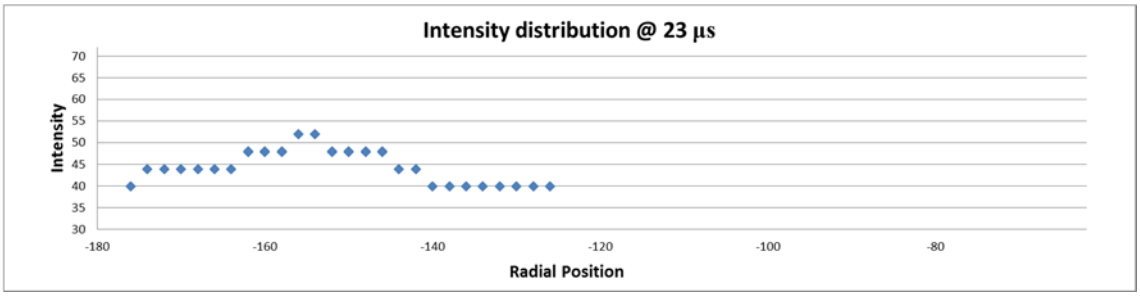
Intensity distribution @ 23 µs
Intensity
70
65
60
55
50
45
40
35
30
-180
-160
-140
-120
-100
-80
Radial Position

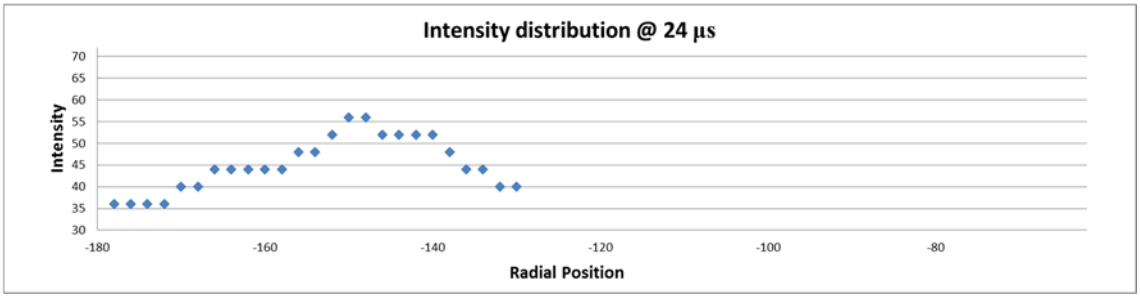
Intensity distribution @ 24 µs
Intensity
70
65
60
55
50
45
40
35
30
-180
-160
-140
-120
-100
-80
Radial Position

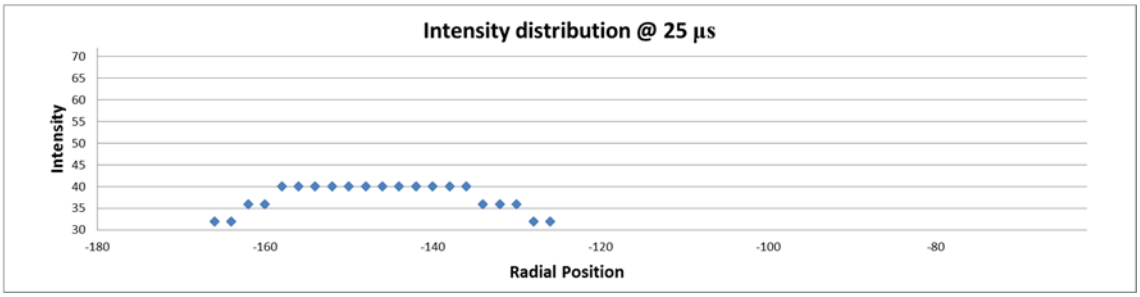
Intensity distribution @ 25 µs
Intensity
70
65
60
55
50
45
40
35
30
-180
-160
-140
-120
-100
-80
Radial Position

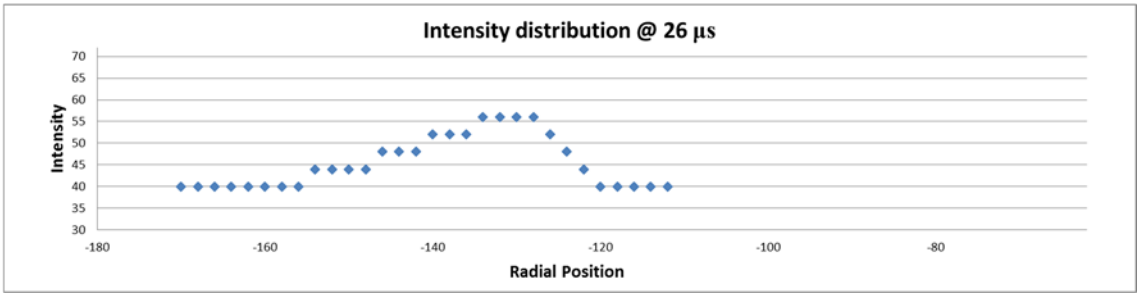
Intensity distribution @ 26 µs
Intensity
70
65
60
55
50
45
40
35
30
-180
-160
-140
-120
-100
-80
Radial Position

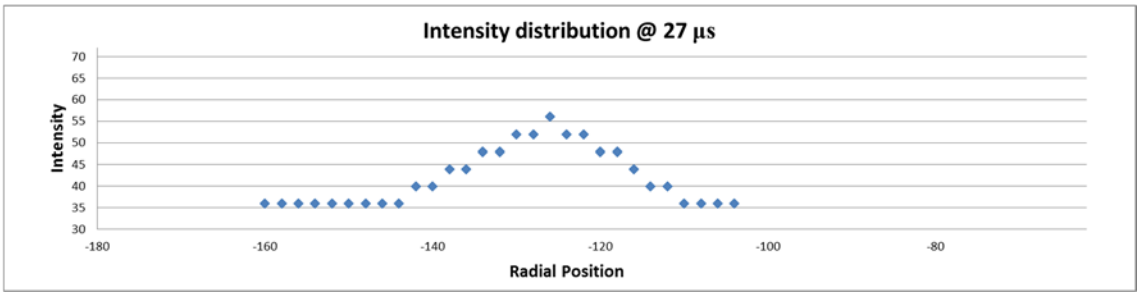
Intensity distribution @ 27 µs
Intensity
70
65
60
55
50
45
40
35
30
-180
-160
-140
-120
-100
-80
Radial Position

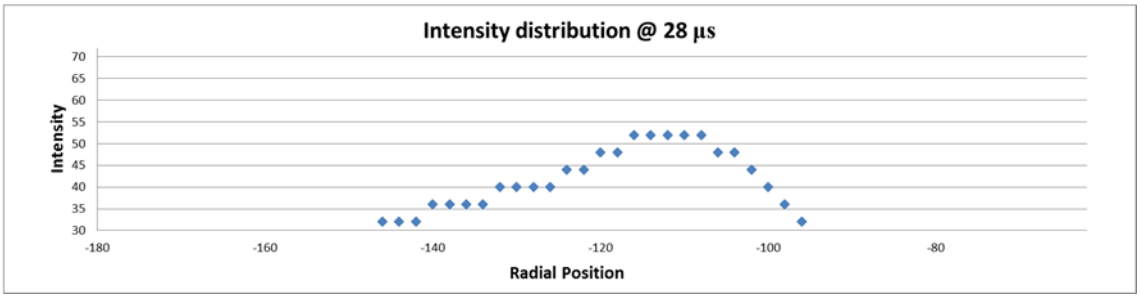
Intensity distribution @ 28 µs
Intensity
70
65
60
55
50
45
40
35
30
-180
-160
-140
-120
-100
-80
Radial Position

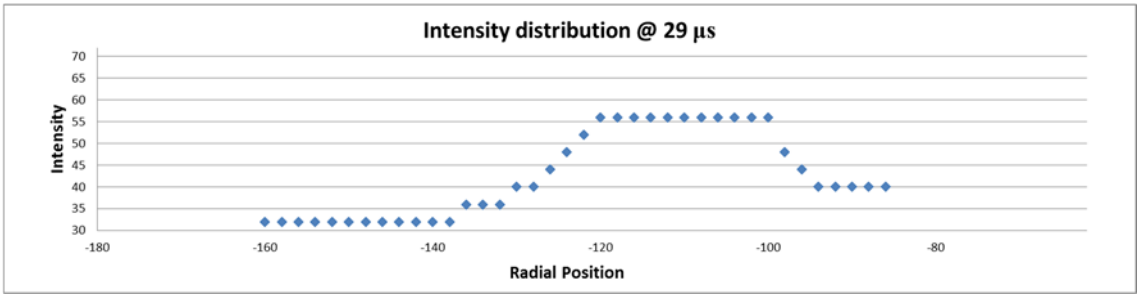
Intensity distribution @ 29 µs
Intensity
70
65
60
55
50
45
40
35
30
-180
-160
-140
-120
-100
-80
Radial Position

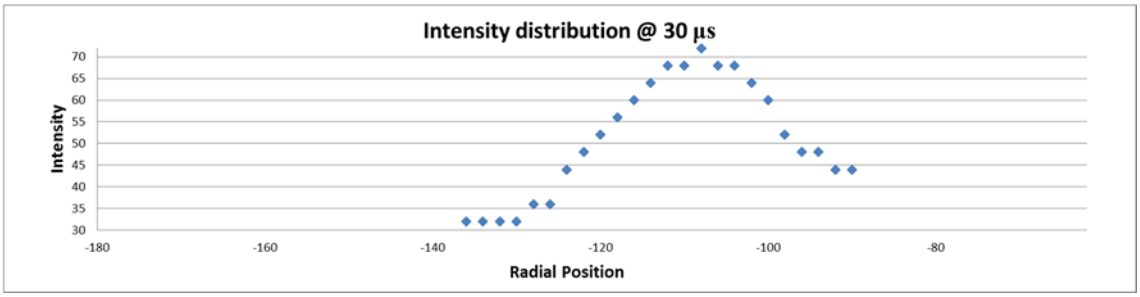
Intensity distribution @ 30 µs
Intensity
70
65
60
55
50
45
40
35
30
-180
-160
-140
-120
-100
-80
Radial Position

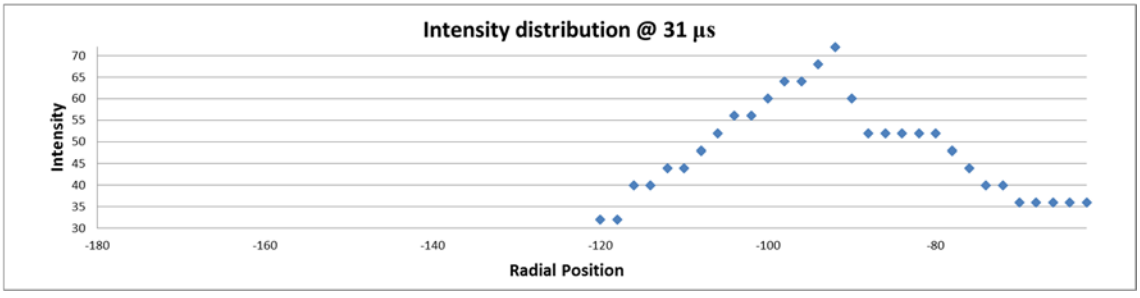
Intensity distribution @ 31 µs
Intensity
70
65
60
55
50
45
40
35
30
-180
-160
-140
-120
-100
-80
Radial Position

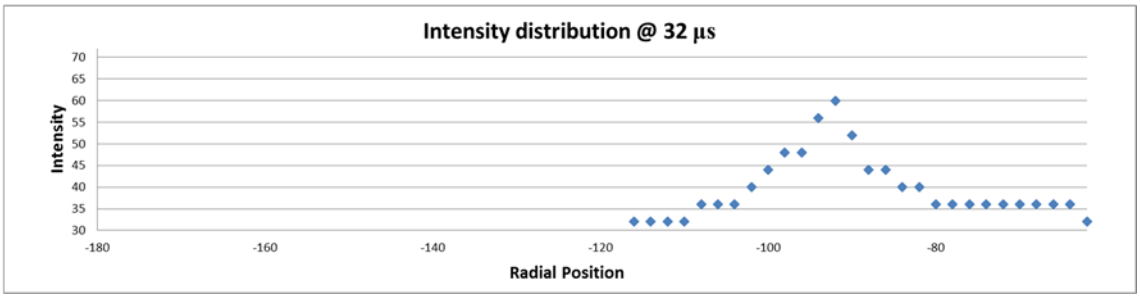
Intensity distribution @ 32 µs
Intensity
70
65
60
55
50
45
40
35
30
-180
-160
-140
-120
-100
-80
Radial Position

Appendix B: Frequency analysis

Unrolled Plot 1

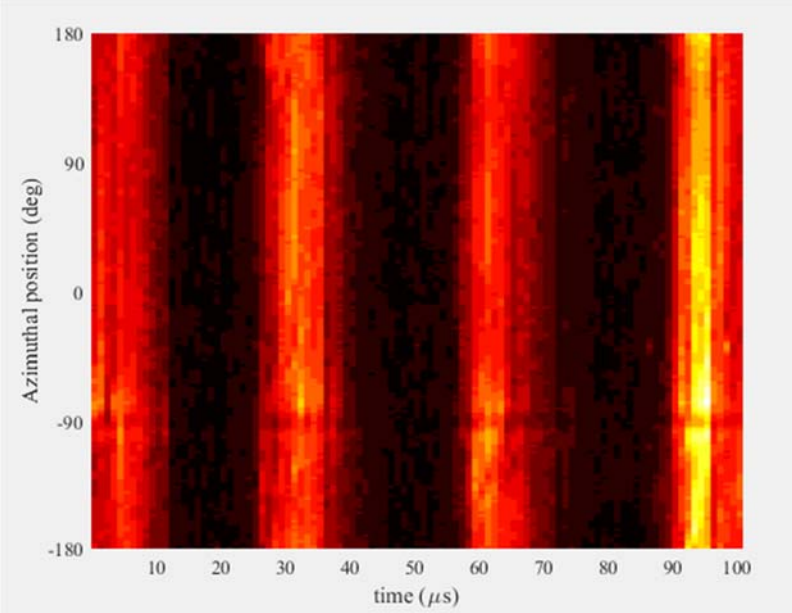

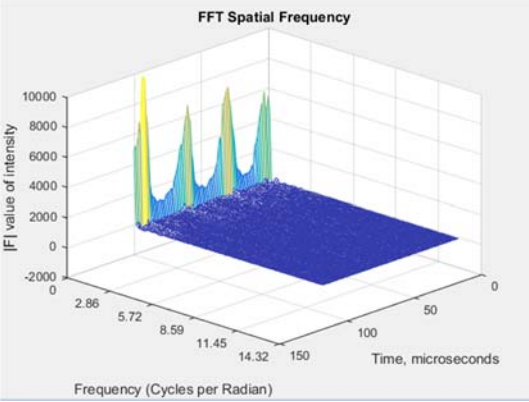

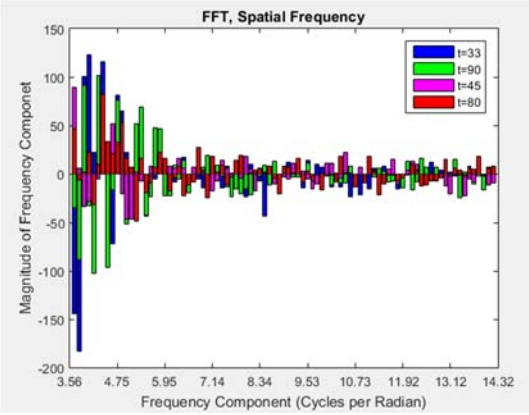

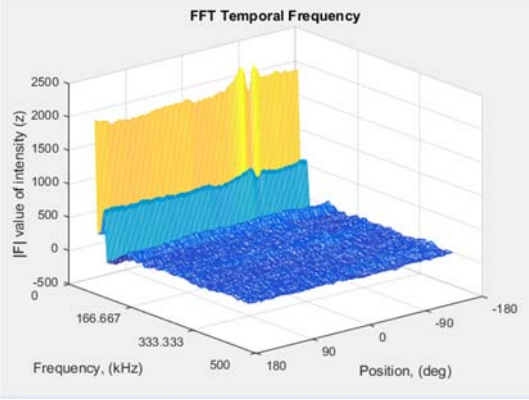

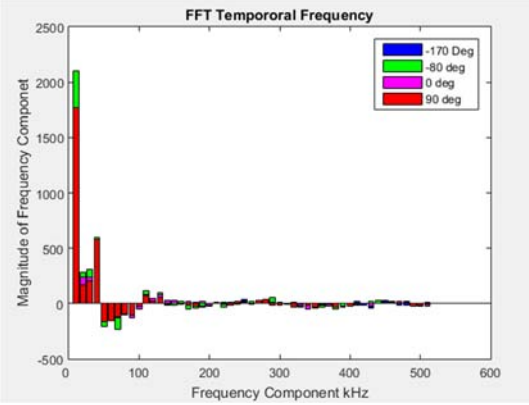

Unrolled Plot 2

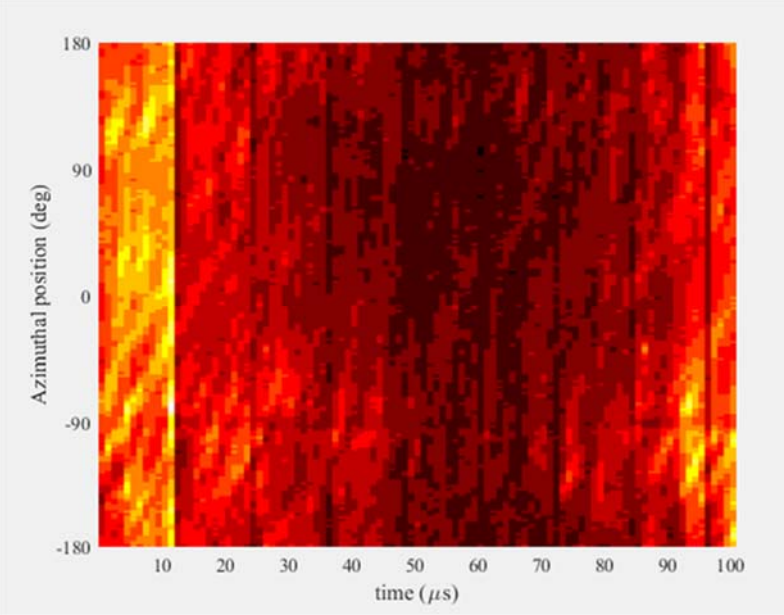

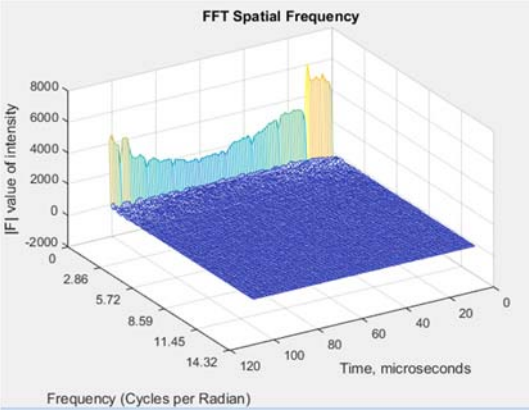

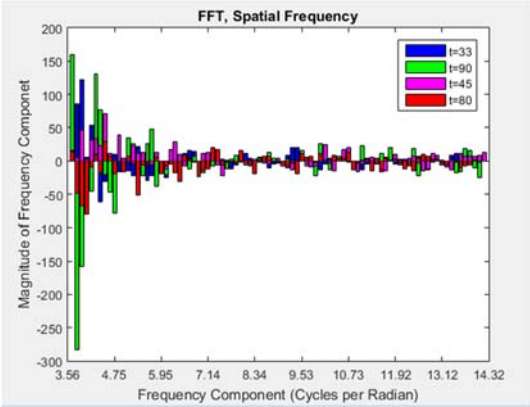

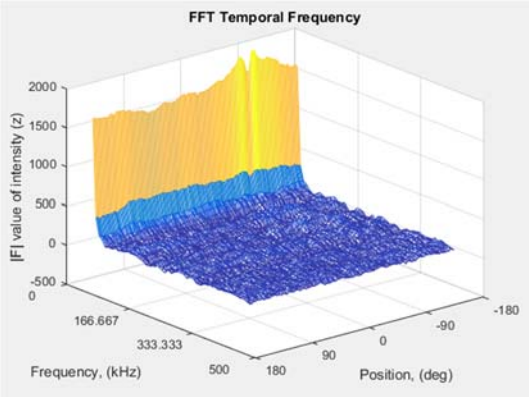

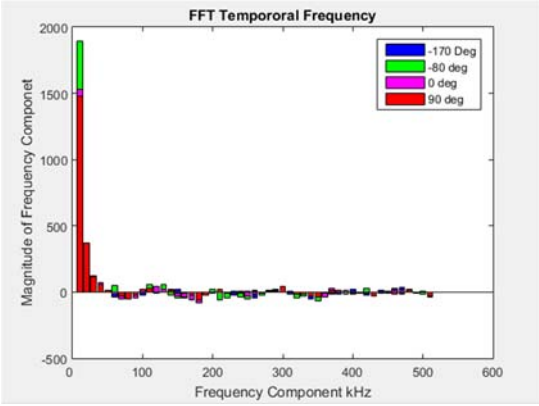

Unrolled Plot 3

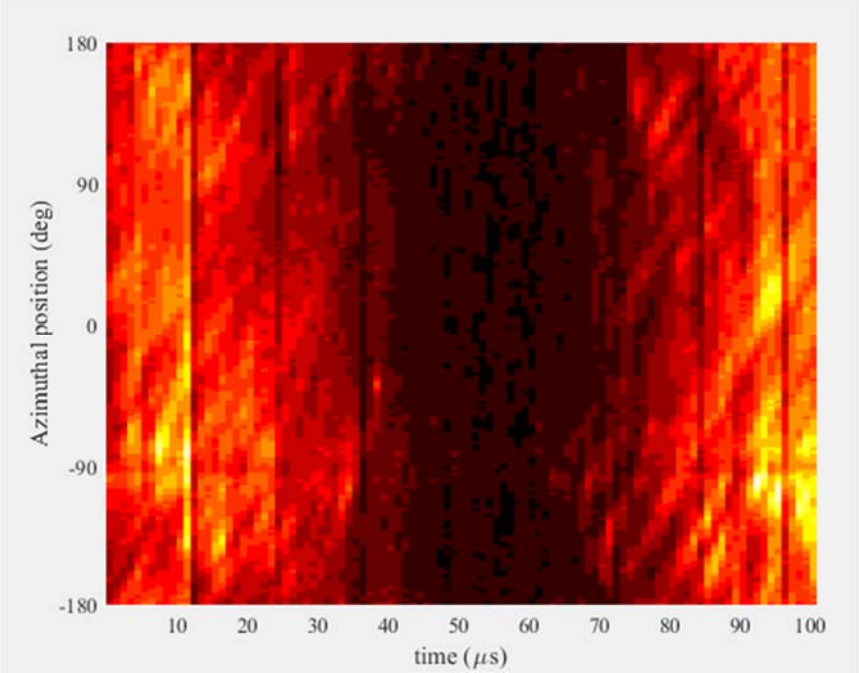

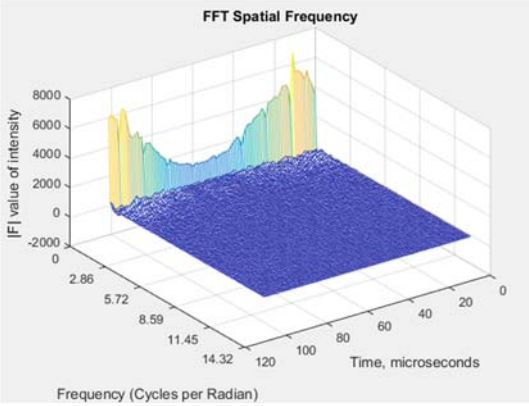

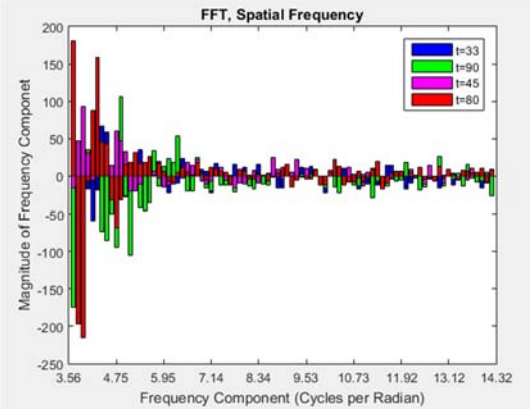

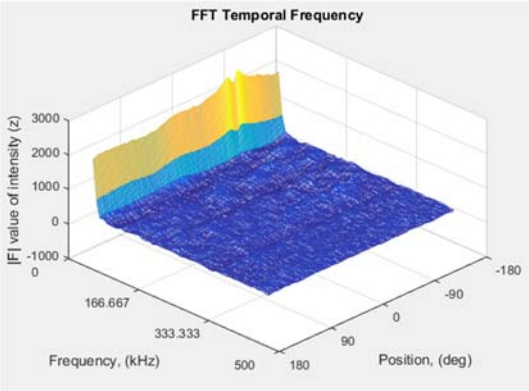

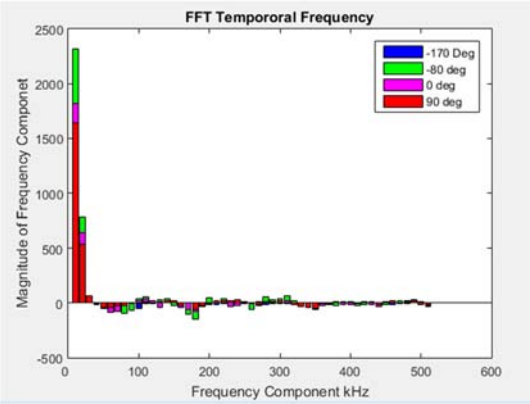

Unrolled Plot 4

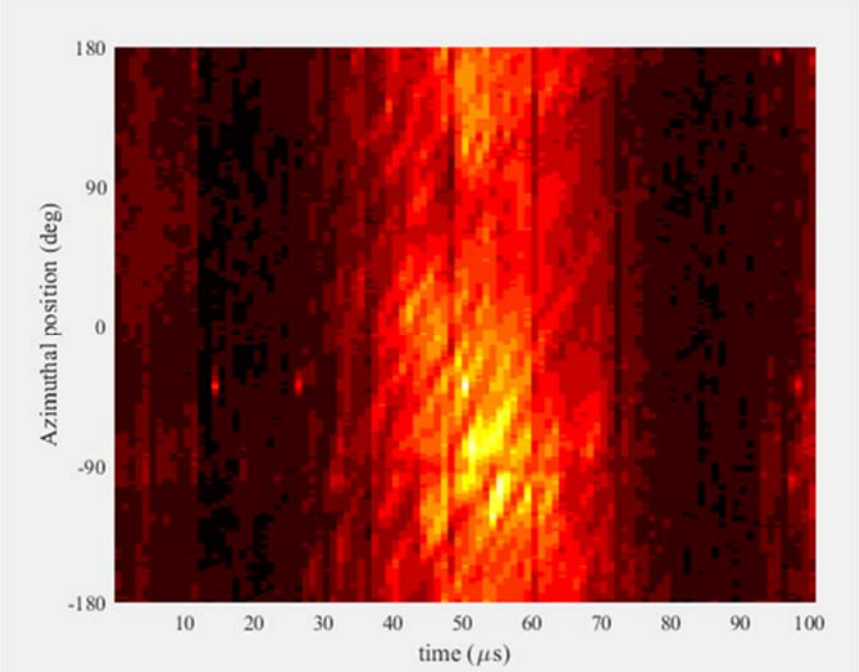

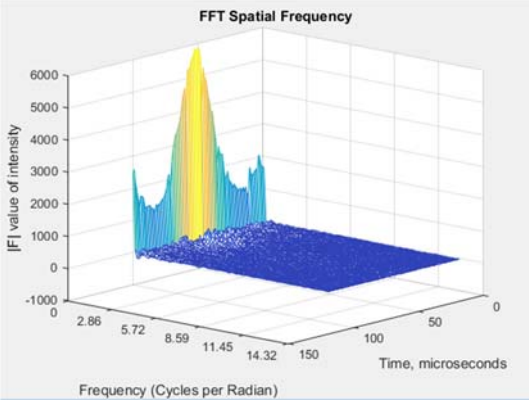

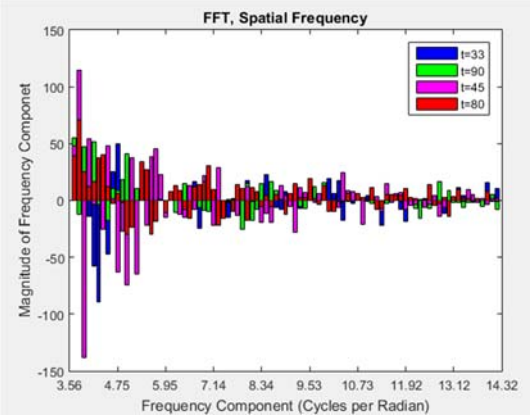

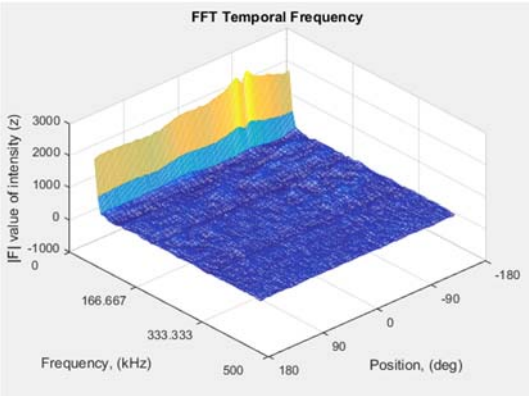

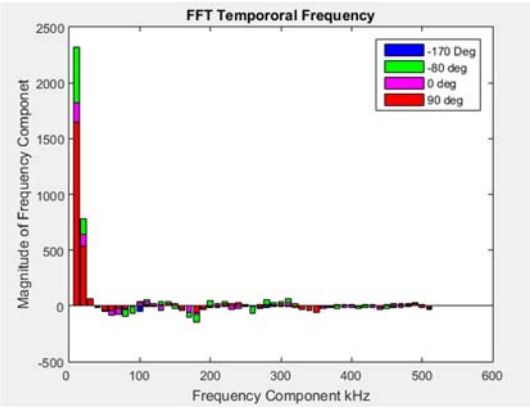

Unrolled Plot 5

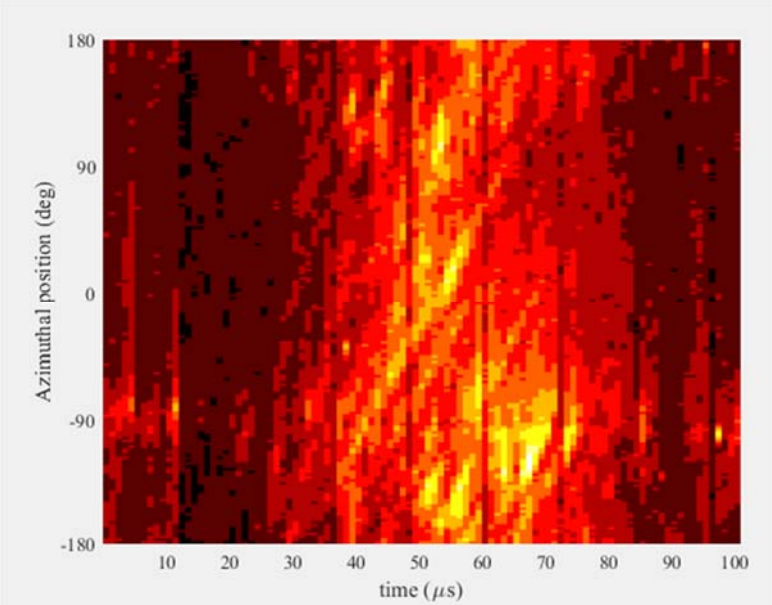

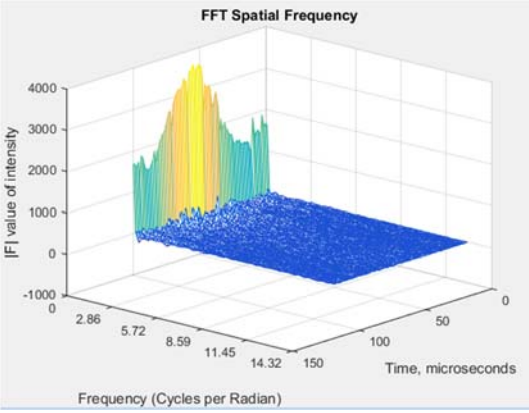

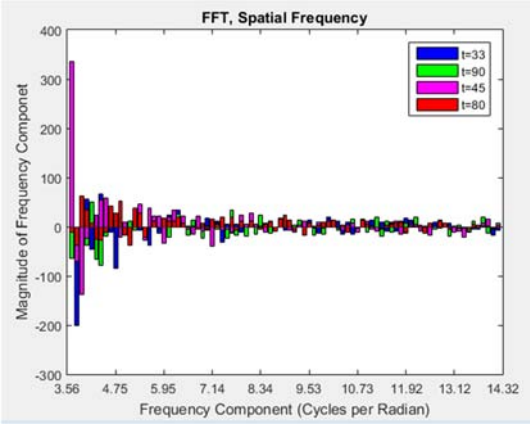

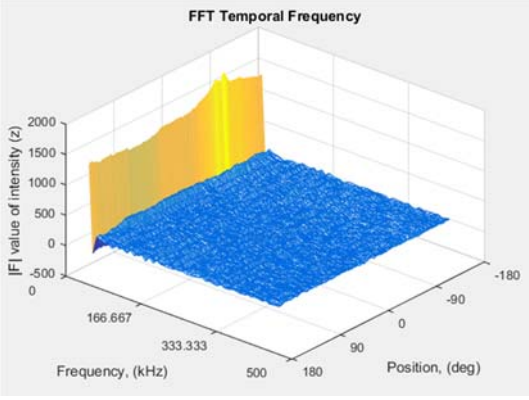

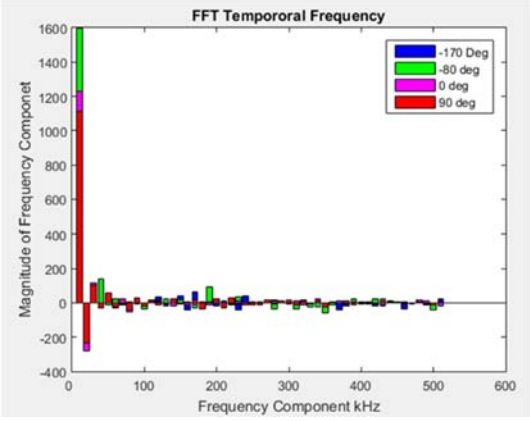

Unrolled Plot 6

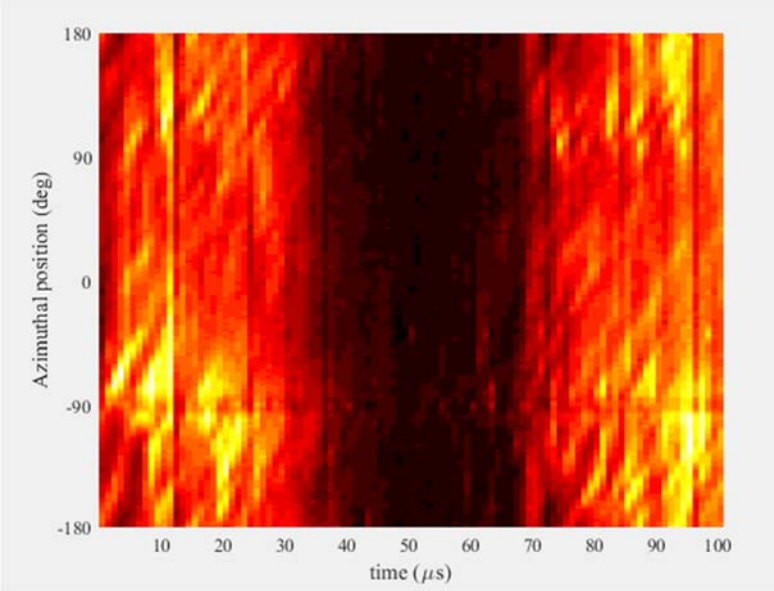

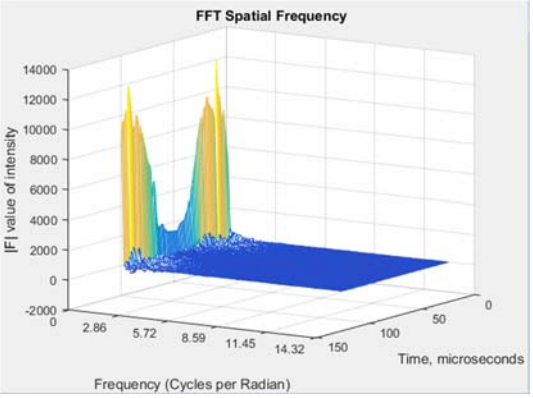

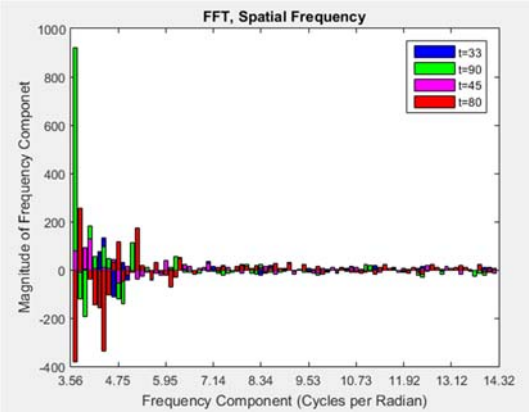

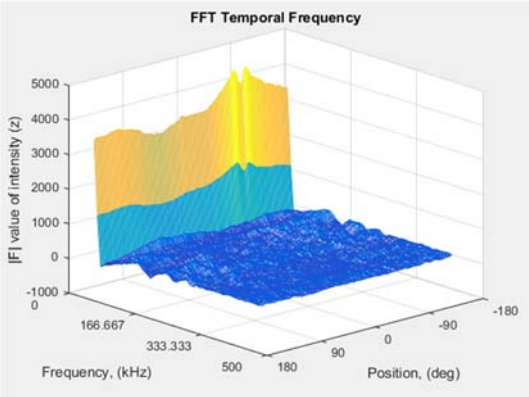

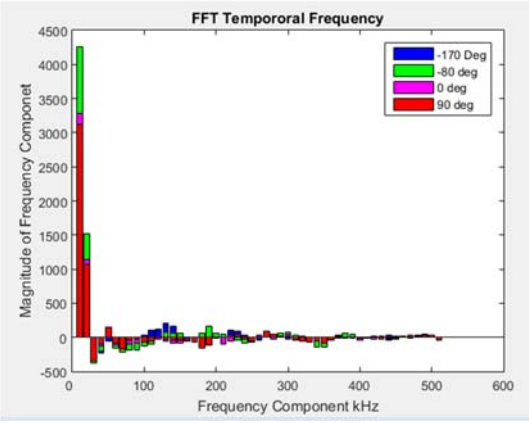

Unrolled Plot 7

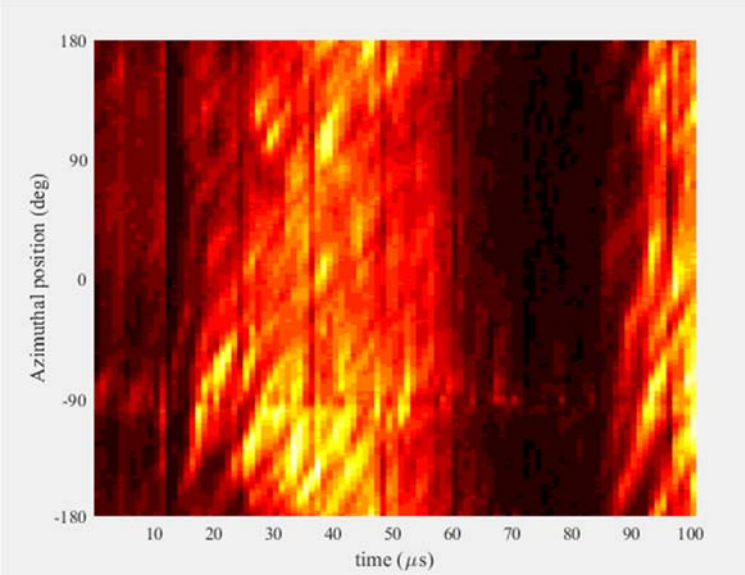

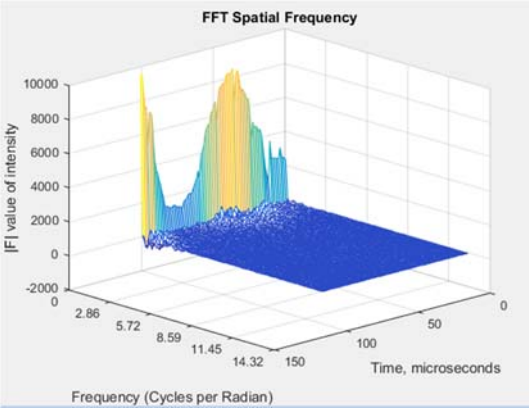

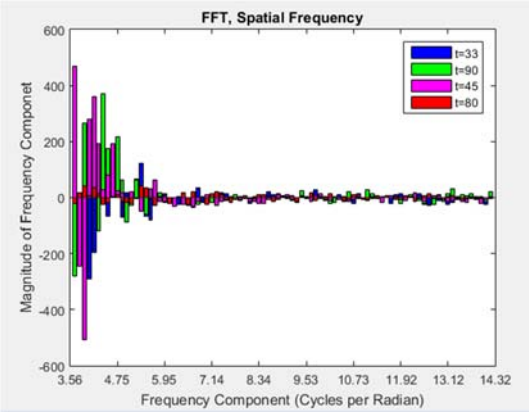

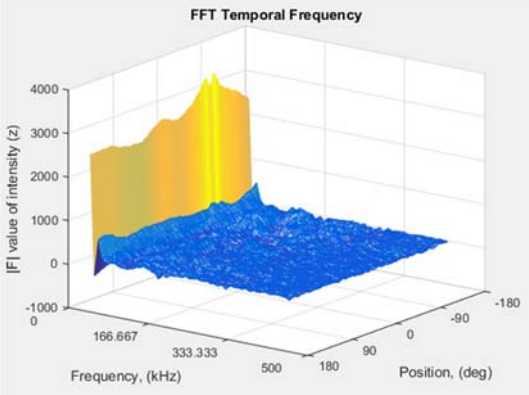

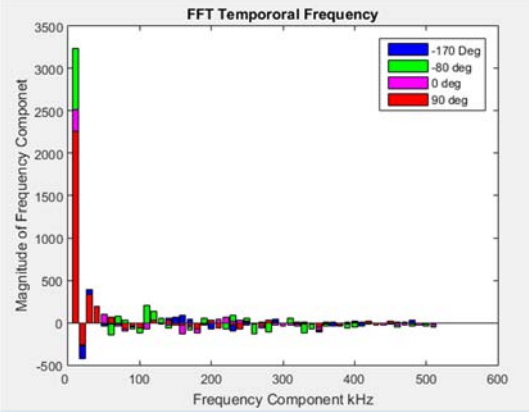

Unrolled Plot 8

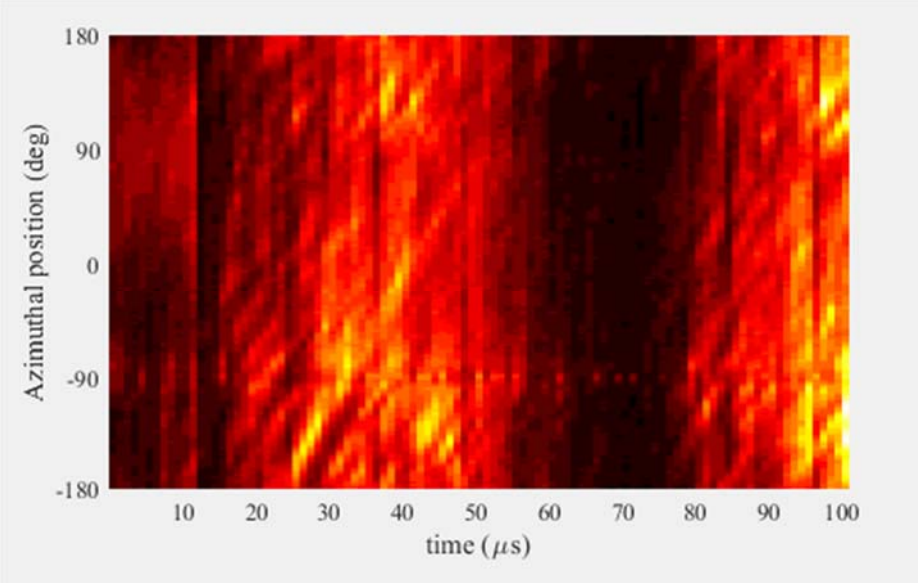

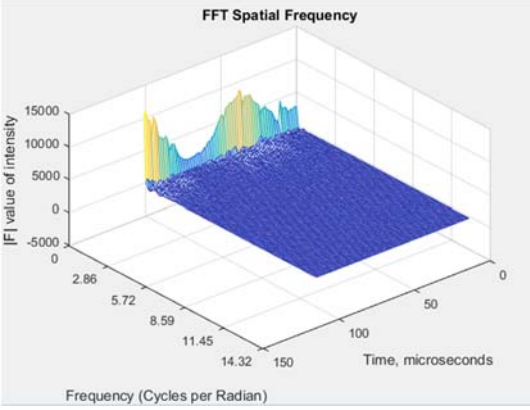

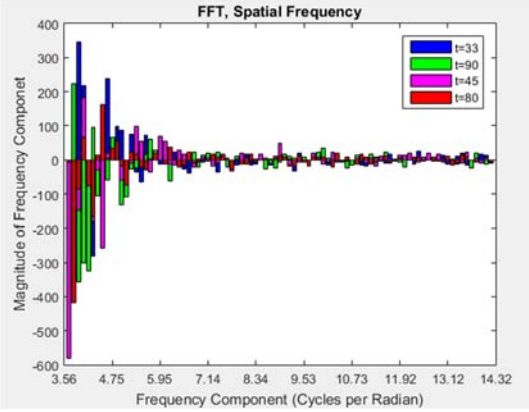

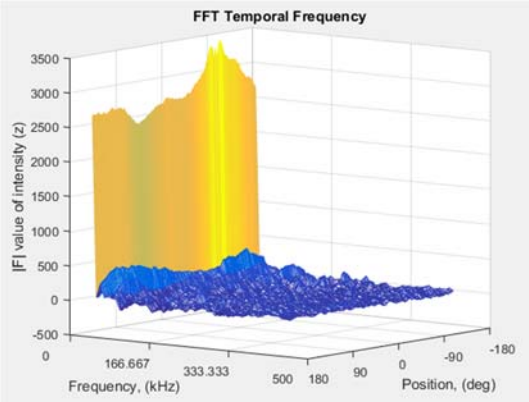

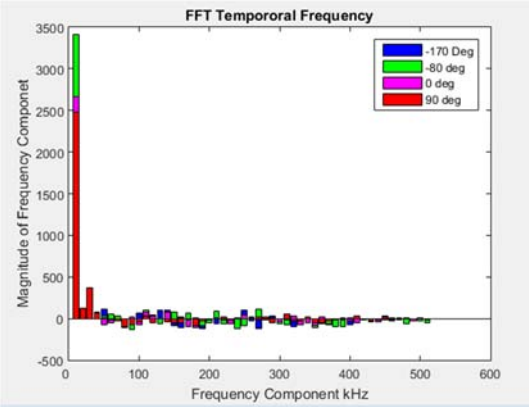

Unrolled Plot 9

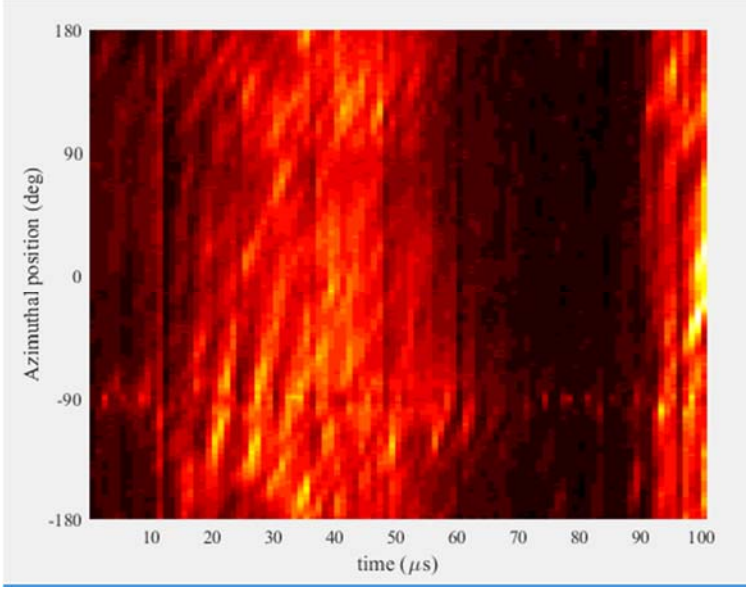

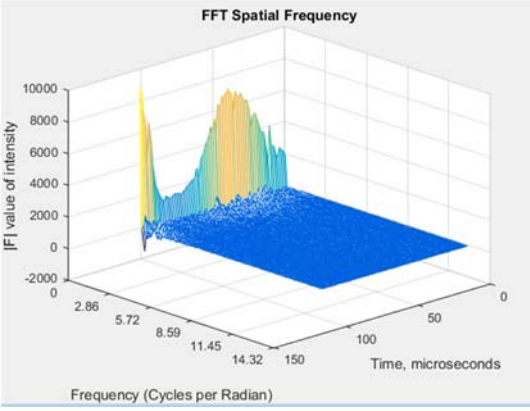

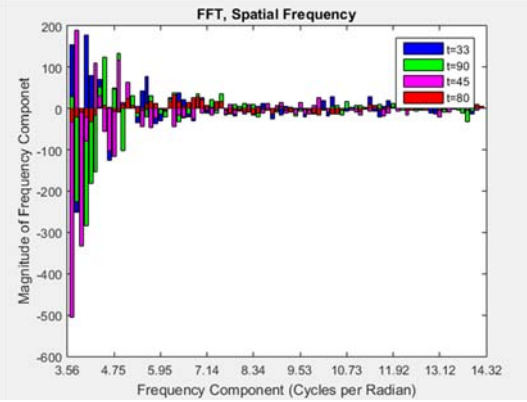

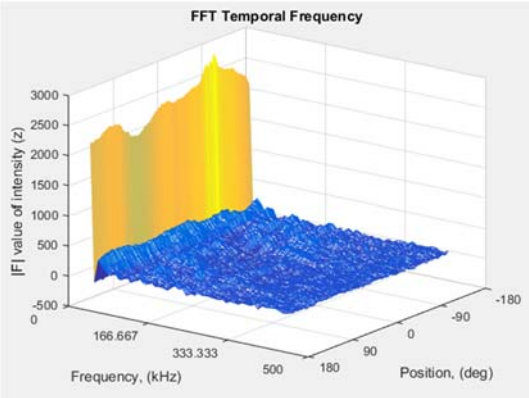

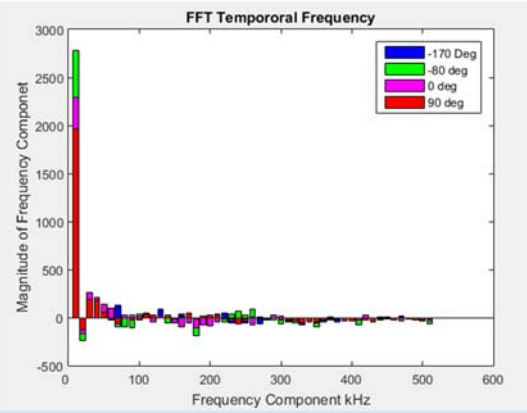

Unrolled Plot a

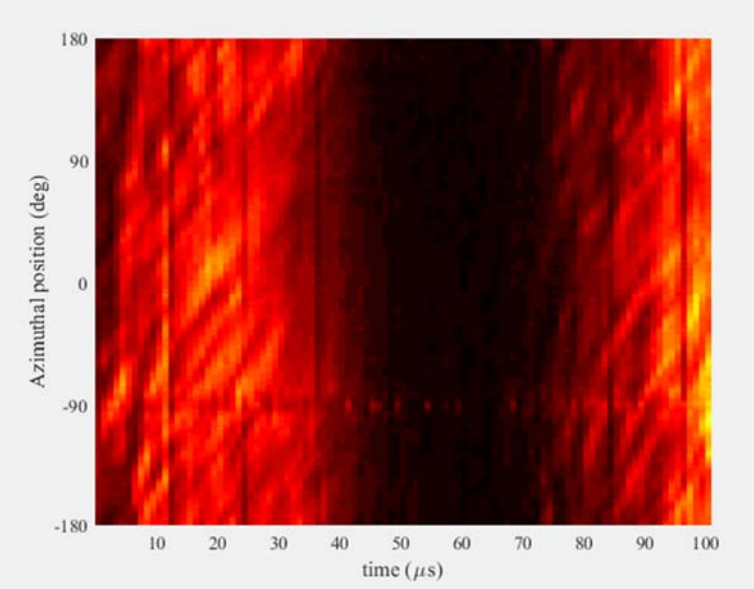

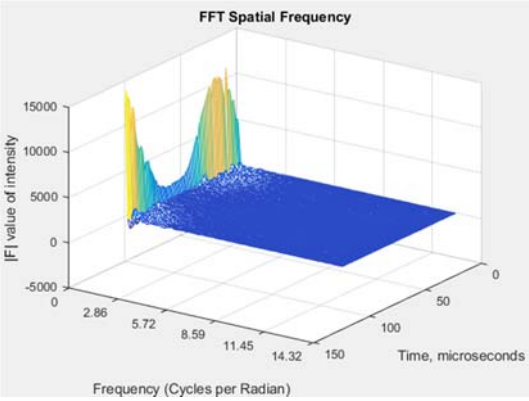

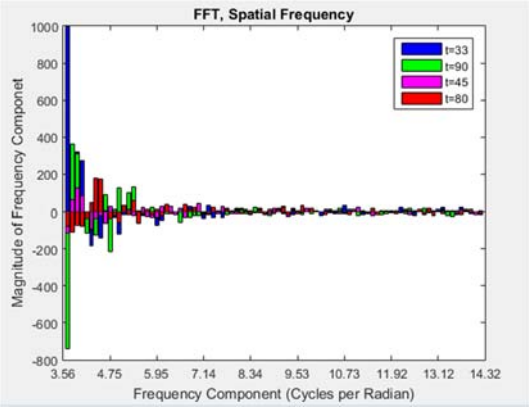

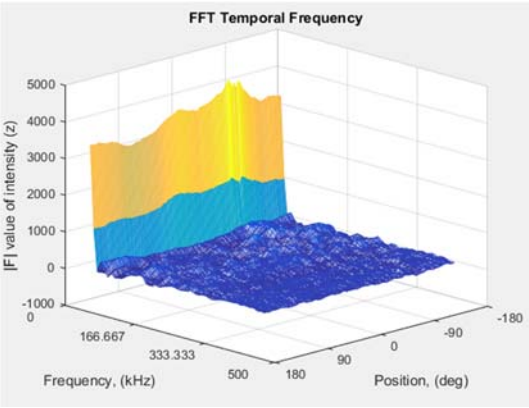

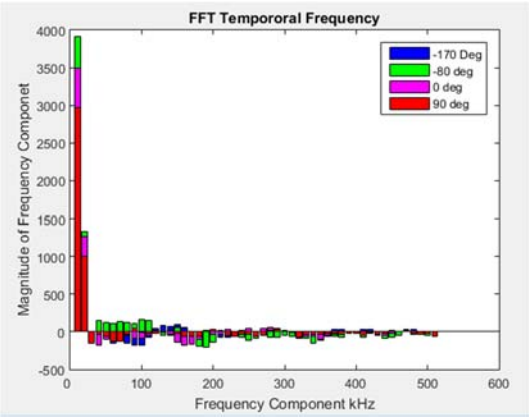

Unrolled Plot b

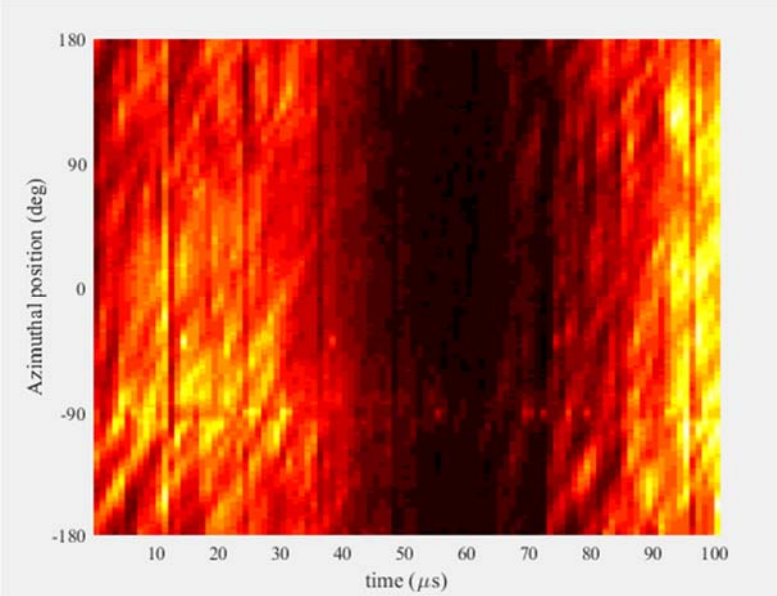

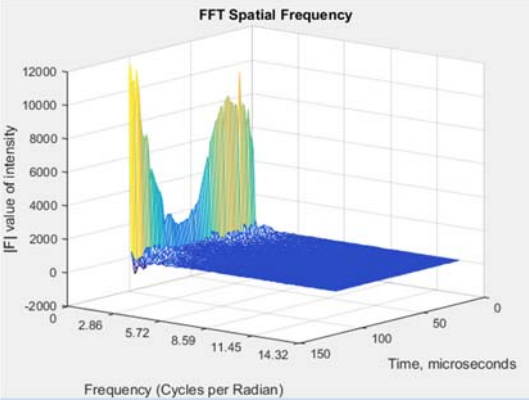

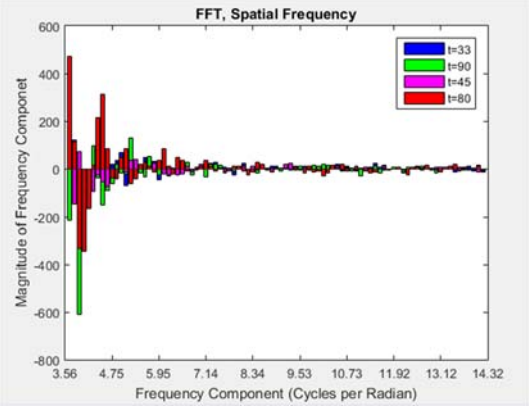

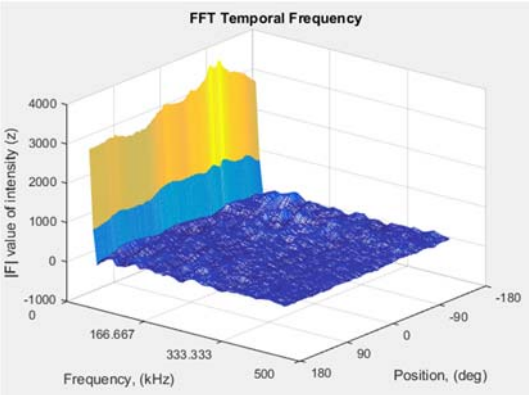

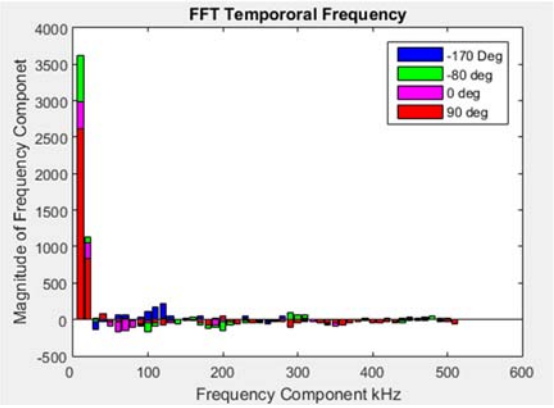

Unrolled Plot c

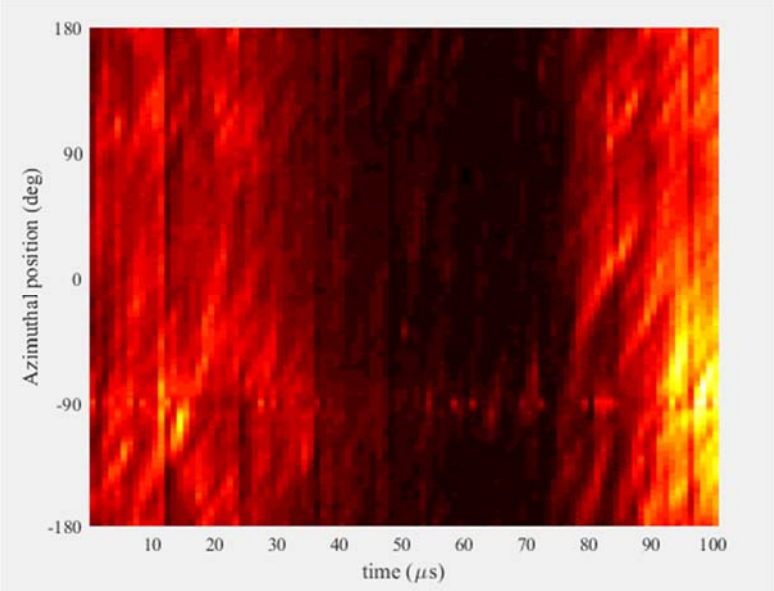

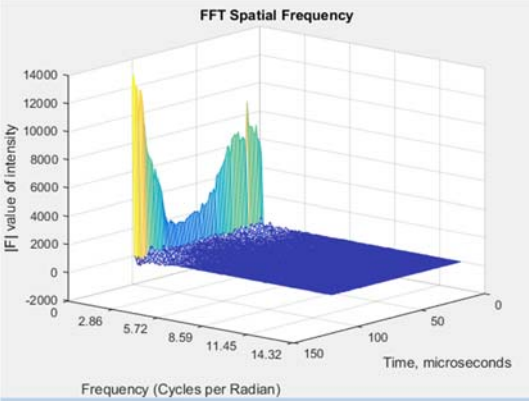

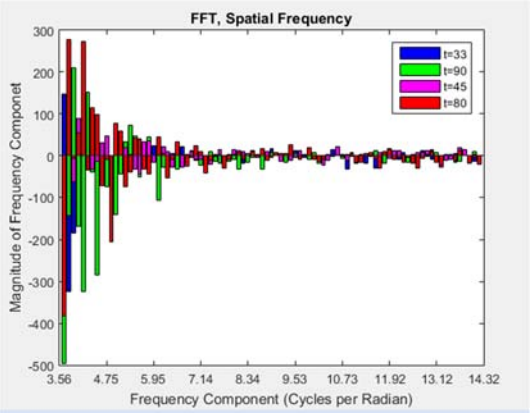

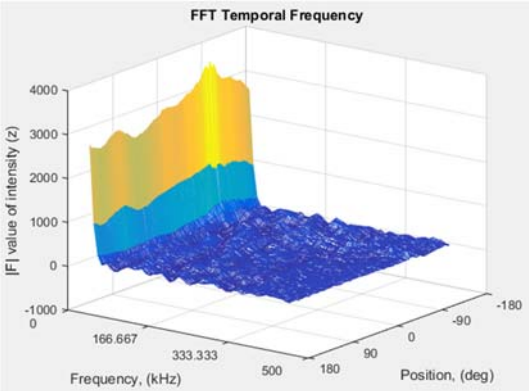

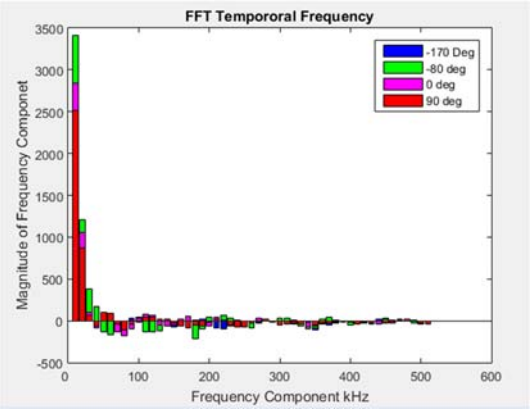

Unrolled Plot d

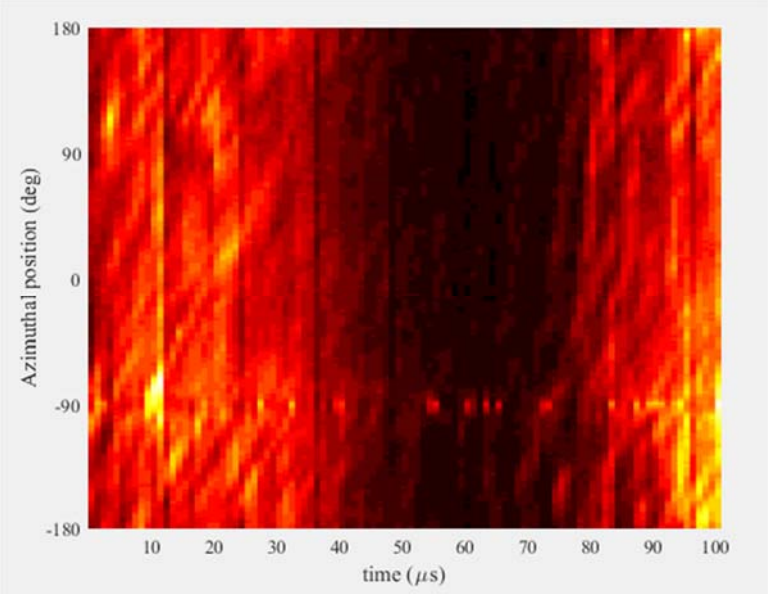

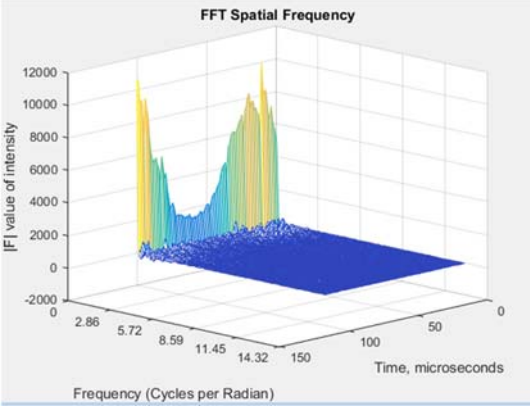

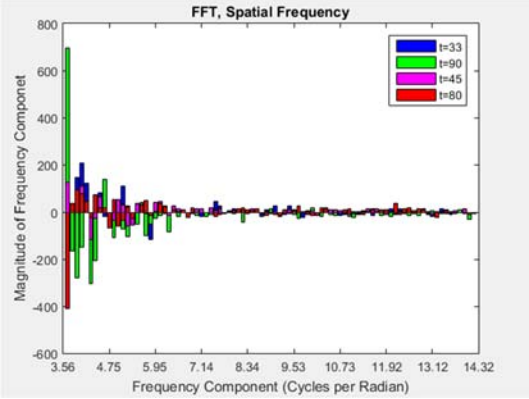

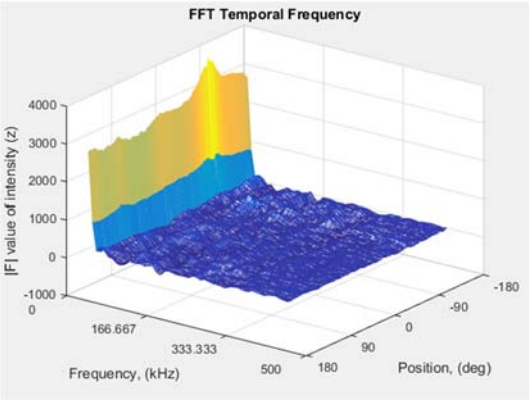

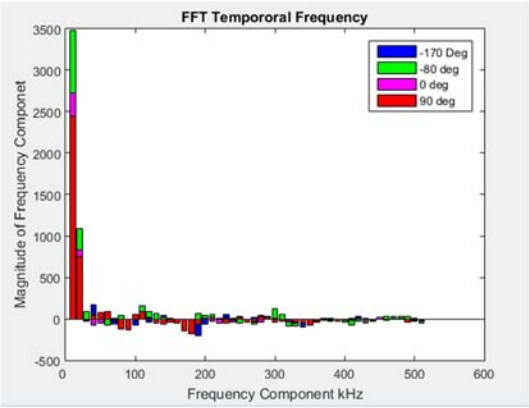

Unrolled Plot e

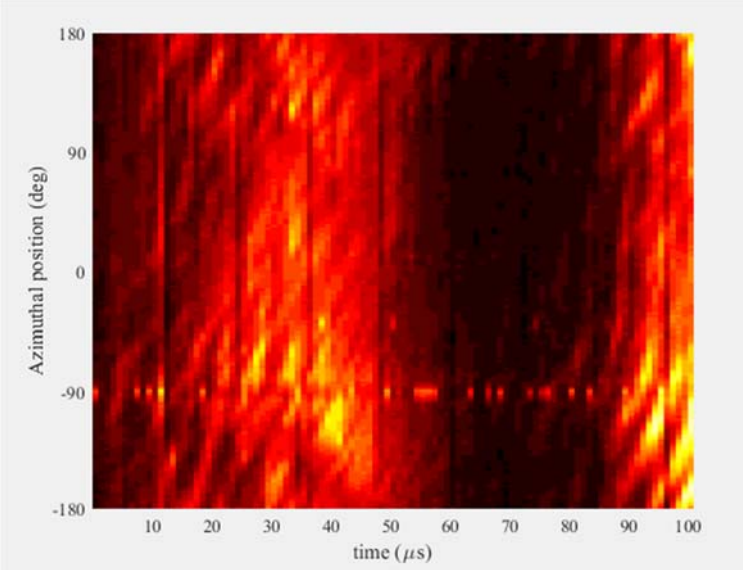

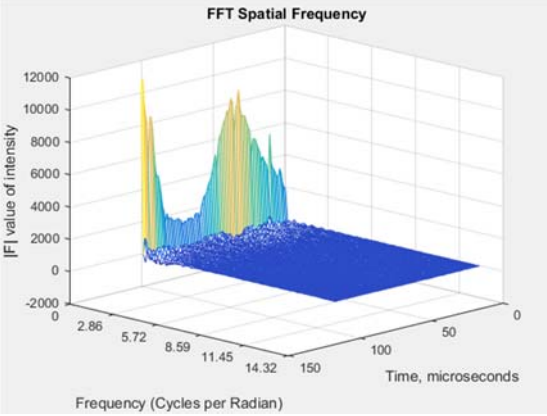

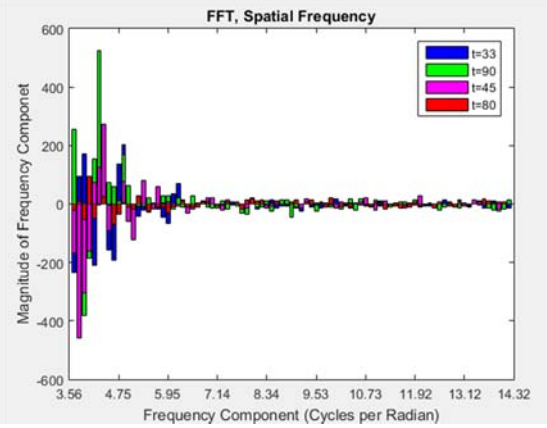

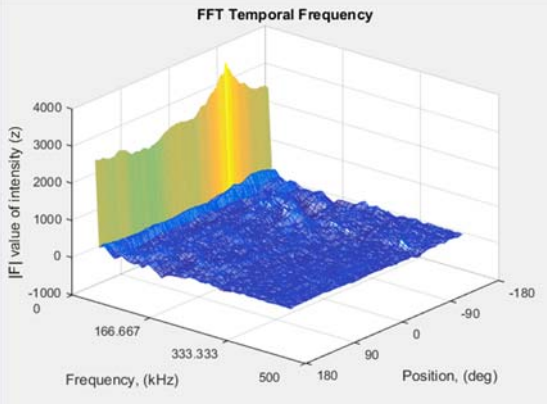

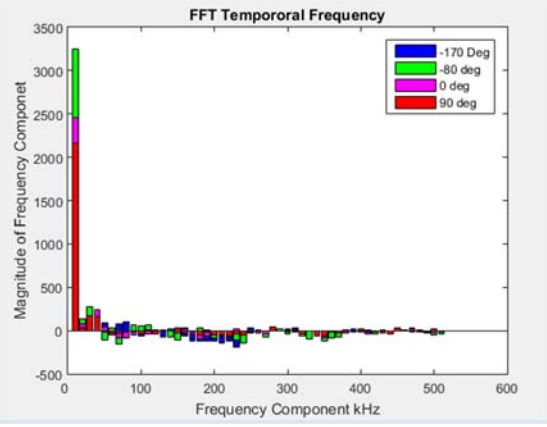

Unrolled Plot f

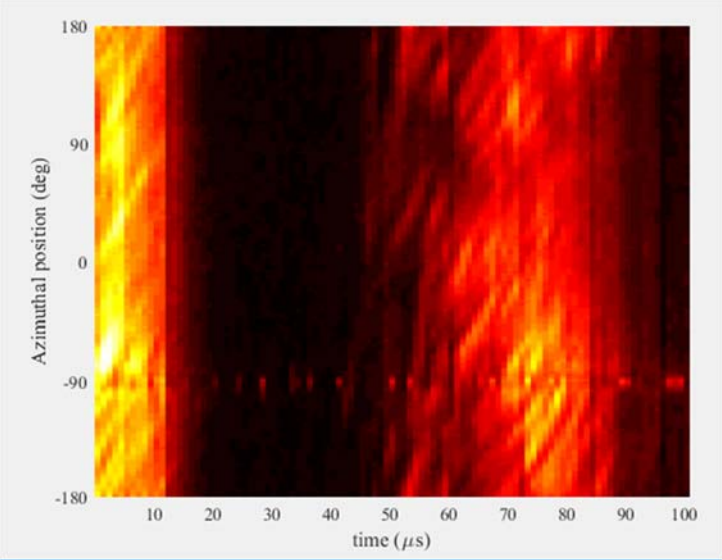

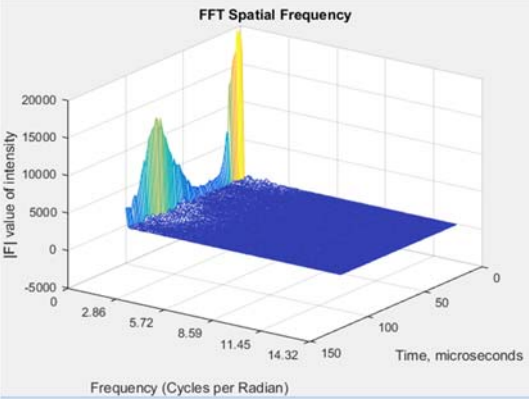

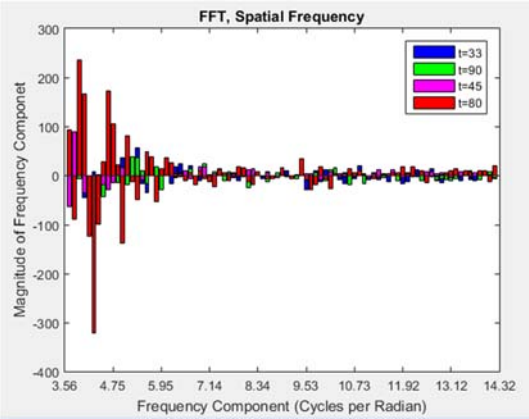

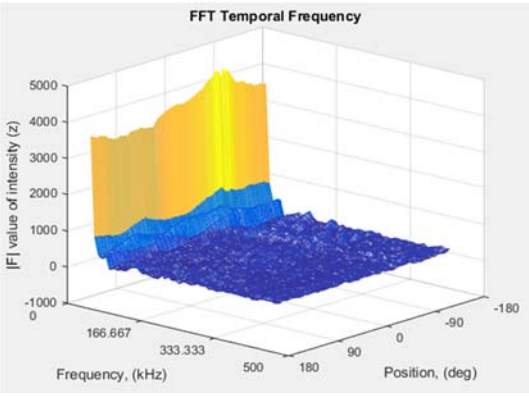

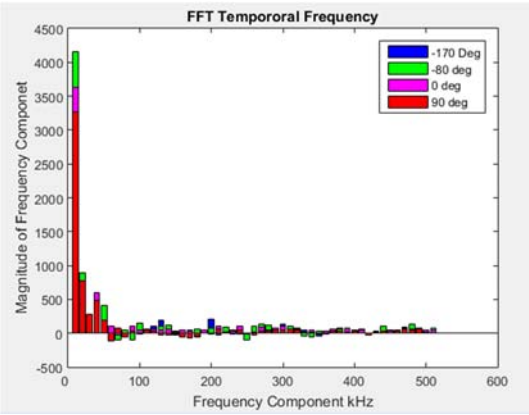

Bibliography

[1] D. M. Goebel and I. Katz, Fundamentals of Electric Propulsion: Ion and Hall Thrusters, Hoboken, New Jersey: JPL Space Science and Technology Series, Wiley, 2008.

[2] D. Williams, "http://www.busek.com," Busek, March 2012. [Online]. Available: http://www.busek.com/news__201203__aehf.htm. [Accessed 3 August 2016].

[3] A. E. Gonzales, M. K. Scharfe, J. W. Koo and W. A. Hargus, "Comparison of Numerical and Experimental Time-Resolved Near-Field Hall Thruster Plasma Properties," in *AIAA Joint Propulsion Conference*, Atlanta,Georgia, July- Aug 2012.

[4] M. S. McDonald, A. D. Gallimore, B. A. St. Pierre and C. K. Bellant, , "Measurement of Cross-Field Electron Current in a Hall Thruster Due to Rotating Spoke Instabilities," in *47th AIAA/ASME/SAE/ASEE Joint Propulsion Conference & Exhibit*, San Diego, California, 31 July - 03 August 2011.

[5] D. A. Cunningham, "Localized Plasma Measurement During Instability Modes In a Hall Thruster," Air Force Institute of Technology , Wright-Patterson Air Force Base, Ohio, 2016.

[6] W. Wiesel, spaceflight Dynamics, 2010.

[7] G. P. Sutton and O. Biblarz, Rocket Propulsion Elements Eighth Edition, Hoboken, New Jersey : John Wiley & Sons, Inc. , 2010.

[8] "Half life of the elements," Wolfram Research, Inc., [Online]. Available: http://www.periodictable.com/Properties/A/HalfLife.html. [Accessed 8 febuary 2007].

[9] D. A. Gurnett and A. Bhattacharjee, Introduction to Plasma Physics With Space and Laboratory Applications, Cambridge: The Press Syndicate of the University of Cambridge, 2005.

[10] H. Evans, J. Lange and J. Schmitz , The phenomenology of Intelligence-focused Remote Sensing, New York, NY: Riverside Research , 2014.

[11] J. Sansonetti and W. C. martin, "Handbook of Basic Atomic Spectroscopic Data," Quantum Measurement Division, PML, [Online]. Available: https://www.nist.gov/pml/handbook-basic-atomic-spectroscopic-data. [Accessed 15 January 2017].

[12] J. D. Hubba, Naval Research Laboratory Plasma Formulary, Washington DC: Naval Research Laboratory , 2013.

[13] D. Bohm, The characteristics of electrical discharges in magnetic fields, A. Guthrie and r. k. Wakerling, Eds., Ann Arbor, Michigan: McGraw-Hill Book Company, 1949.

[14] G. S. Janes and R. S. Lowder, "Anomalous Electron Diffusion and Ion Acceleration in a low-density plasma," *American Institute of Physics ,* vol. 9, no. 6, pp. 1115-1123, 1966.

[15] D. LTilley, K. H. De Grys and R. M. Meyers, "Hall thruster-cathode coupling," in *35th Joint Propulsion Conference and Exhibit*, Los Angeles Ca, 1999.

[16] J. D. Sommerville and L. B. King, "Effect of Cathode Position on Hall-Effect Thruster Performance and Near-Field Plume Properties," in *43th AIAA/ASME/SAE/ASEE Joint Propulsion Conference and Exhibit*, Cincinnati Oh, 2007.

[17] R. F. Kemp and J. M. Sellen, "Plasma Potential Measurements by Electron Emissive Probes," *Review of Scientific Instruments ,* vol. 37, p. 455, 1966.

[18] s. Mazouffre, A. Petin, P. Kudrna and M. Tichy, "Development of a High-Frequency Emissive Probe," *IEEE TRANSACTIONS ON PLASMA SCIENCE,* vol. 43, no. 1, 2015.

[19] D. J. Griffiths, Introduction to Electrodynamics 3rd edition, Upper Saddle River, New Jersey : Prentice Hall Inc , 1999.

[20] B. Rubin, a. kapulkin and m. Guelman, "Research on Optimization of Onboard Magnetic Diagnostics System of Hall Thruster Plasma," in *International electric Propulsion Conference,*, New Jersey, 2005.

[21] D. Liu, R. E. Huffman, R. D. Branam and W. A. Hargus Jr, "Ultra-High Speed Imaging of Hall Thruster Discharge," 2011.

[22] D. Liu, *Two-Dimensional Time-Dependent Plasma Structures of a Hall Effect Thruster,* Dayton : Air Force Institue of technology , 2011.

[23] Busek Co. Inc., "BHT-600-pm Permanent Magnet Hall Thruster Installation and Operating Manual," Natick, 2016.

[24] B. C. Inc., "www.busek.com," 2013. [Online]. Available: http://www.busek.com/index_htm_files/70008509B.pdf.

[25] N. Hyatt, C. R. Hartsfield and D. Cunningham , "Hall Effect Thruser Characterization Through Potential, Magnetic, and Optical Measurments," in *AIAA SciTech* , Grapevine Texas , 2017.

[26] high-Speed Video Camera Instruction Manual.

[27] A. J. Wheeler and A. R. Ganji, Introduction to Engineering Experimentation, Englewood Cliffs, New jersey: Prentice-Hall, Inc, 1996.

[28] R. F. Mills, *EENG 571: Chapter 3, Base band signals,* Dayton Oh, 2017.

[29] P. Major David Liu, Interviewee, *Chamber issue discussions.* [Interview]. 12 Feburary 2017.

REPORT DOCUMENTATION PAGE

Form Approved
OMB No. 074-0188

1. REPORT DATE *(DD-MM-YYYY)*	2. REPORT TYPE	3. DATES COVERED *(From – To)*
22-03-2012	Master's Thesis	August 2015 – March 2017

TITLE AND SUBTITLE

HALL EFFECT THRUSTER CHARACTERIZATION THROUGH POTENTIAL, MAGNETIC, AND OPTICAL MEASUREMENTS

5a. CONTRACT NUMBER

5b. GRANT NUMBER

5c. PROGRAM ELEMENT NUMBER

6. AUTHOR(S)

Hyatt, Nicholas, L., Captain, USAF

5d. PROJECT NUMBER

5e. TASK NUMBER

5f. WORK UNIT NUMBER

7. PERFORMING ORGANIZATION NAMES(S) AND ADDRESS(S)
Air Force Institute of Technology
Graduate School of Engineering and Management (AFIT/ENY)
2950 Hobson Way, Building 640
Wright-Patterson AFB OH 45433-7765

8. PERFORMING ORGANIZATION REPORT NUMBER

AFIT-ENY-MS-17-M-267

9. SPONSORING/MONITORING AGENCY NAME(S) AND ADDRESS(ES)
Air Force Office of Scientific Research Energy
Attn: Dr. Mitat Birkan
875 N. Randolph, Ste 325
Arlington, VA 22203
mitat.birkan@us.af.mil

10. SPONSOR/MONITOR'S ACRONYM(S)
AFOSR

11. SPONSOR/MONITOR'S REPORT NUMBER(S)

12. DISTRIBUTION/AVAILABILITY STATEMENT
DISTRUBTION STATEMENT A. APPROVED FOR PUBLIC RELEASE; DISTRIBUTION UNLIMITED.

13. SUPPLEMENTARY NOTES
This material is declared a work of the U.S. Government and is not subject to copyright protection in the United States.

14. ABSTRACT
Electric propulsion is a lucrative method for providing ΔV to spacecraft. In general, much higher I_{sp}s are obtained compared to their chemical counterpart. A Hall Effect Thrusters is a subset of electric propulsion with moderately high specific impulse and thrust when compared to other forms of electric propulsion. Even though Hall thrusters have been in use for over 50 years there are still many unknowns associated with their operation. Experimental research will be conducted in AFIT's Space Propulsion Application Simulation System laboratory, to measure Hall current, plasma potential and visible emission from the 600W Hall thruster in a time correlated system at high data rates. Additionally data will be analyzed to correlate behavior of plasma instabilities to determine causal relationships between plasma properties and anomalous diffusion modes.

15. SUBJECT TERMS
Hall Thruster, Hall Effect Thruster, Electric Propulsion, Ion, Frequency Analysis , Plasma,

16. SECURITY CLASSIFICATION OF:			17. LIMITATION OF ABSTRACT	18. NUMBER OF PAGES	19a. NAME OF RESPONSIBLE PERSON
a. REPORT	b. ABSTRACT	c. THIS PAGE			Dr. Carl Hartsfield, AFIT/ENY
U	U	U	UU	153	19b. TELEPHONE NUMBER *(Include area code)* (937) 255-3636, ext 4667 Carl.hartsfield@afit.edu

Standard Form 298 (Rev. 8-98)
Prescribed by ANSI Std. Z39-18